FINESTRUCTURE AND TURBULENCE IN THE DEEP OCEAN

by

PETER JOHN HENDRICKS

A.B. and Sc.B., Brown University
(1967)

M.S., University of California, San Diego
(1969)

SUBMITTED IN PARTIAL FULFILLMENT OF THE
REQUIFEMENTS FOR THE DEGREE OF
DOCTOR OF PHILOSOPHY

at the

MASSACHUSETTS INSTITUTE OF TECHNOLOGY

and the

WOODS HOLE OCEANOGRAPHIC INSTITUTION

January 1977

Signature of Author: _____
Joint Program on Oceanographic Engineering,
Massachusetts Institute of Technology-Woods Hole
Oceanographic Institution, January 1977

Certified by: _____
Thesis Supervisor

Accepted by: _____
Chairman, Joint Committee on Oceanographic
Engineering, Massachusetts Institute of Technology-
Woods Hole Oceanographic Institution.

FINESTRUCTURE AND TURBULENCE IN THE DEEP OCEAN

by

Peter John Hendricks

Submitted to the Department of Ocean Engineering in partial fulfillment of the requirements for the degree of Doctor of Philosophy.

ABSTRACT

Millimeter scale fluctuations in refractive index recorded with a freely sinking shadowgraph system are correlated with finestructure profiles of temperature, salinity and density and compared to models of ocean turbulence. Images with vertically aligned periodic structure, called bands, are identified as salt fingers, while others with chaotic structure are turbulent.

Images are found on interfaces that are 1-10 m thick and have gradients at least several times the mean. From 6 profiles in the Mediterranean Outflow region of the eastern North Atlantic between 1.0 and 1.9 km depth, 398 interfaces have been identified and a significant fraction (about 1/3) of these have detectable images. High contrast images, including bands, are most often found below warm, saline intrusions and within stepped structure where there is a regular sequence of homogeneous mixed layers separated by interfaces. As the interfacial salinity gradient increases in the sense that allows salt finger convection, the fraction of interfaces with images increases. The horizontal spacing of bands ($\sim$ 5 mm) is consistent with calculated salt finger diameter. The calculated and observed length of ocean salt fingers (10-20 cm) is a small fraction of the interface thickness.

High levels of small scale variability in the shadowgraphs is reflected in high levels of variance in the finestructure band of the temperature spectra. The temperature gradient spectra have a slope of -1, indicative of turbulence affected by buoyancy forces, and there is a relative peak at a wavelength near the observed salt finger length.

The high contrast images are found at interfaces within the enhanced mean salinity gradient below saline intrusions. For very strong salinity gradients there is a solitary interface with intense images, but for weaker mean gradients the convection takes the form of stepped structure. The steps may evolve from the solitary interface as the salinity gradient is run down by salt finger convection.

This study identifies parts of the ocean where salt finger convection is prevalent and includes the first comprehensive description of salt fingers in the ocean. Existing models of salt fingers are evaluated in light of ocean observations, and models of ocean turbulence are compared to measurements.

Thesis Supervisor: Albert J. Williams 3rd
Title: Associate Scientist

ACKNOWLEDGEMENTS

Dr. A. J. Williams, 3rd, my adviser, devised and carried out the ocean experiments that form the basis for this thesis. He encouraged me to analyze these data, provided the necessary resources, and gave me valuable guidance. Karen Pires typed several drafts and part of the final copy, which was completed by Ruth Brown. John Tochko helped with figures. My wife, Kathleen, did most of the drafting, some of the typing and gave me the encouragement that I needed to finish my thesis. The Woods Hole Oceanographic Institution patiently supported my work. Support from ONR contract N00014-66-C0241 NR 083-004 is also acknowledged.

TABLE OF CONTENTS

LIST OF FIGURES

1. INTRODUCTION

Transport of heat, mass and momentum in the ocean, maintenance of the ocean thermocline, and dispersal of contaminants in natural bodies of water are closely related problems. They are all critically dependent on mixing mechanisms and their effectiveness. Transport rates that are implied from large scale conservation equations, the depth of the ocean thermocline, and dispersal rates calculated from dye studies all show that the rates are much greater than can be explained by molecular diffusion. Since accelerated transport is one of the fundamental properties of turbulent flow, this suggests that the ocean may be turbulent in some sense. But rather than being continually in a weakly turbulent state, recent measurements suggest there may be infrequent but energetic events sparcely distributed throughout the ocean which affect the mixing. Since most of the ocean is not turbulent at any instant and mixing events may be rare, it is difficult to make direct measurements of these transitory events. In fact it has been suggested that the dominant portion of mixing in the ocean takes place at the boundaries and that processes in the interior, other than advection, have a negligible effect.

In this study, certain specific mixing events are identified in the ocean. These events are then analyzed in detail to describe their dimensions and physical characteristics. On the basis of these measurements some estimates of the effectiveness of these events as turbulent mixing are made. Further, an attempt is made to determine what the conditions are that are favorable to these events.

1.1 Finestructure in the Ocean

Finestructure of temperature, salinity, density and velocity in the ocean has been puzzling ever since instruments capable of measuring it have been used. Generally it is too large to be a direct result of molecular transport phenomona and too small to be of interest in the large scale balances of the general circulation. On the other hand, it may provide clues as to how scales larger and smaller than itself communicate and place practical limits or bounds on processes operating in the ocean. For example, creating a layer that is homogeneous in density from a region that previously had a linear stratification requires an input of energy and maintaining such a layer requires continuous stirring. Similarly, a density inversion has potential energy that is lost when it sinks to its equilibrium level.

Finestructure may be characteristic of some physical process that is also operating on a scale that is larger than or smaller than the finestructure. A particular example which will be discussed at length here is stepped structure, where relatively homogeneous layers in temperature, salinity and density are bounded by interfaces where these properties change abruptly with depth. These steps may be regular when there is an orderly sequence of them of nearly the same dimensions or irregular when they are intermittant and of varying size. An important question in either case is what is the physical interpretation of these layers? Are they a transitory effect due to distortion of a more uniform situation by a field of internal waves, or do they represent convective overturning and mixing?

Since all measurements that have sufficient resolution show finestructure in the ocean, there should be an explanation for finestructure with general applicability. Such an explanation is almost certainly closely related to internal gravity waves. One of the fundamental properties of a stratified fluid is the ability to support internal gravity waves and in environmental fluids (such as the ocean and the atmosphere), they are always present. They are often energetic and they are capable of distorting slowly varying fields in the ocean into more contorted ones with smaller scale variations. In fact, the band of wave numbers and frequencies that are described by internal gravity wave theory generally coincides with the finestructure band. In many cases finestructure and internal waves have a very intimate relationship. A model has been proposed (Garrett and Munk, 1972; Garrett and Munk, 1975) which relates the statistics of finestructure measurements to the dynamics of inertio-internal gravity waves, that is, waves in which effects of the earth's rotation are also included. This model is semi-empirical in that it was constructed and has been refined to agree with finestructure measurements. Even so its universality has been surprising and there have been few measurements which do not fit the model.

The Garrett-Munk model is a universal spectrum of finestructure fluctuations when scaled in appropriate non-dimensional variables. It assumes that the finestructure observed is due to distortion of more smoothly varying fields by a large number of superposed internal gravity waves, and the resulting statistical description is homogeneous and isotropic. Since most measurements agree with the proposed model

to within an order of magnitude under a wide variety of conditions, the model appears to have great general applicability. But there are regions in the ocean where the finestructure is not a direct result of internal waves. Two possible situations are interleaving of water layers with different origins and different temperature salinity characteristics and layer interface structures that are caused by double diffusive convection. A critical question then arises: is the spectrum of finestructure in these two situations distinguishable from the model spectrum of internal waves? If so, then the spectrum of finestructure may be used as an indicator of mixing in the ocean. While if not, then the model should not be interpreted as a distinctive description of internal waves. Hayes et al. (1975) have shown that temperature spectra have levels greater than the model spectrum when there is interleaving of dissimilar water layers, and here temperature finestructure attributable to double diffusive convection will be compared to the model spectrum. The most fundamental characteristic of a stratified fluid is the Brunt-Väisälä frequency, N, which has two related interpretations. It is defined by

$$N = \left\{ -\frac{g}{\rho} \left[\frac{d\rho}{dz} - \frac{\partial \rho}{\partial z} \right)_{\eta, S} \right] \right\}^{1/2} \qquad (1.1)$$

where ρ is the density, the vertical coordinate, z, is positive upward, g is the gravitational acceleration, and the partial derivative is taken with entropy, η, and salinity, S, held constant, i.e., adiabatically. In order to displace a fluid particle vertically, a distance ζ from its equilibrium position adiabatically requires an amount of work per unit mass equal to

$$\Delta e = N^2 \zeta . \qquad (1.2)$$

While, once it is released from this new position, it will oscillate about its equilibrium position with frequency N if the effects of viscosity and heat conduction are neglected. This illustrates that N can be seen as a measure of potential energy or as the frequency of internal gravity waves.

Although internal waves are energetic, pervasive, and may lead to significant amounts of mixing by breaking, this study concentrates on finestructure that is attributable to intermixing of water masses with different origins and to double diffusive convection. Both of these effects depend on the equation of state for sea water whereby the density, ρ, at constant pressure is a function of both temperature, T, and salinity, S, or

$$\rho = \rho_0 \left[1 - \alpha (T - T_0) + \beta (S - S_0) \right] \qquad (1.3)$$

where the subscript zero defines a reference state and

$$\alpha = - \frac{1}{\rho} \left(\frac{\partial \rho}{\partial T} \right)_{S,p} , \quad \beta = \frac{1}{\rho} \left(\frac{\partial \rho}{\partial S} \right)_{T,p} \qquad (1.4)$$

are the coefficients of expansion for heat and salt. Since $\alpha, \beta > 0$, the density of sea water can be increased either by decreasing the temperature or increasing the salinity. Thus two layers of sea water may be at the same density when one is both warmer and saltier than the

other. A particularly useful way of expressing this relationship is the T-S diagram. The graph in Figure 1.1 has salinity as its abscissa and temperature as the ordinate. Lines of constant density slope downward from right to left, but they have some curvature due to non-linearities in the equation of state. The direction of increasing density is toward the lower right as shown in the diagram. Each water type, i.e., a specific temperature and salinity is represented as a single point, and two are depicted in the diagram A and B. The water type A is warmer, saltier and lighter than B, and if they were in the same vertical column, A would float on B.

A straight line connecting the two water types A and B defines a water mass which represents all linear combinations of the two water types at the end points. In some instances there may be a third water type present; for example C is saltier than A or B but between them in temperature and density. The lines AC and BC then define water masses, while any point within the triangle ABC is attainable with a combination of A, B and C. The above discussion has assumed that temperature (more properly, enthalpy) and salinity are conserved when two parcels of water mix and while that is not strictly true it is usually an adequate representation. In summary, a straight line on a T-S diagram is evidence of linear binary mixing, while deviations from a straight line may be explained by the presence of a third water type involved in the mixing.

Suppose there is a water column that is described by the line AB on a T-S plot; that is, a CTD (Conductivity, Temperature and Depth, see Appendix A), cast when plotted in this form is a straight line AB. A schematic example where temperature, salinity, and

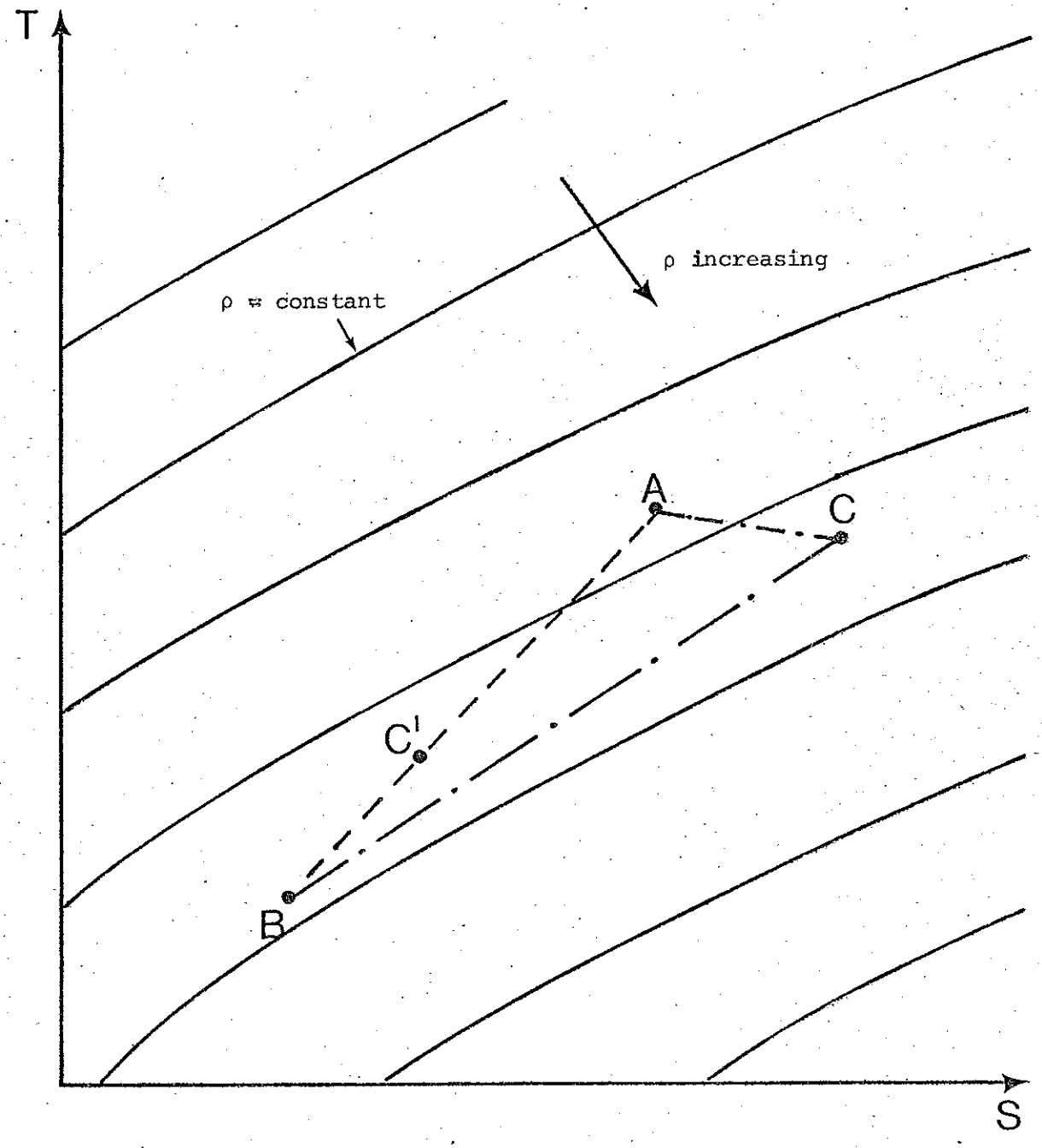

FIGURE 1.1 Schematic T-S plot. Each point is a particular water type and a straight line connecting two points represents all combinations of the two water types at the end points. Lines of constant density are also shown with an increase toward the lower right.

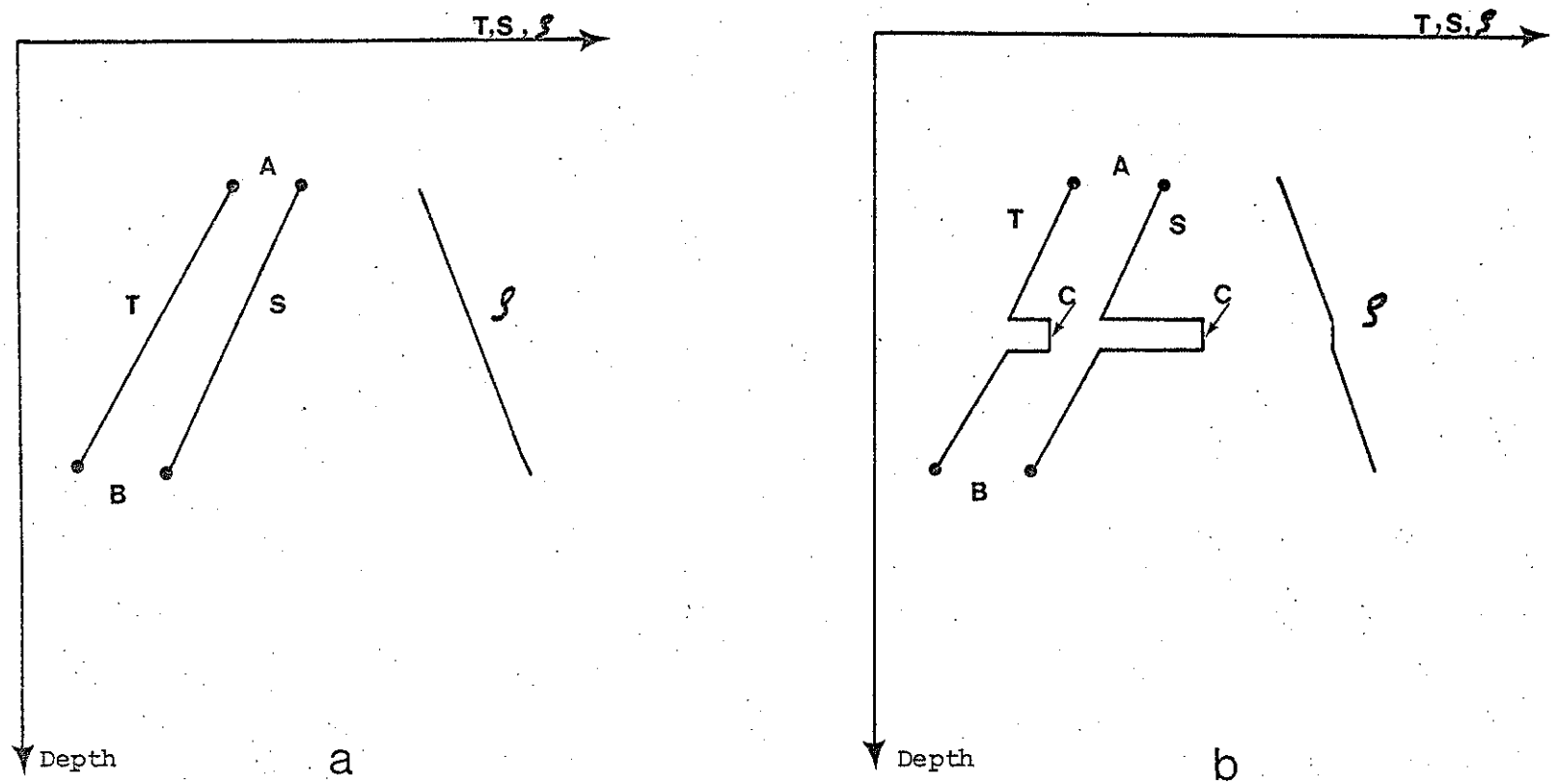

FIGURE 1.2 Schematic profiles of temperature, salinity, and density. a) Simple linear profiles where temperature and salinity decrease with depth while density increases. b) Effect of a warm salty intrusion on the profile in a). These profiles are also represented in the T-S plot 1.1.

density all vary linearly with depth is shown in Figure 1.2a. Although these distributions were drawn as straight lines for simplicity, they need not be to produce a straight line on a T-S plot. In Figure 1.2b an intrusive layer C is advected into the water column at a level where its density is stable with respect to the water above and below. This level is represented as the point C on the curve AB. The new distribution shown in Figure 1.2b has sharp gradients in both T and S above and below the intrusion, while the density gradients are weakened. One of the prime motives of this thesis is to describe what may happen to an intrusive layer such as C, how it interacts with the layers above and below, and what processes are important in this interaction.

1.2 Turbulence and Dissipation

When finestructure exists as a result of distortion by internal gravity waves or by advection of dissimilar water types, there need not be turbulence. Turbulence is understood to mean three-dimensional random flow which results in dissipation of kinetic energy and accelerated transport. Internal waves are not turbulent because they are not necessarily dissipative and advection can also take place entirely within the laminar regime. Turbulence is also characterized by variations on a continuous range of length scales from the largest which is the scale of the kinetic energy input to the smallest where the variations are eliminated by diffusion and viscosity.

In the measurements to be described, fluctuations in the index of refraction, which is closely related to density, have been detected in the deep ocean using a shadowgraph technique. Since the length

scale of these fluctuations is in the millimeter range, they may be interpreted within the context of turbulent flow. By using the formalism of isotropic turbulence theory, some characteristics of the flow that includes these fluctuations can be inferred.

In the case of a homogeneous fluid, there are simple relationships among various properties of a turbulent flow which have been derived by Kolmogorov. The theory only applies when the length scale at which the turbulence is produced is much larger than that for dissipation. This is equivalent to large Reynolds Number flow. Then, by dimensional analysis, the length scale at which dissipation of kinetic energy takes place, η_v, is related to the dissipation rate per unit mass, ϵ, and the kinematic viscosity, ν, by

$$\eta_v = \left(\nu^3/\epsilon\right)^{1/4} \tag{1.5}$$

where the relation may be regarded as a definition of η_v. An important feature of this relation is that the length scale of dissipation becomes smaller as the dissipation rate increases. A time scale, t_v, is similarly defined,

$$t_v = \left(\nu/\epsilon\right)^{1/2} \tag{1.6}$$

which is the turnover time of the viscous eddies.

When the fluid is stratified the situation becomes more complicated. The stratification itself is a reservoir of potential energy which can supply or absorb some of the turbulent energy. Also the length scale at which viscosity acts to dissipate turbulent kinetic energy may not be the same as the scale where diffusion smooths out

fluctuations in the temperature and salinity fields. In sea water, the diffusivities for both heat and salt are smaller than the viscosity, which allows both to have fluctuations at smaller scales than the smallest velocity shears. If the dynamic effects of the temperature and salinity can be neglected at these small scales, then Batchelor's (1959) estimate of a diffusive length scale in the case of large Prandtl Number (or Schmidt Number in the case of salinity fluctuations) can be used, namely

$$\eta_d = \left(\frac{\nu k^2}{\epsilon}\right)^{1/4} \tag{1.7}$$

where k is the diffusivity for heat or salt. Since

$$\frac{\eta_\nu}{\eta_d} = \left(\frac{\nu}{k}\right)^{1/2} \tag{1.8}$$

this ratio can be estimated for sea water where $P_r = \frac{\nu}{k_T} \cong 7$ and $S_c = \frac{\nu}{k_s} \cong 10^3$. Hence the ratio of the dissipative scales is about 2.7 for temperature fluctuations and 30 for salinity fluctuations.

The essential question about these small scale turbulent features in the deep ocean is how are they generated. Since they are so small, their diffusive lifetimes are correspondingly short. For a salinity interface the age can be approximated by dimensional analysis as

$$t_d = \ell^2/k_s \tag{1.9}$$

where ℓ is the characteristic length. For the turbulent structures visible on the shadowgraphs ℓ is several millimeters and t_d is a few hours. This implies that the visible turbulence has been generated locally and quite recently.

Nearly all turbulence observed with the shadowgraph technique in the ocean occurs on interfaces where the gradients of temperature, salinity and density are greater than their mean values. This may be related to the availability of large differences in index of refraction, or it may truly represent the concentration of turbulence at interfaces. In any case, turbulence is invisible to the shadowgraph system where there are no anomalies in index of refraction. Because turbulence is necessarily dissipative, there must be an energy source if the turbulence is to be maintained; similarly, strong gradients found at the interfaces must somehow be maintained or be eroded by diffusion.

There are two classes of flows which seem to satisfy the implicit requirements of sharp gradients and small scale turbulence. The first may be termed shear instability where the turbulent kinetic energy comes from the kinetic energy of the mean current field. The transformation takes place by instability driven by shear. The second likely source of turbulence is double diffusive convection. Here the energy source is the potential energy in the stratification and the turbulent kinetic energy is maintained by buoyant convection. In both cases it is possible to have sharp interfaces with small scale turbulence.

The main body of the text is divided into two sections. The first is titled "Models of Ocean Turbulence," and it contains derivations and calculations that are needed to interpret the measurements described in the second section, which is titled "Analysis of Observations." Most of the important results are in the second section and

a reader very familiar with the subject of ocean microstructure may be able to read the second section with only occasional references to the first.

2. MODELS OF OCEAN TURBULENCE

In this section, several aspects of ocean turbulence are developed to be a guide for understanding field measurements. The coverage of the field is not complete, but certain subjects that appear to be relevant to the measurements are given detailed treatment. The first of these is salt finger convection, and it is given the most comprehensive discussion because much of the turbulence identified in the field data is attributed to this mechanism. A linear stability analysis is presented to show how salt fingers may occur in the ocean. Then another model, the equilibrium model, is used to see what conditions are necessary for salt fingers to persist in a quasi-steady state. Finally more realistic end conditions are imposed to complete the picture of the flow in the field of salt fingers and the turbulent convection that this flow drives.

The convective boundary layer that is coupled to salt fingers is shown to be an essential part of the system in the next part. Some models of turbulent convection are applied to this flow in an attempt to bring out its important features. The last two parts of the section are a brief description of turbulence generation by shear instability and a detailed calculation of the potential energy change that accompanies mixing in a stratified fluid.

2.1 Double Diffusive Convection

The instrument - SCIMP - (see Appendix A for instrument description), which obtained the ocean measurements of microstructure described here, was originally designed to photograph salt fingers in the ocean and substantiate their presence with concurrent CTD measurements. Before

considering the evidence for their presence, the characteristics of salt fingers will be summarized based on theoretical calculations and laboratory measurements. Although the properties of oceanic salt fingers cannot necessarily be extrapolated from linearized theoretical models and laboratory measurements at scales that are very different, they provide the best available framework to begin interpretation.

The physical principle that allows salt finger convection was first demonstrated by Stommel et al. with a simple thought experiment in 1956. It was based on the equation of state for sea water, by which the density of sea water is increased by an increase in salinity and decreased by an increase in temperature. This allows statically stable density distributions when the salinity decreases with depth as long as the temperature decreases fast enough to maintain increasing density. (Similarly temperature may increase with depth as long as the salinity increases rapidly enough to cause increasing density. Increasing temperature combined with decreasing salinity always leads to decreasing density and is unstable.) They envisioned a long diabatic pipe that could reach from the surface of the ocean to the base of the thermocline. In regions of the ocean where salinity as well as temperature decrease with depth, the salt represents a source of energy in the geopotential field, which may be liberated simply by falling, and the long pipe is an effective means of releasing this energy. If this pipe is situated in the ocean spanning the thermocline and primed by pumping some water out of the pipe at the surface, the flow will continue without any other external influence after the pumping is stopped, earning the name "perpetual salt fountain." As water rises

in the diabatic tube, it comes to thermal equilibrium with the surrounding water. Since it is less saline but the same temperature as the surroundings, it is lighter than its surroundings and there is an upward buoyancy force. As fluid rises the force increases until it reaches the top of the tube with its accumulated head and appears as a fountain. Naturally there are no diabatic tubes and viscous forces will limit the effectiveness of this mechanism. By following through the complimentary experiment where the tube is primed in the opposite direction, it can be seen that the salt fountain works equally well in either direction. Although this was just a thought experiment, there are several critical points that come from it:

(1) there is potential energy in a salinity distribution that decreases with depth

(2) this energy can be liberated by vertical fluid flow where heat transfer is allowed but salt flux is inhibited

(3) the energy release mechanism is symmetric in that both upward and downward motions are accelerated

(4) it is necessary that both temperature and salinity decrease in the direction of gravity.

The critical step in going from the "oceanographic curiosity" of the salt fountain to a potentially important mechanism in ocean dynamics was made by Stern in 1960. He realized that the pipe is unnecessary because the molecular diffusion of heat is very fast compared to salt. The diffusivity for heat is approximately 100 times greater than that for salt so that inefficient diffusion of salt takes the place of the pipe in the salt fountain. Then a fluid

particle that is displaced upward to where the surroundings are warmer and saltier will be heated by these surroundings but will gain relatively little salt, and hence the fluid particle will expand and its density will decrease. As it expands it rises to warmer surroundings increasing its temperature, specific volume and velocity. Ultimately the velocity of the particle is limited by viscous drag. The motion of the rising particle is maintained by heat that it removes from its surroundings, and this surrounding fluid must contract increasing its density and causing it to sink. This requirement plus the symmetry of the mechansim lead to a model with a close-packed arrangement of rising and sinking columns where each column is bounded on all sides by columns with flow in the opposite direction. The name salt fingers has been given to this flow, and in the laboratory the cross-section of the fingers is a quadralateral. When the field of fingers is subjected to shear, they may be transformed into lamellae (Linden, 1971). Salt fingers with triangular cross-section are another possible close-packed arrangement, but they have not been observed in this configuration.

There is another instability and flow that is complimentary to salt fingers and may occur when temperature, salinity and density all increase with depth. It is also called double diffusive convection because it depends on the relatively inefficient flux of salt compared to heat. This time when a fluid particle is displaced upward, the surroundings are cooler and less salty. There the particle gives up some of its heat, contracts and sinks beyond its equilibrium level by an amount greater than the original displacement. There it is

warmed, expands and rises again in a growing oscillation. This starting oscillation ultimately breaks down into turbulent convection (Shirtcliffe, 1967) and a quasi-steady state where there is a sharp horizontal interface maintained by turbulent convecting layers on either side of it. Because the fluxs across this interface appear to be carried by molecular diffusion (Turner, 1973), this flow has been named the diffusive mode of double diffusive convection.

2.1.1 Linear Stability Analysis

There are several important characteristics and scales that may be obtained from a linear analysis of double diffusive convection. These are derived as a guide for interpreting ocean measurements. Even though the ocean observations may not be in the parameter range where linear theory is applicable, better understanding of the physical principles and constraints should result. The analysis follows a presentation by N.P. Fofonoff in a class at W.H.O.I., and it includes results due to Stern (1960), Veronis (1965), and Baines and Gill (1969).

Consider a fluid that is stratified with linear gradients of temperature and salinity. The equation of state is also linear in the temperature, T, and the salinity, S, so that the density, ρ, is as before

$$\rho = \rho_0 \left[1 - \alpha (T - T_0) + \beta (S - S_0) \right] \quad (2.1)$$

where the subscript zero denotes a reference state. The coefficients of expansion at constant pressure, p, for temperature and salinity are respectively α and β, which are defined as above but here are restricted to being constant,

$$\alpha = -\frac{1}{\rho}\left(\frac{\partial \rho}{\partial T}\right)_{S,P} \quad , \quad \beta = \frac{1}{\rho}\left(\frac{\partial \rho}{\partial S}\right)_{T,P} \tag{2.2}$$

Consistent with the thought experiments described above, a spherical particle of water with radius, a, is taken initially in equilibrium with its stratified surroundings. This particle is then displaced vertically from equilibrium a distance ζ to a new position where the density of the surroundings, ρ_s , may be different than the density of the fluid particle, ρ . There is then a buoyancy force on the particle which tends to accelerate it. Balancing the buoyancy force with the particle acceleration gives

$$m \frac{d^2\zeta}{dt^2} = -g(\rho - \rho_s) V \tag{2.3}$$

where m is the mass of the particle, t is time, g is the acceleration of gravity, and V is the particle volume.

When the fluid particle moves relative to its surroundings, there is a drag force that retards it. If the relative motion is slow enough (Reynolds Number $<<$ 1) the drag force is linearly proportional to the velocity difference, Δu , and the drag force is given by a formula that is similar to Stokes formula (Landau and Lifshitz, 1959)

$$F = 5\pi \Delta u \mu a \tag{2.4}$$

where μ is the dynamic viscosity. If the surrounding fluid is at rest, then $\Delta u = \frac{d\zeta}{dt}$ and drag force can be written

$$F = 5\pi \frac{d\zeta}{dt} \mu a \tag{2.5}$$

Adding the drag force to the vertical momentum equation, (2.3),

$$m \frac{d^2 \zeta}{dt^2} = -g(\rho - \rho_s) V - 5\pi \mu a \frac{d\zeta}{dt} . \quad (2.6)$$

Using the fact that the particle is a sphere to calculate the volume, and the kinematic viscosity is $\nu = \mu/\rho$,

$$\frac{d^2 \zeta}{dt^2} + \frac{15}{4} \frac{\nu}{a^2} \frac{d\zeta}{dt} = -\frac{g}{\rho}(\rho - \rho_s) \quad (2.7)$$

The surroundings are linearly stratified in the vertical direction, (z), and the gradients are related by

$$\frac{d\rho_s}{dz} = -\alpha \frac{dT_s}{dz} + \beta \frac{dS_s}{dz} \quad (2.8)$$

$$= N_0^2 \frac{\rho_s}{g} \quad (2.9)$$

where N_0 is the constant surrounding buoyancy frequency to the Boussinesq approximation. The buoyancy force can be rewritten in terms of displacement using the equation of state, (2.1), and the Boussinesq approximation as

$$-\frac{g}{\rho}(\rho - \rho_s) = -N_0^2 \zeta + g\left[-\alpha(T - T_0) + \beta(S - S_0)\right] \quad (2.10)$$

which can then be substituted into the momentum equation, (2.7), to give

$$\frac{d^2 \zeta}{dt^2} + \frac{15\nu}{4a^2} \frac{d\zeta}{dt} + N_0^2 \zeta = g\left[-\alpha(T - T_0) + \beta(S - S_0)\right] \quad (2.11)$$

Taking the reference state (zero subscript) at t = 0 and $\zeta = 0$, the equation is homogeneous in the case of no heat or salt diffusion, i.e.,

$$T \equiv T_0 \quad , \quad S = S_0$$

This is equivalent to the limit of large Prandtl Number, $P_r = \nu/k_T$, and Schmidt Number, $S_c = \nu/k_s$, where k_T and k_S are the molecular diffusivities for heat and salt respectively. The homogeneous equation is a linear, second order, ordinary differential equation with constant coefficients, which is analogous to a damped harmonic oscillator. Oscillations are critically damped when

$$\frac{15\nu}{4a^2} = 2N_0 \tag{2.12a}$$

or

$$a^2 = \frac{15\nu}{8N_0} \tag{2.12b}$$

For $a^2 > \frac{15\nu}{8N_0}$, the system is over damped and motions of the system are described by exponential solutions with real negative exponents, while for $a^2 < \frac{15\nu}{8N_0}$ the exponents have imaginary parts, and the solution oscillates within an envelope that decreases with time. Using $\nu = 10^{-2}\ \frac{cm}{s}$ for sea water gives radii for critical damping shown below.

N_0 (Cycles/hr)	a (cm)
0.1	10.4
1	3.28
10	1.04
100	0.33

If there is diffusion of heat or salt then the equation is no longer homogeneous and there are other solutions. The temperature, T, and the salinity, S, are coupled to the displacement equation by the conservation equations for heat and salt. The one dimensional heat flow equation is

$$m c_p \frac{dT}{dt} = - A k \left.\frac{\partial T}{\partial r}\right|_{r=a} \qquad (2.13)$$

where A is the area of the fluid particle, and c_p and k are the specific heat and thermal conductivity. Again assuming a spherical shape and estimating the temperature gradient as

$$\left.\frac{\partial T}{\partial r}\right|_{r=a} \cong \frac{T - T_s}{a} \qquad (2.14)$$

$$= \frac{T - T_0 - \frac{dT_s}{dz} S}{a} \qquad (2.15)$$

then

$$\frac{dT}{dt} = - \frac{3 K_T}{a^2} \left(T - T_0 - \frac{dT_s}{dz} S\right) \qquad (2.16)$$

where $K_T = \frac{k}{\rho c_p}$. Defining $\lambda_T = \frac{3 K_T}{a^2}$,

$$\frac{dT}{dt} = -\lambda_T \left(T - T_0 - \frac{dT_s}{dz} S\right) \qquad (2.17)$$

Following the same reasoning for the salt flux gives

$$\frac{dS}{dt} = -\lambda_s \left(S - S_0 - \frac{dS_s}{dz} S\right) \qquad (2.18)$$

where $\lambda_s = 3D/\rho a^2$ and D is the diffusion coefficient for salt. Rearranging and defining new parameters, the heat flow, salt flux and vertical momentum equations can be written as

$$\frac{dT}{dt} + \lambda_T T - \lambda_T \frac{N_T^2}{\beta_T} S = \lambda_T T_0 \qquad (2.19)$$

$$\frac{dS}{dt} + \lambda_s S - \lambda_s \frac{N_s^2}{\beta_s} J = \lambda_s S_0 \qquad (2.20)$$

$$\frac{d^2 J}{dt^2} + \lambda_v \frac{dJ}{dt} + N_0^2 J - \beta_T T - \beta_s S = -\beta_T T_0 - \beta_s S_0 \qquad (2.21)$$

with the new parameters

$$\lambda_v = \frac{15\nu}{4a^2} \quad , \quad \beta_T = g\alpha \quad , \quad \beta_s = g\beta,$$

$$N_T^2 = \beta_T \frac{dT_s}{dz} \quad , \text{ and } \quad N_s = \beta_s \frac{dT_s}{dz} .$$

Note that the right-hand side of these equations, (2.19-2.21), are constants. The parameters N_T^2 and N_S^2 measure the stratification effects of temperature and salinity separately and their sum is the overall stability,

$$N_0^2 = N_T^2 + N_S^2 . \qquad (2.22)$$

To obtain the characteristic equation for the set of equations (2.19-2.21), the following time dependent behavior is assumed

$$J = J_0 e^{pt} \quad , \quad T = T_0 e^{pt} \quad , \quad S = S_0 e^{pt} \qquad (2.23)$$

Substituting these solutions and differentiating gives

$$(p + \lambda_T) T - \lambda_T \frac{N_T^2}{\beta_T} J = \lambda_T T_0 \qquad (2.24)$$

$$(P+\lambda_s)S - \lambda_s \frac{N_s^2}{\beta_s} J = \lambda_s S_0 \qquad (2.25)$$

$$(P^2 + \lambda_v P + N_0^2) J - \beta_T T - \beta_s S = -\beta_T T_0 - \beta_s S_0 \qquad (2.26)$$

The determinant of the coefficient matrix is after some manipulation given by

$$(P+\lambda_v)(P+\lambda_T)(P+\lambda_s) + N_0^2 P + \lambda_s N_T^2 + \lambda_T N_s^2 = 0 \qquad (2.27)$$

In the limit of $\lambda_v, \lambda_T, \lambda_s \to 0$, which may be $a^2 \to \infty$ or $\nu, \kappa_T, \kappa_s \to 0$, i.e., large mass or small molecular effects, the equation reduces to

$$P^3 + N_0^2 P = 0 \qquad (2.28)$$

which is an undamped oscillation with frequency N_0.

Defining a dimensionless growth rate

$$\chi = P/\lambda_T$$

and substituting gives the characteristic equation for the dimensionless growth rate

$$(\chi+\sigma)(\chi+1)(\chi+\tau) + R\sigma\chi + R_T\tau\sigma + R_s\sigma = 0 \qquad (2.29)$$

where

$$\sigma = \frac{\lambda_v}{\lambda_T} = \frac{15\nu/4a^2}{3\kappa_T/a^2} = \frac{5}{4} \times (\text{Prandtl No.})$$

$$\tau = \frac{\lambda_s}{\lambda_T} = \frac{\kappa_s}{\kappa_T} = (\text{Lewis No.})^{-1}$$

$$R = \frac{N_o^2 a^4}{9\nu \kappa_T} \quad , \quad R_T = \frac{N_T^2 a^4}{9\nu \kappa_T} \, , \quad R_S = \frac{N_S^2 a^4}{9\nu \kappa_S}$$

The parameters R, R_T, and R_S are analogous to the Rayleigh Number

$$R_a \equiv \frac{N_T^2 d^4}{\nu \kappa_T}$$

where d is a vertical length scale.

The characteristic equation is cubic and must have at least one real root. The other two roots may be real or complex conjugates. In the case of salt fingers, $R_S < 0$ and $R_T > 0$, the growth rate is zero when

$$\sigma\tau + R_T \tau\sigma + R_S \sigma = 0 \qquad (2.30)$$

while gravitational stability requires

$$R_T + R_S > 0 \qquad (2.31)$$

Figure 2.1 shows the portion of the R_T, R_S plane, which represents the combination of temperature and salinity gradients, where salt fingers are possible. The solid line $R_T = -R_S$ is a line of neutral gravitational stability. Solutions below that line are unstable. The dashed line represents the curve

$$R_T = -R_S/\tau - 1 \qquad (2.32)$$

Salt fingers are possible in the shaded region, which lies to the left of this line and above the neutral stability line. It is shown with a steep slope since $\tau = 10^{-2}$ for sea water. In the case of $|R_T| >> 1$,

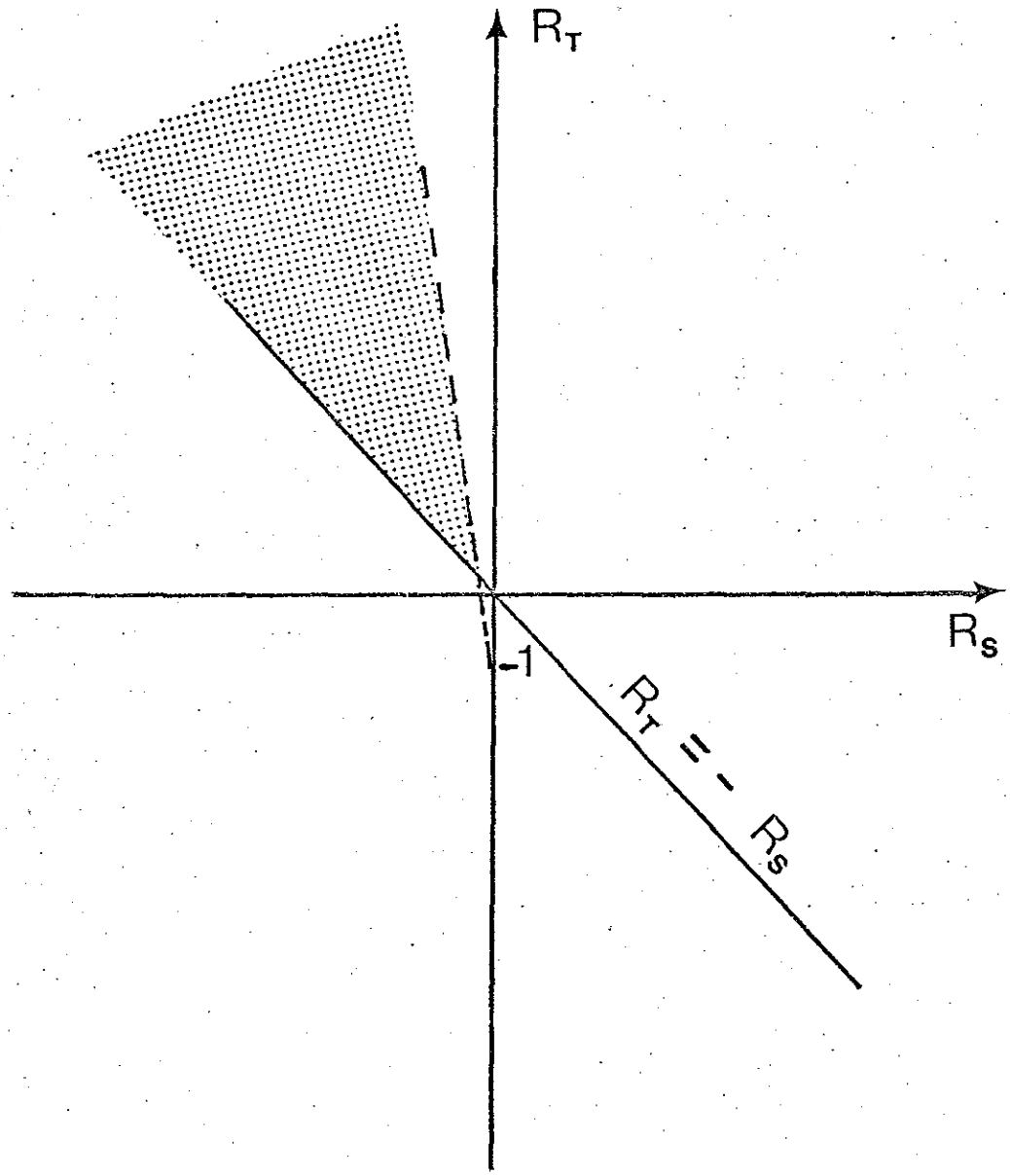

FIGURE 2.1 Illustration of the parameter range where salt fingers may exist. The lower boundary of the salt finger region is the line $R_T = -R_S$. Below this line the density distribution is gravitationally unstable. The right side of the salt finger region is the line $R_T = -\tau R_S - 1$. To the right of this line the salinity gradient is too weak to drive the convection.

which is the interesting oceanographic case where the fingers are not heavily damped by viscosity, the approximation

$$R_T < - R_S/\tau \tag{2.33}$$

is valid, or in terms of gradients

$$\frac{\beta \, dS_s/dz}{-\alpha \, dT_s/dz} > \tau \cong 10^{-2} \tag{2.34}$$

This states that one percent or more of the density stratification due to temperature is compensated by salinity, which is a very weak constraint in most oceanic situations.

The above analysis has shown what parameter ranges have small disturbances that grow, but it has not shown which salt fingers are most likely to be seen in nature. One criterion which may be applied is the largest growth rate to finite amplitude. Defining the function, f

$$f(x,\sigma,\tau) = \frac{(x+\sigma)(x+1)(x+\tau)}{\sigma} \tag{2.35}$$

and

$$y = -Rx - R_T\tau - R_S \tag{2.36}$$

then

$$f - y = 0. \tag{2.37}$$

is a solution to the characteristic equation. The function f is a cubic polynomial with roots at $x = -1, -\sigma, -\tau$, and it is sketched in Figure 2.2. Since $\tau << 1$ and $\sigma > 1$ for sea water the function f can be approximated for small x as

$$f \cong x \tag{2.38}$$

while, some manipulation leads to another form for y

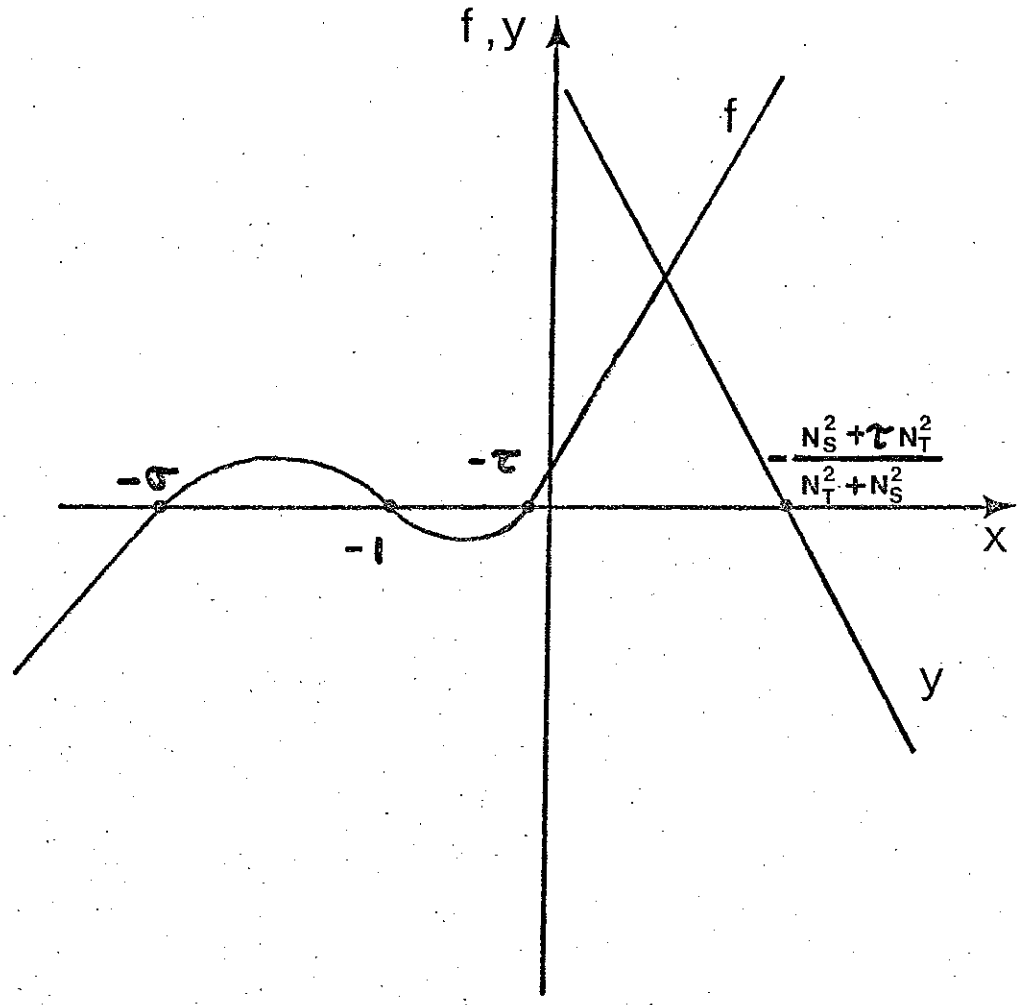

FIGURE 2.2 Graphical solution for the fastest growing infinitessimal salt finger. Intersection of the two curves (2.35) and (2.36) gives the solution (2.37).

$$y = -R\left(\chi + \frac{N_S^2 + \tau N_T^2}{N_T^2 + N_S^2}\right) \tag{2.39}$$

For positive growth rate, the solution is

$$\chi = -\frac{R_S}{1+R} \tag{2.40}$$

or in dimensional terms

$$\rho = -\frac{N_S^2 \lambda_T}{N_0^2 + \sigma \lambda_S^2} \tag{2.41}$$

This growth rate is a maximum at

$$N_0^2 = \sigma \lambda_T^2 \tag{2.42}$$

in terms of finger radius

$$a^4 = \frac{9\sigma \kappa_T^2}{N_0^2} \tag{2.43}$$

Using $\sigma = 10$, $\kappa_T = 10^{-3} \frac{cm^2}{s}$, this formula can be used to estimate salt finger radii

N (cph)	a (cm)
0.1	7.4
1.0	2.3
10.0	0.74
100.0	0.23

In summary, linear stability gives the following useful results for salt fingers in the oceanic parameter range:

(1) Salt fingers are possible when temperature and salinity both decrease with depth.

(2) The gradients of temperature and salinity must be statically stable with at least one percent (τ) of the temperature stratification compensated by salt.

(3) The horizontal length scale of the fastest growing salt fingers is near one centimeter in the stability range 1-10 cph.

2.1.2 Equilibrium Model for Salt Fingers

The linear stability analysis describes the physical principles that lend to the instability and can be used to estimate a horizontal length scale with a maximum growth rate. Another approach to the problem is to assume that the salt finger field has been set up and is steady. The dimensions and transports of such a system can then be evaluated. In particular, ratio of the heat flux to the salt flux can be calculated along with the rate at which potential energy is released by the salt finger system, i.e., the buoyancy flux. Also the salt finger diameter is estimated for steady flow. This model was first described by Stern (1969), and it has been developed by Lambert and Demenkow (1972) and Huppert and Manins (1973).

Consider vertical gradients of temperature and salinity dT_s/dz, dS_s/dz where the notation is the same as above except when noted. These gradients are such that the temperature, T_s, the salinity, S_s, and the specific volume, $1/\rho_s$, all decrease with depth. There are salt fingers present and the steady vertical momentum equation can be written to the Boussinesq approximation as

$$0 = -\frac{1}{\rho_0}\frac{d\rho}{dz} + \nu \nabla_H^2 w - g\left[1 + \beta(S-S_0) - \alpha(T-T_0)\right] \tag{2.44}$$

where p is the pressure, w is the velocity in the z direction and $\nabla_H^2 = \frac{\partial^2}{\partial x^2} + \frac{\partial^2}{\partial y^2}$ is the horizontal Laplacian. Conservation of heat and salt require that advection and diffusion balance in steady state, so

$$w \frac{dT}{dz} = K_T \nabla^2 T \tag{2.45a}$$

$$w \frac{dS}{dz} = K_S \nabla^2 S \tag{2.45b}$$

The solution is separated a horizontally averaged part, which is a function only of z, and a fluctuation that depends on x and y

$$\begin{aligned} w &= w(x,y) \\ T &= T_s(z) + T'(x,y) \\ S &= S_s(z) + S'(x,y) \end{aligned} \tag{2.46}$$

where the horizontal averages are $\overline{w} = 0$, $\overline{T} = T_s$ and $\overline{S} = S_s$. From the horizontal momenutm equations, $\frac{\partial p}{\partial x} = \frac{\partial p}{\partial y} = 0$ in steady flow, and the horizontally averaged vertical momentum equation is hydrostatic,

$$0 = -\frac{1}{\rho_0} \frac{d\overline{p}}{dz} - g\left[1 + \beta(S_s - S_0) - \alpha(T_s - T_0)\right]. \tag{2.47}$$

When (2.47) subtracted from the unaveraged equation (2.44), the remainder is

$$0 = \nu \nabla_H^2 w - g(\beta S' - \alpha T'). \tag{2.48}$$

Substituting the separation (2.46) into the conservation equations (2.45)

$$w \frac{dT_s}{dz} = K_T \left(\frac{d^2 T_s}{dz^2} + \nabla_H^2 T' \right) \tag{2.49a}$$

$$w \frac{dS_s}{dz} = K_S \left(\frac{d^2 S_s}{dz^2} + \nabla_H^2 S' \right) \tag{2.49b}$$

Since $\overline{w}, \overline{T'}, \overline{S'} = 0$, the horizontal average of these equations can be used to infer that

$$\frac{d^2 T_s}{dz^2} = \frac{d^2 S_s}{dz^2} = 0 \tag{2.50}$$

or the mean gradients are constant and (2.49) can then be rewritten

$$w \frac{dT_s}{dz} = K_T \nabla_H^2 T' \tag{2.51a}$$

$$w \frac{dS_s}{dz} = K_S \nabla_H^2 S' \tag{2.51b}$$

The set of equations (2.48) and (2.51) is now linear and can be separated into the following solutions

$$(w, T', S') = (-w_*, T_*, S_*) \sin \frac{x}{L} \sin \frac{y}{L} \tag{2.52}$$

where L/π is the length of a side of a single square cross section salt finger. A square cross section has been assumed to agree with laboratory observations of Shirtcliff and Turner (1970). Substituting (2.52) into (2.48) and (2.51) gives the relations among the amplitudes

$$0 = -2\nu \frac{w_*}{L^2} - g(\beta S_* - \alpha T_*) \tag{2.53a}$$

$$-w_* \frac{dT_s}{dz} = -2 K_T \frac{T_*}{L^2} \tag{2.53b}$$

$$-W_* \frac{dS_s}{dz} = -2K_s \frac{S_*}{L^2} \qquad (2.53c)$$

At any level the horizontally averaged convective heat flux is $F_T = \overline{wT'}$ and the salt flux $F_S = \overline{wS'}$. These fluxes can be evaluated by integrating over a pair of fingers using (2.52) to specify the distributions. The buoyancy fluxes due to heat, αF_T, and salt, βF_S, have the ratio

$$r = \frac{\alpha F_T}{\beta F_S} = \frac{\alpha T_*}{\beta S_*} \qquad (2.54)$$

Since the system is driven by the downward flux of salt, $r<1$ and the buoyance flux, $F_B = \beta F_S(1-r)$. Using (2.53b) and (2.53c), r can be written in terms of the mean gradients as

$$r = \tau \frac{\alpha\, dT_s/dz}{\beta\, dS_s/dz} \qquad (2.55)$$

From (2.53) and (2.55) an expression for the finger width is obtained

$$L = \left[\frac{4\nu K_T}{g\alpha\, dT_s/dz}\left(\frac{r}{1-r}\right)\right]^{1/4} \qquad (2.56)$$

which is similar in form to the scale derived from the linear stability anslysis, (2.43). The flux ratio r must be inferred from laboratory experiments which do not exactly fit the conditions assumed by the analysis. Turner (1967) suggests a value r = 0.56, while Linden (1973) finds r = 0.1 a better estimate under equilibrium conditions. Neither set of measurements duplicates oceanic conditions where $\frac{\alpha\, dT_s/dz}{\beta\, dS_s/dz} \cong 1$, i.e., the stability is low.

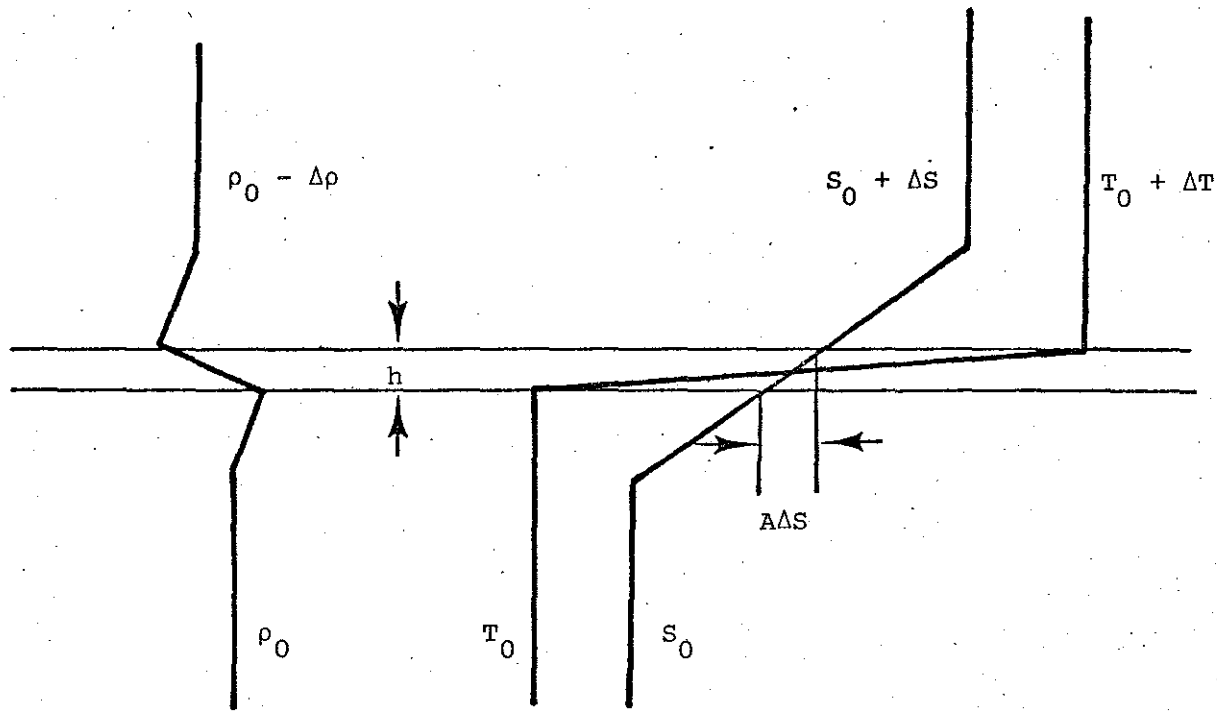

FIGURE 2.3 Schematic representation of salt fingering interface and convecting layer system. The temperature changes by an amount ΔT and the salinity by $A\Delta S$ across the interface with thickness h. Note that the density distribution is unstable above and below the interface where temperature is constant and salinity increases with depth.

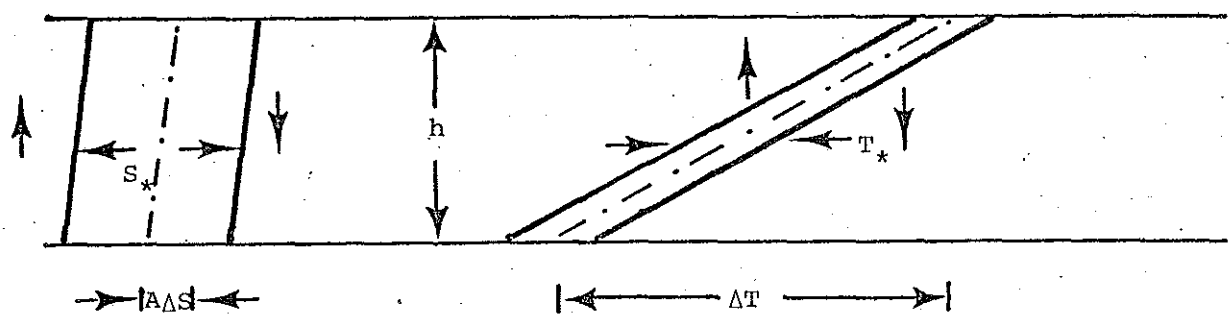

FIGURE 2.4 Temperature and salinity profiles within rising and sinking fingers. The direction of the flow is indicated by the arrow beside each profile. At any level the temperature and salinity differences are T_* and S_*. The system is analogous to a counterflow heat exchanger but there is relatively little salt diffusion.

2.1.3 Finite Length Effects

The equilibrium model is independent of depth so it assumes that the salt fingers are infinitely long. Naturally, the length of salt fingers is limited and a proper model should take this into account. The above analysis may be locally valid near the midplane of a field of salt fingers if it is sufficiently far from the ends. Naturally occurring salt fingers seem to have a nearly constant temperature gradient core with a poorly defined transition zone at either end of the core. In the ocean uniform regions of nearly constant temperature and salinity are often found beyond the transition zones which appear to be mixed by the unstable buoyancy flux from the fingers. The salinity structure in the core or in the transition zones has never been measured and is poorly understood, but some reasonable guess can be made to extend the applicability of the model to finite length fingers.

The proposed model now has a core with thickness, h, where equations (2.48) and (2.51) govern the dynamics, and there are transition layers above and below which are as yet unprescribed. Assuming that most of the temperature change takes place across the core while a significant fraction of the salinity change takes place across the transition layers (2.57)

$$\frac{dT_\xi}{d\xi} \cong \frac{\Delta T}{h} \quad , \quad S_* = A\Delta S \, , \quad A<1$$

where ΔT and ΔS are the temperature and salinity differences between two mixed layers. The factor A is the fraction of the total salinity that occurs across the core. See Figure 2.3.

To evaluate the fluxes due to salt fingers explicitly, recourse must be made to laboratory measurements. Formally the fluxes in the equilibrium model can be integrated to

$$\alpha F_T = \frac{\alpha w_* T_*}{4} \quad , \quad \beta F_S = \frac{\beta w_* S_*}{4} \tag{2.58}$$

but the vertical velocity scale, w_* , is unknown and not easily measured in the ocean. Turner (1967) has used a dimensional argument to estimate the fluxes without directly measuring the vertical velocity. The estimate is a direct analogy to thermal convection at high Rayleigh Number (Chandrasekhar, 1961), where the form of the Nusselt Number, Nu, depends only on the Rayleigh Number and fluid properties, i.e.,

$$Nu = \frac{F_T}{k\,\Delta T/d} = f_n\left(\frac{g\alpha\Delta T}{\nu\kappa_T} d^4, \text{ fluid properties}\right) \tag{2.59}$$

In the case of an unbounded fluid, there is no dependence on an external length scale and the form of the flux law which satisfies this requirement is

$$Nu = C_1 (Ra)^{1/3} \tag{2.60a}$$

or

$$F_T = C_2 (\alpha \Delta T)^{4/3} \tag{2.60b}$$

where C_1 and C_2 are functions of fluid properties. The analogous form for the salt flux by salt finger convection is

$$\beta F_S = C(\beta \Delta S)^{4/3} \tag{2.61}$$

where C is a function of fluid properties and the parameter, $\alpha\Delta T/\beta\Delta S$,

the Turner Number. Using this expression with (2.57) in (2.58) to calculate the vertical velocity scale gives

$$w_* = \frac{4C}{A}(\beta\Delta S)^{1/3} \tag{2.62}$$

implying that the vertical velocity is a weak function of the salinity difference. This scale can be used with (2.53a) and (2.54) to obtain another relationship for vertical velocity

$$w_* = \frac{L^2 g}{2\nu}\beta S_*(1-r) \tag{2.63a}$$

or, with the aid of (2.57)

$$w_* = \frac{L^2 g A}{2\nu}(\beta\Delta S)(1-r) \tag{2.63b}$$

Eliminating w_* between (2.62) and (2.63) gives an alternate relationship for finger diameter,

$$L = \left[\frac{8\nu C}{g A^2 (1-r)}\right]^{1/2}(\beta\Delta S)^{-1/3} \tag{2.64}$$

Superficially, (2.64) is easier to evaluate than its counterpart in terms of temperature gradient, (2.56), because the salinity difference between two convecting layers should be relatively easy to measure with conventional profiling instruments. However, the two additional coefficients C and A are poorly measured quantities and there are no reliable estimates for the parameter range found in the ocean. Turner (1967) found that C increases with decreasing $\alpha\Delta T/\beta\Delta S$ in the range $2 < \frac{\alpha\Delta T}{\beta\Delta S} < 10$ and extrapolates $C \cong 0.1$ cm/s for $\alpha\Delta T/\beta\Delta S \cong 1$, which corresponds to ocean conditions. The factor A has been estimated by Linden (1973) as 0.5, but this appears to

be little more than a reasonable guess because physically $0 \leq A \leq 1$. Again the finger diameter in (2.64) depends on the flux ratio, r, which is not a well established coefficient for Turner Number near one.

In all of the above models the length scale that has been evaluated is the horizontal length scale or finger width. Although this is a measured quantity in the measurements described here, the quantification is marginal. In all cases but one, estimates must be made subjectively and are probably not good to much better than a factor of two. This combined with the 1/4 or 1/3 power dependence on most parameters make L an inconclusive quantity. A length scale that is more accurately measured is the length of the fingers, h, making it an important parameter to derive from the dynamical equations.

Using the approximation $dT_s/dz = \frac{\Delta T}{h}$, the finger width, (2.56), is rewritten as

$$L = \left[\frac{4\nu k_T h}{g\alpha\Delta T}\left(\frac{r}{1-r}\right)\right]^{1/4} \qquad (2.65)$$

but (2.64) can be used to eliminate L in favor of ΔS , then

$$h = \frac{16\nu C^2}{k_T A^4 r(1-r)} \frac{\alpha\Delta T}{\beta\Delta S}\left(\beta\Delta S\right)^{-1/3} \qquad (2.66)$$

To complete the evaluation of h, the dependence of the salt flux scale, C, on $\alpha\Delta T/\beta\Delta S$ must be determined. Linden's (1973) direct measurements suggest a linear flux gradient relationship across the interface in the form

$$\beta F_S = K_S \frac{\beta\Delta S}{h} \qquad (2.67)$$

where K_s is an eddy exchange coefficient defined by the above equation.

Then

$$C(\beta\Delta S)^{4/3} = K_S \frac{\beta\Delta S}{h} \tag{2.68a}$$

or

$$h = \frac{K_S}{C}(\beta\Delta S)^{-1/3} \tag{2.68b}$$

Eliminating C in (2.66) gives

$$h = (16)^{1/3}\left(\frac{\nu}{g k_T}\right)^{1/3}\left[\frac{K_S^2}{A^4 r(1-r)}\right]^{1/3}\left(\frac{\alpha\Delta T}{\beta\Delta S}\right)^{1/3}(\beta\Delta S)^{-1/3} \tag{2.69}$$

By using an empirical result from the laboratory, (2.67), one partially known function has been substituted for another, but the term in the brackets remains virtually unmeasured. Under oceanic conditions, the remaining parameters in (2.69) are either well known physical coefficients or measurable quantities. The expression for h, (2.66), will be tested against measurements of salt fingers in the ocean.

The above discussion has been based on the ad hoc assumption that the salt fingers have finite length, h. A physical explanation for this behavior has been offered by Stern (1969) and termed "collective instability". According to the model, salt fingers become unstable to small amplitude disturbances with long horizontal wavelengths (compared to a salt finger diameter) such as an internal wave. The shear associated with the long waves tilts the field salt fingers from vertical and results in horizontal variations in salt flux which become unstable and limits the length of the salt fingers. The criterion for unstability is expressed in terms of a maximum buoyancy flux

$$\frac{\beta F_S - \alpha F_T}{\nu\left(\alpha\, dT/dz - \beta\, dS/dz\right)} \leq D \tag{2.70}$$

where D is a dimensionless number of order one. In the oceanic case $K_S \ll K_T$, $\alpha\, dT/dz \gg \beta\, dS/dz$ through the salt finger field, excluding the transition layers; then neglecting the salinity gradient in the denominator gives

$$\frac{\beta F_S (1-r)}{\nu \alpha\, dT/dz} \leq D \tag{2.71}$$

This expression can be used to give another estimate for interface thickness. Using $dT/dz = \frac{\Delta T}{h}$ gives

$$h \leq \frac{D\nu \alpha \Delta T}{\beta F_S (1-r)} \tag{2.72}$$

or using the power law expression for the salt flux, (2.61) to eliminate βF_S gives

$$h \leq \frac{D\nu}{C(1-r)} \left(\frac{\alpha \Delta T}{\beta \Delta S}\right) (\beta \Delta S)^{-1/3} \tag{2.73}$$

Comparing (2.66) and (2.73), the functional dependency on the external parameters, $\alpha \Delta T / \beta \Delta S$ and $\beta \Delta S$ is identical, while the assumptions that led to them are seemingly different. In the former case the salinity differences between adjacent fingers is assumed to be a constant fraction, A, of the total between layers and the dynamics of the fingers are described by (2.48) and (2.51). The latter is based on a linear relation between buoyancy flux and density gradient within the fingering region, while both use $dT/dz = \Delta T/h$ and $\beta F_S = C(\beta \Delta S)^{4/3}$.

In the model of salt finger convection on thin interfaces mixing deep layers on either side, the equilibrium thickness of these layers must be determined by the conditions at the interface. Layer thickness is related to the mean salinity gradient by

$$H = \frac{\Delta S}{dS_s/dz} \tag{2.74}$$

so that H is determined by the salinity step across an interface. The salinity difference ΔS is greater than the salinity difference between two adjacent fingers because it includes the difference across the transition region as well as the core. Since the layers are mixed by the unstable buoyancy flux across the interface, the layer thickness must be related to the interface conditions but (2.74) is a strict constraint if the mean salinity gradient dS_s/dz is assumed to be externally imposed.

Formal substitution of the salt flux law (2.61) into (2.74) gives

$$H = \frac{(\beta F_s/C)^{3/4}}{\beta\, dS_s/dz} \tag{2.75}$$

and using the critical salt flux (2.71) from the collective instability model, then

$$H \le \left(\frac{D\nu}{(1-r)}\frac{\alpha\Delta T/h}{C}\right)^{3/4}\left(\beta\, dS_s/dz\right)^{-1} \tag{2.76}$$

The approximation $\frac{\alpha\Delta T}{h}\left(\beta\, dS_s/dz\right)^{-1} = \alpha\Delta T/\beta\Delta S$ leads to

$$H \le \left(\frac{D\nu}{(1-r)C}\right)^{3/4}\left(\frac{\alpha\Delta T}{\beta\Delta S}\right)\left(\frac{\alpha\Delta T}{h}\right)^{-1/4} \tag{2.77}$$

or in terms of the mean salinity gradient,

$$H \le \left(\frac{D\nu}{(1-r)C}\,\frac{\alpha\Delta T}{\beta\Delta S}\right)^{3/4}\left(\frac{\beta\, dS_s}{dz}\right)^{-1/4} \tag{2.78}$$

These last two relations can be tested with ocean data to see if they are adequate descriptions. Again the poorly measured coefficients, D, C, and r may preclude a definitive evaluation, but a consistency check can be made over the parameter range found.

The concept of an eddy diffusivity has proven useful in many turbulence problems. Formally, the eddy diffusion coefficient, K, is defined as the ratio of the flux to the mean gradient. For the case of buoyancy flux due to salt, the eddy coefficient is

$$K_S = \frac{\beta F_S}{\beta \, dS_S/dz} \tag{2.79}$$

By using the 4/3 power flux law and the thin interface approximation, $h << H$,

$$K_S = C H (\beta \Delta S)^{1/3} \tag{2.80}$$

or the eddy diffusivity is directly proportional to the layer thickness and a weak function of the salinity difference across an interface. The corresponding eddy diffusivity for heat is

$$K_T = \frac{\alpha F_T}{\alpha \, dT_S/dz} = \frac{r}{\alpha \Delta T/\beta \Delta S} K_S \tag{2.81}$$

which is less than K_S since $r<1$ and $\alpha \Delta T/\beta \Delta S > 1$.

An alternative expression for the eddy diffusivity is obtained by using the critical salt flux from the collective instability model. Then

$$K_S = D \nu (1-r) \frac{\alpha \, dT/dz}{\beta \, dS_S/dz} \tag{2.82}$$

Substituting $dT/dz = \Delta T/h$ for the critical temperature gradient

and using the same approximation before for the mean salinity gradient gives

$$K_S = D\nu\,(1-r)\,\frac{\alpha\Delta T}{\beta\Delta S}\,\frac{H}{h} \tag{2.83a}$$

and

$$K_T = D\nu(1-r)\,r\,H/h \tag{2.83b}$$

This again shows that the eddy diffusivity is proportional to the layer thickness but introduces an additional dependence on the inverse of the interface thickness. It is interesting to note that the magnitude of the salinity difference across an interface does not enter explicity in this form.

This is the end of the section that explicity discusses the dynamics of salt fingers. Before going on to describe some of the interactions between the field of salt fingers and the surroundings, it may be helpful to summarize the important characteristics of salt fingers and those than can be compared with ocean data.

By assuming steady flow and separating the motion into one part that depends only on z and another that depends only on x and y, the equilibrium model shows that the ratio of the buoyancy flux due to heat, αF_T , to the buoyancy flux due to salt, βF_S , can be written in terms of the mean gradients as

$$r = \frac{\alpha F_T}{\beta F_S} = \tau\,\frac{\alpha\, dT_s/dz}{\beta\, dS_s/dz} \tag{2.55}$$

Also the salt finger width, L, depends on this ratio and the mean temperature gradient in the form

$$L = \left[\frac{4\nu K_T}{g\alpha\, d\bar{T}_s/dz}\left(\frac{r}{1-r}\right)\right]^{1/4} \qquad (2.56)$$

When the salt fingers are restricted to a finite length, h, this length can be evaluated with additional assumptions as

$$h = \frac{16\nu C^2}{K_T A^2 r(1-r)}\left(\frac{\alpha\Delta T}{\beta\Delta S}\right)(\beta\Delta S)^{-1/3} \qquad (2.66)$$

and with a mixed layer and sharp interface system, the layer thickness is restricted to

$$H \leq \left[\frac{D\nu}{(1-r)C}\right]^{3/4}\left(\frac{\alpha\Delta T}{\beta\Delta S}\right)\left(\frac{\alpha\Delta T}{h}\right)^{-1/4} \qquad (2.77)$$

2.2 Transition Zone as a Convective Boundary Layer

That region in the salt finger convection system which is neither laminar salt fingers nor convecting layers is the transition zone. It is the boundary layer between interface and mixed layer matching incompatible features of each. The interface seems to be fairly well described by the equilibrium model for salt fingers with suitable adjustments for finite length effects, while the convecting layers are essentially passive in the system and are less critical for an understanding of the dynamics. By comparison, the transition zone determines most of the important characteristics of the system, and it is the least well understood of the regions.

The transition zone is a most difficult turbulent boundary layer to understand because it is unsteady, and it is driven by several forces which may dominate the behavior at different times. These forces are related to the many functions that the transition zone performs in the salt finger interface - convecting layer system.

The transition zone is both a source for fluid entering the salt fingers and a sink for emergent fluid. This dual role seems impossible in steady state, but somehow the exchange is performed. Again though the actual mechanics are vague, it seems very likely that the fluid entering the fingers has been modified from the condition when it was within the mixed layer. Likewise the fluid released into the mixed layer has somewhat different properties than the fluid emerging from the salt fingers. Thus the transition zone is a region where complicated mixing events take place with at least two specific fluid inflows and two outflows.

Another characteristic of the transition zone, which is implicit from the discussion above, is its role as both source and sink of the sporadic plumes that maintain the convecting layers. Again the specifics of the mechanism are unclear, but flux continuity requires transport across the homogeneous layers and visual observations suggest that this is the natural mode.

There are obvious restrictions placed on these flows within the transition zone by the conservation laws for mass, heat and salt, but there are also exchanges of momentum and energy. Both fluid leaving the salt fingers and the plumes arriving at the transition zone have kinetic energy and vertical momentum, while density anomalies created by the salt fingers are capable of doing work within the transition zone. The energy from these sources must be transformed, radiated away or dissipated.

2.2.1 Conservation Equations in the Transition Zone

Mass

If the size of the transition zone remains constant in the mean, then the mass of fluid entering the transition zone through salt fingers is equal to the mass leaving through salt fingers. As a result, in steady state the outflow due to sporadic plumes must be balanced by an inflow from the neighboring layer, which may be thought of as plumes released by the transition zone on the other side of the convecting layer. Then the mass flux into the boundary layer due to salt fingers equals that out

$$\dot{m}_{fi} = \dot{m}_{fo} = \dot{m}_f \tag{2.84}$$

and similarly the mass flow out due to sporadic plumes, $\dot{m}_p$, is balanced by an inflow from the adjacent layer.

Heat

In steady state, the net heat inflow of the entering and leaving salt fingers must be balanced by the heat flow out in the sporadic plumes less the inflow required by continuity. Calling T_1 the mean temperature of the entering salt fingers, T_2 the temperature of the leaving salt fingers, T_3 the temperature of the leaving plume and T_4 the temperature of the replacement flow from the adjacent layer

$$\dot{m}_f (T_1 - T_2) = \dot{m}_p (T_4 - T_3) \tag{2.85}$$

Note that this is also the average vertical heat flux in the fingers and the layers, F_T. This estimate has tacitly assumed that the two contributions to the heat flow from conduction along the salt fingers balance.

Salt

Completely analogous to the heat balance is the salt balance

$$\dot{m}_f (S_1 - S_2) = \dot{m}_p (S_4 - S_3) \tag{2.86}$$

where the subscripts on salinity have the same meaning as those on temperature. The buoyancy flux ratio, written in terms of these advective transports in the transition zone is

$$\frac{\alpha F_T}{\beta F_S} = r = \frac{\dot{m}_f \alpha (T_1 - T_2)}{\dot{m}_f \beta (S_1 - S_2)} \tag{2.87}$$

in the present notation. Using the heat and salt balances, this ratio can be expressed in terms of the plume properties as

$$r = \frac{\alpha (T_4 - T_3)}{\beta (S_4 - S_3)} \tag{2.88}$$

or the temperature and salinity differences between plume and layer have the same ratio as the difference between adjacent fingers. Further there is the obvious result for the mass flux ratio

$$\frac{\dot{m}_p}{\dot{m}_f} = \frac{T_1 - T_2}{T_4 - T_3} = \frac{S_1 - S_2}{S_4 - S_3} \tag{2.89}$$

Within the context of the similarity model for salt fingers, $T_1 - T_2$ is proportional to T_* and $S_1 - S_2$ is proportional to S_* making (2.87) consistent with the original definition of the flux ratio (2.54).

2.2.2 Convecting Layers

The potential energy that is released by salt finger convection stirs the layers on either side of the interface, but ultimately this energy must be dissipated or radiated away in steady state. While a certain fraction of the energy may be used to raise the center of

gravity of the layer, there is also kinetic energy contained in intermittent plumes that traverse the mixed layers and the fate of this energy is uncertain.

Each salt fingering interface releases an amount of potential energy per unit mass at a rate

$$b = g \beta F_s (1-r) \tag{2.90}$$

Assuming the interfaces are thin compared to the layers, $\delta << H$, the energy flux per unit area is

$$B = \rho_0 g \beta F_s (1-r) H \tag{2.91}$$

Suppose that this buoyant work is converted to turbulent mechanical energy which is dissipated at a rate

$$\epsilon = u^3/\ell \tag{2.92}$$

where u is the scale of turbulent velocity fluctuations and ℓ is the length scale of the turbulence. Setting $\ell = H$ and $\epsilon = b$, the turbulent velocity scale is

$$u = \left[g H \beta F_s (1-r) \right]^{1/3} \tag{2.93}$$

Although this estimate may be valid, it does not account for energy radiated away or work that lifts the center of gravity of the layer. It also does not depend on the particular mechanism by which the potential energy of stratification is converted to turbulence.

The fluid emerging from salt fingers has both kinetic energy due to its vertical velocity and potential energy due to its density anomaly. Both of these have a length scale of a finger diameter, L, and cannot directly excite motions in the mixed layer with a length scale $H >> L$. Instead the emergent fluid is modified within the

transition zone that exists on either side of the salt finger field. The transition zone is the important link that allows salt fingers to communicate with the convecting layers, but so far there has been no mathematical descriptions of the region. Visual observations of laboratory experiments have provided some insights and are presently the only recourse.

Like other types of buoyant convection, the transition zones in salt finger convection aggregate fluid until it rises or sinks in a larger mass. The net effect is that relatively large plumes or blobs of fluid intermittently leave the interface and rise or sink according to their density anomaly. This behavior has been reported by Stern and Turner (1969). If the layers are uniform in density, then the blobs will continue to rise or sink until they impact the next interface, or, more properly, the transition zone associated with the next interface.

If the system of salt fingers and convecting layers is steady and horizontally homogeneous, then heat and salt flux must be carried by the blobs as well as the salt fingering interfaces and the transition zones. And if the blobs can be identified in the ocean and measured, then estimates of the fluxes can be made directly. First the dynamics of the blobs are examined to see how they might be expected to appear in the ocean.

The elements that eventually break away to float or sink through the convecting layers are formed in the transition zone. Since that region is presently poorly understood, the characteristics of the blobs are difficult to predict. But if they are to transport heat and salt,

there must be anomalies of these properties compared to the homogeneous layers. Also part of the potential energy of the density anomaly must be converted to the mechanical energy which keeps the layer mixed. Assuming that the salt is transported vertically by spherical blobs each with a salinity anomaly δS compared to the layer they traverse,

$$\beta F_s = 4/3\, \pi\, d^3/8\, \beta \delta S f \qquad (2.94)$$

where d is the blob diameter and f is the number of blobs per square centimeter per second crossing a horizontal plane. As the blobs move across the convecting layer, they grow due to entrainment, diluting the salinity anomaly. Part of the potential energy is converted into kinetic energy of the mean motion while some mixes the layer.

The buoyant elements can be modeled as instaneaneous, isolated sources of buoyancy on the basis of laboratory observations. As such they are expected to become self-preserving so that the diameter increases linearly with distance from the point of departure in the transition zone, i.e.

$$d = k z \qquad (2.95)$$

Turner (1972) has made a systematic study of self-preserving flows due to point and line sources of buoyancy and the instantaneous plume or "thermal" is one of these flows. The density anomaly in terms of reduced gravity, g', and the mean vertical velocity of the plume, w, can then be represented as power law functions

$$g' = g\left(\frac{\rho_s - \rho}{\rho_s}\right) = G z^p \qquad (2.96a)$$

$$w = W z^q \qquad (2.96b)$$

By balancing the buoyancy force with the change of momentum of the fluid element, a relationship between the powers p and q can be derived. Setting the buoyancy force g'V equal to the time rate of change of momentum, P, gives

$$g'V = \frac{dP}{dt} = w\frac{dP}{dz} \tag{2.97}$$

Since $V \propto z^3$, and $P = \rho V w \propto z^{q+3}$, (the effect of density change on momentum is neglected, consistent with the Boussinesq approximation), the vertical momentum balance (2.97) places the following dimensional requirement on the exponents

$$p = 2q - 1 \tag{2.98}$$

There are many possible descriptions of the plume dynamics all of which satisfy the momentum equation, but have different entrainment characteristics and environmental density distributions (see Turner, 1972). In the case where the density of the layer is constant, which is true in the fully developed salt finger and convecting layer system, the linear growth of the plume is accompanied by a z^{-3} dilution of the density anomaly. Then the exponent of the vertical velocity is

$$q = \frac{p+1}{2} = -1 \tag{2.99}$$

or the velocity decreases linearly with height.

When the element of fluid of anomalous density leaves the transition to rise or sink through the homogeneous layer, it has a certain amount of potential energy. Under the assumptions above, the amount of this energy which is converted into kinetic energy of the mean motion of the plume can be calculated, as well as that which is lost

directly to other motions in the layer. The potential energy of an element of fluid with anomalous density within the transition zone is

$$(PE)_o = g\,|\rho - \rho_s|\,V_o\,H \qquad (2.100)$$

where V_o is its volume, $\rho - \rho_s$ is the density anomaly compared to ρ_s which is the density of the layer below in the case of a heavy element about to sink or the layer above in the case of light element about to rise. In either case H is the thickness of layer it must traverse to lose its potential energy. When the element leaves the transition zone, it must acquire a mean vertical velocity and possibly an internal circulation at the expense of part of its potential energy. During this initial acceleration period, the similarity model may not be applicable, but the element will probably grow and hence be diluted as it emerges from the transition zone. The size of these elements when they emerge is unknown for conditions in the ocean, but there may be evidence in the CTD profiles that will help to quantify these buoyant elements.

Assuming they emerge with a diameter d_1, vertical velocity W_1 and density anomaly $\Delta\rho_1$, then

$$g_1' = g\,\frac{\Delta\rho_1}{\rho_o} \qquad (2.101)$$

is the initial reduced gravity and buoyant force is

$$F_1 = g_1' V_1 = \pi/6\; g_1' d_1^3 \qquad (2.102)$$

for a spherical element. The kinetic energy of the blob is then

$$(KE)_1 = d_1^3\left(\frac{\pi}{12}\right)\rho W_1^2 \qquad (2.103)$$

As the blob crosses the constant density layer, the total buoyant force on it remains the same while its diameter increases linearly and the velocity decreases at the same rate. Since

$$KE \propto d^3 w^2 \propto z \tag{2.104}$$

increases linearly with distance traveled and the total density anomaly is conserved, making potential energy decrease linearly with distance traveled, the ratio of potential energy lost to kinetic energy gained by the mean motion of the blob is a constant. Further, the change of both potential energy and kinetic energy are individually constant with respect to distance traveled across the layer,

$$\frac{d(PE)}{dz} = \text{const.} \quad , \quad \frac{d(KE)}{dz} = \text{const.} \tag{2.105}$$

The ratio

$$\frac{d(KE)/dz}{d(PE)/dz} = R \tag{2.106}$$

is the fraction of potential energy that is converted into kinetic energy of the mean motion. An estimate of this conversion ratio must take into account more details of the physical situation. For the Hills spherical vortex model used by Turner, the fraction of the energy in the mean motion is

$$R = 5/14 \tag{2.107}$$

Since the structure of suddenly released plumes in the laboratory closely resembles Hills spherical vortex, this should be a reasonable estimate of the conversion ratio under conditions found in the ocean. The remaining 9/14 of the potential energy that is not accounted for in

the mean motion must go into turbulent kinetic energy within the layer and viscous dissipation.

2.2.3 Intermittent Convection

Because of the unstable buoyancy flux at both ends of a field of salt fingers, the situation there may be analogous to a layer of fluid heated from below. The relevant parameters to this flow are grouped to form a Rayleigh Number, Ra, and a Prandtl Number, σ, which have been defined above as

$$R_a = \frac{g\alpha \Delta T \ell^3}{\nu k_T} \quad , \quad \sigma = \nu / k_T \tag{2.108}$$

where ℓ is the thickness of the fluid layer and ΔT is the temperature difference across the layer. In this case, a measure of the flux is given by the Nusselt Number, Nu, which is the ratio of the actual heat flux to the heat flux by pure conduction across a layer with thickness ℓ and temperature difference ΔT.

$$Nu = \frac{F_T}{k_T \Delta T / \ell} \tag{2.109}$$

where F_T is the "kinematic" heat flux as before. The convective flux law is then

$$Nu = f_n (Ra, \sigma) \tag{2.110}$$

This problem has been analyzed by numerous investigators both theoretically and experimentally, but no satisfactory theory yet exists. A dimensional argument may be used to predict the form of (2.110) when the Prandlt Number and Rayleigh Number are both large. The heat flux should not depend on the Prandtl Number when that quantity is large and the separation of the plates is no longer relevant

when it is so large that the flux depends only on conditions near the boundaries. In that case, the form of the Nusselt Number is (Chandrasekhar, 1961)

$$Nu = c\, Ra^{1/3} \qquad (2.111)$$

which is independent of ℓ and σ.

For small Rayleigh Number, thin fluid layers or small temperature differences, the flow is stable and the conductive heat flux is steady, Nu = 1. As the Rayleigh Number is increased past about 1000 (the exact numerical value depends on the boundary conditions) the fluid becomes unstable and breaks down into regular cellular convection cells (Bernard convection). This instability is predicted theoretically and observed in the laboratory. Further increases in the Rayleigh Number lead to additional convection modes with strong dependence on Prandtl Number. Still further increases in Rayleigh Number result in time dependent flows and turbulence. Various investigators have derived different forms of (2.110), which apply to a variety of conditions and assumptions but most are very close to (2.111) with some variability in the exponent, experimentalists reporting slightly smaller values in the range $Ra < 10^8$ (Rossby, 1969; Somerscales and Gazda, 1969).

In the classical Rayleigh-Bernard problem, the temperature difference is specified and the fluxes are calculated. But the transition zone situation has different boundary conditions which imply that the Rayleigh Number should be reformulated. The flux of heat, salt and buoyancy through the transition zone is prescribed by the fluxes through the salt fingering interface. Substituting

$$\alpha \Delta T = \frac{\alpha F_T}{k_T/\ell} \tag{2.112}$$

in (2.108) gives the flux Rayleigh Number

$$Ra_f = \frac{\alpha F_T \ell^4}{k_T^2 \nu} \tag{2.113}$$

When the unstable buoyancy flux is due to salt, the flux Rayleigh Number becomes

$$Ra_f = \frac{\beta F_s \ell^4}{k_s^2 \nu} \tag{2.114}$$

Under conditions in the transition zones associated with salt fingering in the ocean, $\beta F_s \cong 10^{-5}$ (c.g.s.) (Turner, 1967); so that the flux Rayleigh Number will be very large for any reasonable layer depth l. With ℓ in cm,

$$Ra_f \cong 10^7 \ell^4 \tag{2.115}$$

Further, when the buoyancy flux is due to salt, the dynamical role of the Prandtl Number is replaced by the Schmidt Number, $S_c = \nu/k_s \cong 10^3$ so that the limiting form for large values of this parameter may be applicable.

Such high Rayleigh Numbers as are implied by (2.115) have never been achieved in the laboratory, where flux measurements can be made. Visual observations of salt finger convection suggest that the flow regime in the transition zone is unsteady with large scale blobs of fluid rising or sinking according to their density anomaly, and this type of flow has also been observed in other cases of buoyant convection at high Rayleigh Number (Sparrow et al., 1970).

Howard (1964) has given a mechanistic model of the boundary layer at large Ra, which is repeated here. The heat flux is maintained through a diffusive sublayer by conduction, while buoyant fluid accumulates. After a period of time, t_*, the accumulated fluid breaks off from the boundary and rises or sinks according to its density anomaly in a relatively large blob. Fluid from the adjacent layer then rushes in to replace the blob and the cycle repeats itself. The important physical characteristics that are reproduced by this model are the unsteady flow and the large scale blobs. Because of the flux boundary condition in the transition zone problem the details of the conductive part of Howards model are probably inappropriate to that situation.

The problem implied by Howards argument is unsteady and necessarily non-linear. Foster (1971) has considered this problem with a numerical model based on the full two-dimensional Boussinesq equations of motion. The motion is divided into mean and fluctuating components using a Reynolds decomposition, and the system is expanded in terms of a two dimensional Fourier series with time dependent coefficients. The number of Fourier components necessary for such a representation was found to increase with Rayleigh Number being approximately 20 when $Ra_f = 10^7$. Computer capacity limited the solutions to $Ra_f < 10^8$. A further idealization that is imposed by machine size is that only one mode or wavenumber is retained in the horizontal direction. This mode was chosen as the one which gave the largest r.m.s. vertical velocity, near the onset of convection, but in practice it was found to be close to the fastest growing disturbance based on linear theory (a result

predicted by Malkus, 1954). The numerical solutions are steady for $Ra_f < 10^7$, and intermittent for larger values. The average frequency of blob release is found to be independent of layer depth as is the horizontal length scale of the convection. Both of these results are consistent with concept of a boundary layer flow that is independent of the interior flow, i.e., the convecting layer thickness. The model predicts a period, τ_f^*, and a wave number, $2\pi/d$, for heat as

$$\tau_f^* = 14. \left(\frac{g\alpha F_T}{\nu}\right)^{-1/2} \tag{2.116a}$$

$$2\pi/d = 0.13 \left(\frac{g\alpha F_T}{K_T^2 \nu}\right)^{1/4} \tag{2.116b}$$

while the corresponding formulae for salt convection are

$$\tau_f^* = 14. \left(\frac{g\beta F_S}{\nu}\right)^{-1/2} \tag{2.117a}$$

$$2\pi/d = 0.13 \left(\frac{g\beta F_S}{K_S^2 \nu}\right)^{1/4} \tag{2.117b}$$

Under conditions appropriate to salt finger convection in the ocean, the period of intermittency is a few minutes, while the cell spacing for heat and salt are respectively about 10 cm and a few millimeters. These plumes which are found outside the salt finger region may be visible to a shadowgraph system and explain certain observations that will be described later: The length scale associated with the destabilizing salt flux (a few millimeters) does not seem to agree with reported visual laboratory observations where the implicit length scale seems to be much larger.

It may be that Foster's model is describing a scale of convection that is different than that described by salt finger observers. In any

case the flux Rayleigh Number in the ocean must be several orders of magnitude greater than those that have been attained in the laboratory or numerically and the model may not be appropriate in this case. Further, though the numerical results show a horizontal cell spacing that is independent of the layer depth, the range explored was very narrow, $\frac{7}{\ell} \geq \frac{2\pi}{d} \geq \frac{11}{\ell}$, and hardly satisfies asymptotics conditions $d \ll \ell$. In spite of these shortcomings, there may be certain applications for this model in describing ocean data.

2.2.4 Analogy with Planetary Boundary Layer

The transition zone in salt finger convection is similar to the problem of "thermals" in the planetary boundary layer. Unstable conditions arise in the latter case when the imput of heat is concentrated near the ground and a layer of warm buoyant fluid is created there. When winds are weak, the light air accumulates near the ground into a large mass and rises as a single blob or thermal. Efforts to describe this phenomonon have concentrated on the dynamics after it has been formed. Prediction of length scales or other characteristics under actual conditions have generally failed, though some models have been formulated for specific instabilities in the quasi-laminar regime for laboratory conditions. In the geophysical case where the environment is turbulent and the Rayleigh numbers can be extremely large, there is no satisfactory theory. Also extremely large Rayleigh Numbers cannot be simulated in the laboratory, and there are few field measurements.

The analogy between thermals in the planetary boundary layer and the transition layer in the salt finger-convecting layer system is

not perfect. The Prandtl Number for air is about 1/10 that of water but this may not be important under fully turbulent conditions except very near the interface or wall. The boundary conditions for the velocity field are rigid, no slip boundaries for the planetary boundary layer, while they are both slippery and flexible for the buoyant transition layer. In both cases the approximation of a constant flux of buoyancy appears to be the correct condition on the buoyancy field rather than a constant difference.

There are a few results from the meteorological literature that may be relevant here. Businger, Wyngaard, Izumi and Bradley (1971) have made turbulence measurements including both surface stresses and heat fluxes in the planetary boundary layer. Since these data include measurements under unstable conditions, they may be relevant to the buoyant layer in the salt finger convection problem. The major difficulty in interpreting their results is the non-dimensionalization of the vertical coordinate. The Monin-Obukov length is defined

$$L_B \equiv \frac{\rho_0 u_*^3}{k g \overline{\rho' w'}} \qquad (2.118)$$

where k = 0.4 is Karman's constant, $u_* = \sqrt{\tau_0/\rho_0}$ is the friction velocity calculated from the shear stress at the ground, τ_0, and $\overline{\rho' w'}$ is the vertical turbulent transport of density fluctuations. The meaning of the friction velocity on the assumed stress-free boundaries in the transition zone is somewhat vague, but there may be another such as the velocity of the large eddies in the convecting layers that may be substituted. In any case the equivalent velocity scale is unknown.

When the results of Businger et al. are interpreted in terms of mean potential temperature gradient, the dimensional form is

$$\frac{d\bar{\theta}}{dz} = (\overline{w'\theta'})^{1/2}\left(g/\bar{\theta}\right)^{-1/2} u_*^{1/2}\, z^{-3/2} \qquad (2.119)$$

The dependence on the friction velocity makes this result difficult to apply in the ocean without direct shear measurements. By dimensional analysis a similar form for the temperature gradient which is independent of the shear, viz.,

$$\frac{d\bar{\theta}}{dz} = (\overline{w'\theta'})^{1/3}\left(g/\bar{\theta}\right)^{-1/3} z^{-4/3} \qquad (2.120)$$

Although this form is predicted in the free convection mode, the data seems to favor (2.119) under unstable conditions.

2.3 Shear Instability

An alternative mechanism for mixing in the interior of a stratified fluid is instability which transforms the vertical shear of horizontal velocity to turbulence. Mixing by shear instability is probably very important in the atmosphere and may also be found in the ocean. The fundamental parameter for mixing by shear instability is the gradient Richardson Number

$$Ri = -\frac{g}{\rho}\,\frac{\partial\rho/\partial z}{(\partial u/\partial z)^2} \qquad (2.121)$$

When this parameter becomes less than some value that is about one (the exact value depends on the assumed initial distribution of velocity and density before instability), an overturning event is possible which results in a breakdown to turbulence. The shear is supplied by a superposition of geostrophicly balanced shear and internal gravity wave

motions. In the case of a wave that is long compared to the length scale of the microstructure on which it acts, the shear may persist for long enough that Kelvin-Helmholtz instability can develop to finite amplitude and breakdown.

By considering such low mode internal waves, Phillips (1966) has shown that the location that has the lowest Richardson Number and is the most likely to be unstable is that which has the maximum density gradient. This suggests that turbulence should be found on or near interfaces which have large density difference, or, on a larger vertical scale, in portions of the water column with anomalously high stability. A more comprehensive description of mixing by breaking internal waves is given by Woods and Wiley (1972).

Woods' theory is based on observations by divers and profiles with a thermistor taken near Malta within the seasonal thermocline. In the experiments, dye was spread on a horizontal sheet and subsequently observed and photographed by the divers. At times they saw sheets of dye roll up and break in a way compatible with the theory of Kelvin-Helmholtz instability. They found that these events were apparently initiated by packets of internal waves with characteristic parameters: wave length λ = 5 m, period T = few minutes, and phase speeds C = a few centimeters per second. The frequency of these events is such that 3-10% of the flow is turbulent at any time, while the time between events at any point is 1-6 hr. After an interface breaks down, the equilibrium state of the flow is two interfaces with a mixed layer separating them. These interfaces are in turn sheared leading to a multiplication of interfaces and mixed layers.

It is not clear that this particular recipe and scaling applies directly to the deep ocean, but there are several important points that can certainly be carried over. The first is that a strong density interface is the preferred location for breakdown. Secondly, the mechanism leads to a multiplication of the number of interfaces and layers, continuing, presumably, until there is some equilibrium spacing of interfaces (thickness of layers) which depends on the stratification and the characteristics of the ambient internal wave field and mean shear. Thus in a region where the mean shear and the statistics of internal wave field is homogeneous, the equilibrium condition is a distribution where the density difference across an interface is a constant.

2.4 Energetics of Mixed Layers

When the vertical distribution of density or mass changes, it is generally accompanied by a change in potential energy. Or, put another way, when the distribution of mass changes, with the total mass remaining constant, the center of the mass will move vertically except under very special circumstances. In this section the potential energy change associated with changes in mass distribution is calculated for two special cases that apply to layered structure in the ocean.

The simplest case conceptually and analytically is the formation of a uniform layer bounded by very sharp interfaces from an initial state where the gradient is constant. The physical situation is shown schematically in Figure 2.5, where a layer with thickness H and density $\bar{\rho}$ is formed from initially uniform density gradient $\bar{\rho}_z$. Taking the arbitrary reference level for potential energy at the base of the

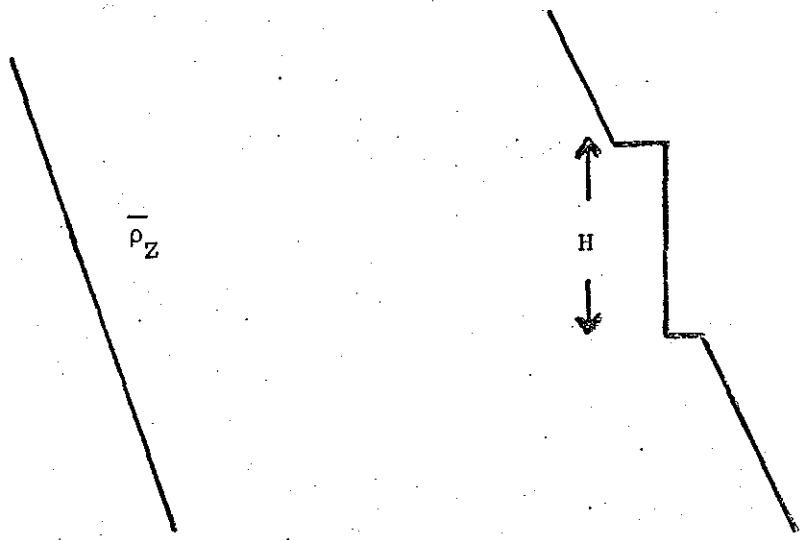

FIGURE 2.5 Formation of a homogeneous layer from a constant density gradient.

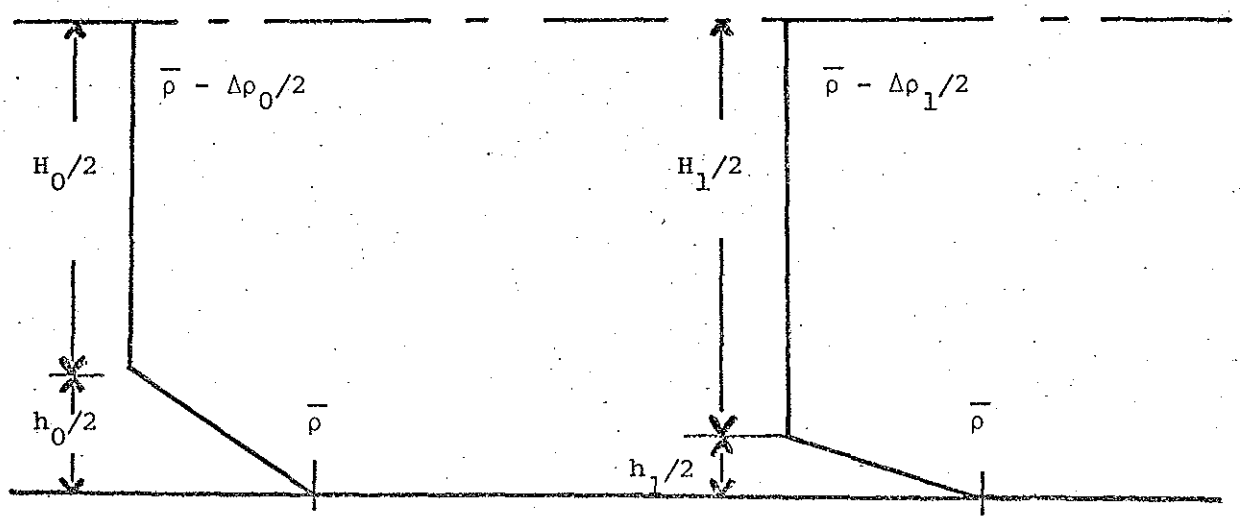

FIGURE 2.6 Thickening of a homogeneous layer. Half an interface and half a layer are shown. The density at the center of the interface is constant, as is the sum of the layer and interface thicknesses.

uniform layer and using z as the vertical coordinate, positive upward, the difference in potential energy per unit horizontal area between the two states is

$$\Delta pe = (pe)_1 - (pe)_0 \tag{2.122a}$$

$$= g/2\ \bar{\rho}\ H^2 - g \int_0^H \left[\left(\bar{\rho} + \bar{\rho}_z\, H/2\right) - \bar{\rho}_z z\right] z\, dz \tag{2.122b}$$

$$= g\ \bar{\rho}_z\ H^3/12 \tag{2.122c}$$

A more general model considers the case where there is already a layer and interface configuration established. When the interface thickness changes, the layer thickness also changes to conserve volume. Mass is also conserved, but potential energy may change. The situation is illustrated in Figure 2.6. The origin is taken at the center of an interface where the density is assumed to remain fixed at $\bar{\rho}$. The system analyzed consists of a half interface with thickness h/2 where the density gradient is constant and the overlying half layer with thickness H/2 where the density is constant. The situation considered is a thinning of the interface with equal thickening of the uniform layer. The subscript zero refers to the initial state and the subscript one is for the final state. Since volume is conserved,

$$\frac{H_0}{2} + \frac{h_0}{2} = \frac{H_1}{2} + \frac{h_1}{2} = \text{const.} \tag{2.123}$$

Similarly, the total mass in the system is

$$\left(\bar{\rho} - \frac{\Delta\rho_0}{2}\right)\frac{H_0+h_0}{2} + \frac{1}{2}\,\frac{h_0}{2}\,\frac{\Delta\rho_0}{2} = \left(\bar{\rho} - \frac{\Delta\rho_1}{2}\right)\frac{H_1+h_1}{2} + \frac{1}{2}\,\frac{h_1}{2}\,\frac{\Delta\rho_1}{2} \tag{2.124}$$

where $\Delta\rho/2$ is the difference in density between the origin (the center of the interface) and the uniform layer. This expression can be simplified to give a relation between the two density differences

$$\Delta\rho_1 = \frac{2H_0 + h_0}{2H_1 + h_1}\,\Delta\rho_0 \tag{2.125}$$

Define the ratio of interface thickness to layer thickness, r, and the dimensionless change in the interface thickness, δ, as

$$r = h/(H+h) \tag{2.126a}$$

and

$$\delta = \frac{h_1 - h_0}{h+H} = \frac{H_0 - H_1}{h+H} \tag{2.126b}$$

The mass conservation (2.125) can then be rewritten using (2.123) as

$$\Delta\rho_1 = \frac{2 - r_0}{2 - r_0 - \delta}\,\Delta\rho_0 \tag{2.127}$$

To evaluate the change in potential energy, the change in height of the center of mass must be calculated. The integrals are simplified by an artificial separation into a "layer" with density $\bar{\rho} - \Delta\rho/2$ and thickness (H + h)/2 and an "interface anomaly" with density linearly decreasing from $\bar{\rho}$ to $\bar{\rho} - \Delta\rho/2$ over the thickness h/2. The center of mass for the "layer" does not move, but its share of the total mass changes by an amount (2.128)

$$\Delta M_\ell = \left(\frac{H_1+h_1}{2}\right)\left(\bar{\rho} - \frac{\Delta\rho_1}{2}\right) - \left(\frac{H_0+h_0}{2}\right)\left(\bar{\rho} - \frac{\Delta\rho_0}{2}\right)$$

$$= \left(\frac{H_0+h_0}{4}\right)\left(\Delta\rho_0 - \Delta\rho_1\right)$$

$$= \frac{1}{4}\left(H_0+h_0\right)\left(1 - \frac{2-r_0}{2-r_0-\delta}\right)\Delta\rho_0$$

Since the total mass is conserved, the change in mass for the "interface anomaly" is equal to the negative of the change for the layer

$$\Delta M_i = - \Delta M_l \tag{2.129}$$

The potential energy in the "interface anomaly" is

$$pe = g \int_0^{h/2} \rho z \, dz \tag{2.130a}$$

$$= g \int_0^{h/2} \frac{\Delta\rho}{2} \left(1 - \frac{z}{h/2}\right) z \, dz \tag{2.130b}$$

$$= g \, \Delta\rho \, h^2 / 48 \tag{2.130c}$$

and the change is

$$(\Delta pe)_i = \frac{g}{48} \left(\Delta\rho_1 h_1^2 - \Delta\rho_0 h_0^2 \right) \tag{2.131a}$$

$$= \frac{g \Delta\rho_0}{48} \left(\frac{2 - r_0}{2 - r_0 - \delta} h_1^2 - h_0^2 \right) \tag{2.131b}$$

In the case of small change in interface thickness,

$$\frac{2 - r_0}{2 - r_0 - \delta} = \frac{1}{1 - \delta/2 - r_0} \cong 1 + \frac{\delta}{2 - r_0} \tag{2.132}$$

if $|\delta| << 2 - r_0$. Then, after some manipulation, (2.131) can be written to the approximation (2.132) as

$$(\Delta pe)_i = \frac{g}{48} \Delta\rho_0 (H+h)^2 \delta \left[\frac{-r_0^2 + 4r_0 + r_0\delta + 2\delta}{2 - r_0} \right] \tag{2.133}$$

Since the center of mass of the "layer" does not move

$$(\Delta pe)_\ell = g\,\Delta M_\ell\, z_c \tag{2.134}$$

where z_c is the height of the center of mass

$$z_c = \tfrac{1}{4}(H+h) \tag{2.135}$$

Combining (2.128), and (2.133) - (2.135) and using the approximation (2.132) the net change in potential energy is

$$\Delta pe = -g\,\Delta\rho_0 (H+h)^2 \left[\tfrac{1}{16}(1+r_0)^2 \frac{\delta}{2-r_0} - \tfrac{1}{48}\delta\left(\frac{-r_0^2+4r_0+r_0\delta+2\delta}{2-r_0}\right)\right]$$

and this can be simplified to

$$\Delta pe = -\frac{g\,\Delta\rho_0 (H+h)^2 \delta}{48}\left[\frac{(r_0-1)(r_0-3)-\delta(r_0+2)}{r_0-2}\right] \tag{2.136}$$

In the case of a thin interface relative to the layer, i.e., $r_0 \to 0$,

$$\Delta pe = g\,\Delta\rho_0 (H+h)^2 \delta / 32 \tag{2.137}$$

The overall stratification of the system is measured by the Brunt-Väisälä frequency, N_0 , which can be written in the present notation as

$$N_0^2 = \frac{g\,\Delta\rho_0}{\bar{\rho}(H+h)} \tag{2.138}$$

Substituting (2.138) into (2.136) gives

$$\Delta pe = -\frac{\bar{\rho} N_0^2 (H+h)^3 \delta}{48}\left[\frac{(r_0-1)(r_0-3)-\delta(r_0-2)}{r_0-2}\right] \tag{2.139}$$

Assuming again that δ is small, only the linear term in δ is retained and the potential energy change can be rewritten

$$\Delta pe = -\frac{\bar{\rho} N_0^2 (H+h)^3 \delta}{48}\left[\frac{(r_0-1)(r_0-3)}{r_0-2}\right] \quad (2.140)$$

The function in the brackets depends only on r_0. Finally, to obtain the potential energy change per unit volume (2.140) must be divided by $\bar{\rho}(H+h)$, giving

$$(\Delta pe)^* = -\frac{N_0^2 (H+h)^2 \delta}{48}\left[\frac{(r_0-1)(r_0-3)}{r_0-2}\right] \quad (2.141)$$

This function is plotted in Figure 2.7. It is nearly linear in r_0, decreasing from the thin interface asymptote, (2.137), to zero as $r_0 \to 1$. This latter limit corresponds to an infinitessimal mixed layer in a linear gradient. This shows that as a mixed layer thickens, it takes an increasingly large amount of energy to thicken it further.

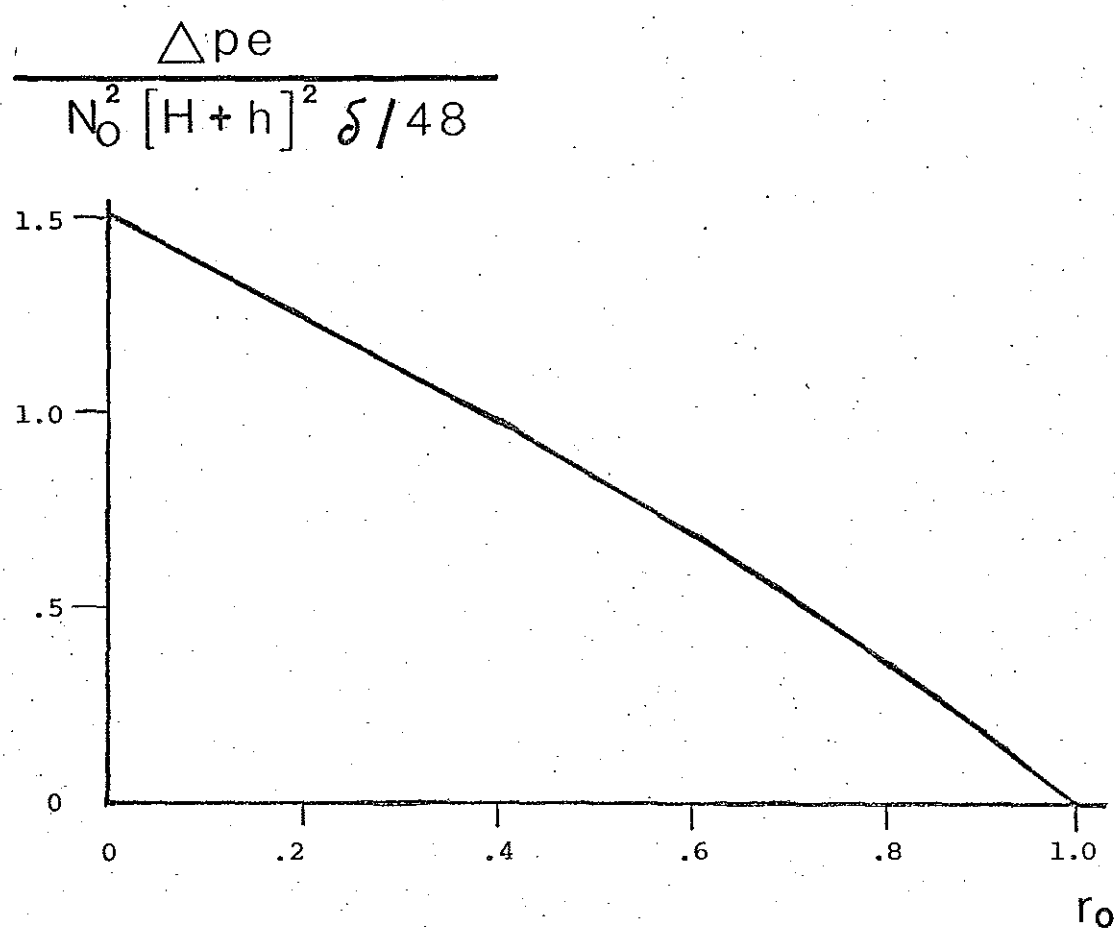

FIGURE 2.7 Dimensionless potential energy change for thickening an existing homogeneous layer in a homogeneous layer and constant density gradient system. The abscissa is the ratio of the interface thickness to the sum of the layer and the interface thicknesses. As the interface becomes relatively thin, an increasingly large amount of energy is required to thin it further. The rate of increase is very nearly linear.

3. ANALYSIS OF MEASUREMENTS

This is the second major section, and it is a comparison of the models developed in the previous section with measurements in the deep ocean. There are two sets of measurements taken in hydrographically similar areas. In both cases there is a flow of water from one basin to another where the two basins have different T-S characteristics. The intruding water is warmer and saltier than the majority of water in the receiving basin so that one characteristic of the system is a subsurface salinity maximum. Most of the emphasis in this section is on understanding the finestructure and turbulence that is found at and below this salinity maximum. The structure appears to be strong influenced by double diffusive convection.

The measurements consist of vertical profiles taken with the freely sinking probe SCIMP (Self-Contained Imaging Micro-Profiler). There are two sensor packages on the probe. One is a CTD (Conductivity-Temperature-Depth), and besides the directly measured variables it can be used to calculate the salinity and density of the sea water. The other is a special purpose instrument called the OSFD (Optical Salt Finger Detector). It records shadowgraphs taken through the sea water on motion picture film. Appendix A describes the instrumentation in greater detail.

3.1 Mediterranean Outflow

The Mediterranean Sea exchanges water with the North Atlantic through the Strait of Gibraltar. At the depth of the sill, the Mediterranean water is saltier and denser than North Atlantic water so it sinks after flowing out through the strait. As it sinks, it entrains

North Atlantic water that is less salty and less dense until it reaches a level and a dilution such that its density is equal to the environmental density and it spreads horizontally at that level. This water mass of Mediterranean influenced water is known as the Mediterranean Outflow. It is characterized by a maximum in the vertical profile of salinity at depth that is usually between 1000 m and 1200 m. The salinity at this maximum may be well over 36.0 °/oo near the Strait of Gibraltar, but it decreases to the west to near 35.0 °/oo after which it is no longer recognizable as a distinct deep salinity maximum. The density expressed in terms of σ_t is in the range 27.6 - 27.8.

The spreading and dispersion of this high salinity water can be used to test some ideas about ocean mixing and the dilution of any intrusion in the ocean. The central questions are whether there is any vertical mixing and if so by what mechanism. Recent calculations by Needler and Heath (1975) suggest that there is a negligible amount of diffusion normal to surfaces of constant potential density, while earlier calculations by Turner (1967) predict rapid vertical transport by salt finger convection.

Within a few hundred miles of the Strait, the influence of the Mediterranean water is particularly strong, and numerous STD casts have been made in the region. There are two unexpected features that are often seen on STD casts, stepped structure and multiple temperature inversions. These two types of finestructure are often found together and may be related.

In 1966 Tait and Howe discovered regularly spaced steps in temperature and salinity below the salinity maximum, where both properties

were nearly uniform for 15-30 meters but are bounded by interfaces where both properties decrease abruptly with depth. Similar steps have been repeatedly observed in the same region making them seem a characteristic feature of the area. The similarity of these steps to features of salt finger convection in the laboratory has prompted some to suggest that this is the cause of the stepped structure.

The second feature of the Mediterranean Outflow that has been repeatedly discussed are the numerous temperature inversions that are often found near the salinity maximum. They are suggestive of interleaving of different water types and may also give valuable information on intrusions and their dispersion in the ocean environment. In particular, is double diffusive convection active both above and below these temperature inversions?

It is natural to question why an additional experiment is necessary in an area that has been given such thorough coverage. The reason is that previous studies were conducted with a standard STD or one altered for higher resolution lowered on a cable from a ship. In the present discussion the measurements were taken with a specially designed probe SCIMP. There have been objections (Pingree, 1971) to measurements of finestructure with an instrument that is lowered on a cable. Since SCIMP sinks freely without any connection to the ship, its measurements are not biased by ship motions. A second problem is that both stepped structure and inversions are not fully resolved by the STD. The CTD with its higher resolution on all channels can see more details of the structure. Finally the OSFD photographs salt fingers and other events which have strong fluctuations in index of refraction on the scale of a centimeter or less.

During July 1973 SCIMP was deployed 6 times from the R/V ATLANTIS II in an area 200 miles southwest of the Strait of Gibraltar. The exact location was chosen primarily because of repeated reports of regularly spaced steps in temperature and salinity below the deep salinity maximum (Tait and Howe, 1968; Howe and Tait, 1970). Since it seemed likely that salt finger convection was responsible for the steps, this appeared to be the ideal place to deploy the OSFD. Also onboard were Bruce Magnel of MIT with a towed body designed to record the periodic horizontal fluctuations in electrical conductivity characteristic of salt finger convection and Neil Brown with a cable lowered CTD with a fast response temperature capability.

On each of the first 5 dives, SCIMP sank rapidly ($\sim$ 25 cm/sec) to approximately 1000 meters, where it dropped a weight to slow its descent rate and turned on the shadowgraph system. It then sank at varying rates to a maximum depth of approximately 2000 m where it dropped a second weight to return to the surface. On the sixth and last dive it sank rapidly all the way to 1800 meters because shiptime was limited.

On these 6 dives the OSFD recorded numerous instances of vertically banded structure and other optical signals that have more random orientation. The CTD on SCIMP also recorded several sequences of regular spaced steps in temperature and salinity, and often the vertical bands were simultaneous with the large gradients separating the steps. Careful evaluation of the films and profiles is necessary to make this relationship more precise.

3.1.1 Stepped Structure and Shadowgraphs

Profiles of temperature, salinity and density in the ocean are never smooth. There is always irregularity on a broad range of vertical length scales from the smallest scale, where diffusion acts to smooth fluctuations, to the largest scale, that of the thermocline itself. There are certain types of irregularities that have come to be called steps because of the similarity of the temperature profile to a staircase. The characteristic feature of these steps is a sequence of uniform layers that are nearly the same thickness and are separated by relatively thin interfaces where temperature and salinity differences are maintained. These steps are such an unexpected feature of ocean stratification that they have attracted much attention and special theories such as double-diffusive convection have been suggested as possible causes for these structures.

Some of the first published reports on stepped structure were based on measurements in the Mediterranean Outflow region (Tait and Howe, 1968; Howe and Tait, 1970). These steps averaged about 20 m thick and had temperature and salinity differences between them of 0.2 C and 0.03 $^{o}/oo$, respectively. There are usually between 5 and 20 layers, but sometimes there are no layers at all in a profile. Repeated observations show that stepped structure is a characteristic of the Mediterranean Outflow, but it is intermittant because it is not always found. The size of the layers has also been shown to vary. Using a high resolution CTD, Siedler and Zenk (1973) found layers in the same region whose parameters were all reduced by a factor of 10. An important correlary to these observations is that the layers

described by Siedler and Zenk would probably have been invisible to Tait and Howe using a lower resolution, conventional STD.

The layers measured on the cruise ATLANTIS II 76, are between two sets of observations described above in size and they occur at the same geographical location and depth. Figure 3.1 shows the profiles of temperature, salinity and potential density for Dive 2 taken 18 July 1973. This is the best example of stepped structure observed by SCIMP during the experiment. The steps occur between 1350 and 1700 decibars and would be barely visible on this scale but for the instrumental spikes in salinity and density. Figure 3.2 shows an enlargement of this section of the profile. The black dots show the locations where there are distinct, regularly spaced, vertical bands in the shadowgraphs. It can be seen that the banded structure occurs on the interfaces, but not all interfaces have banded structure. Before attempting any correlations some of the implications and limitations of the shadowgraphs must be appreciated.

The OSFD can only photograph salt fingers when:

(1) They are the correct size, 2 mm < width < 20 mm, approximately.

(2) The rising and sinking salt fingers have a refractive index distribution that has a large second derivative with respect to the horizontal direction.

(3) The array of square salt finger cells is at an angle (with respect to a rotation about a vertical axis) where it is visible.

With these seemingly severe provisos, it is very likely that all salt fingers in the ocean will not be seen by the OSFD. Naturally, there will be variations in the quality of an image.

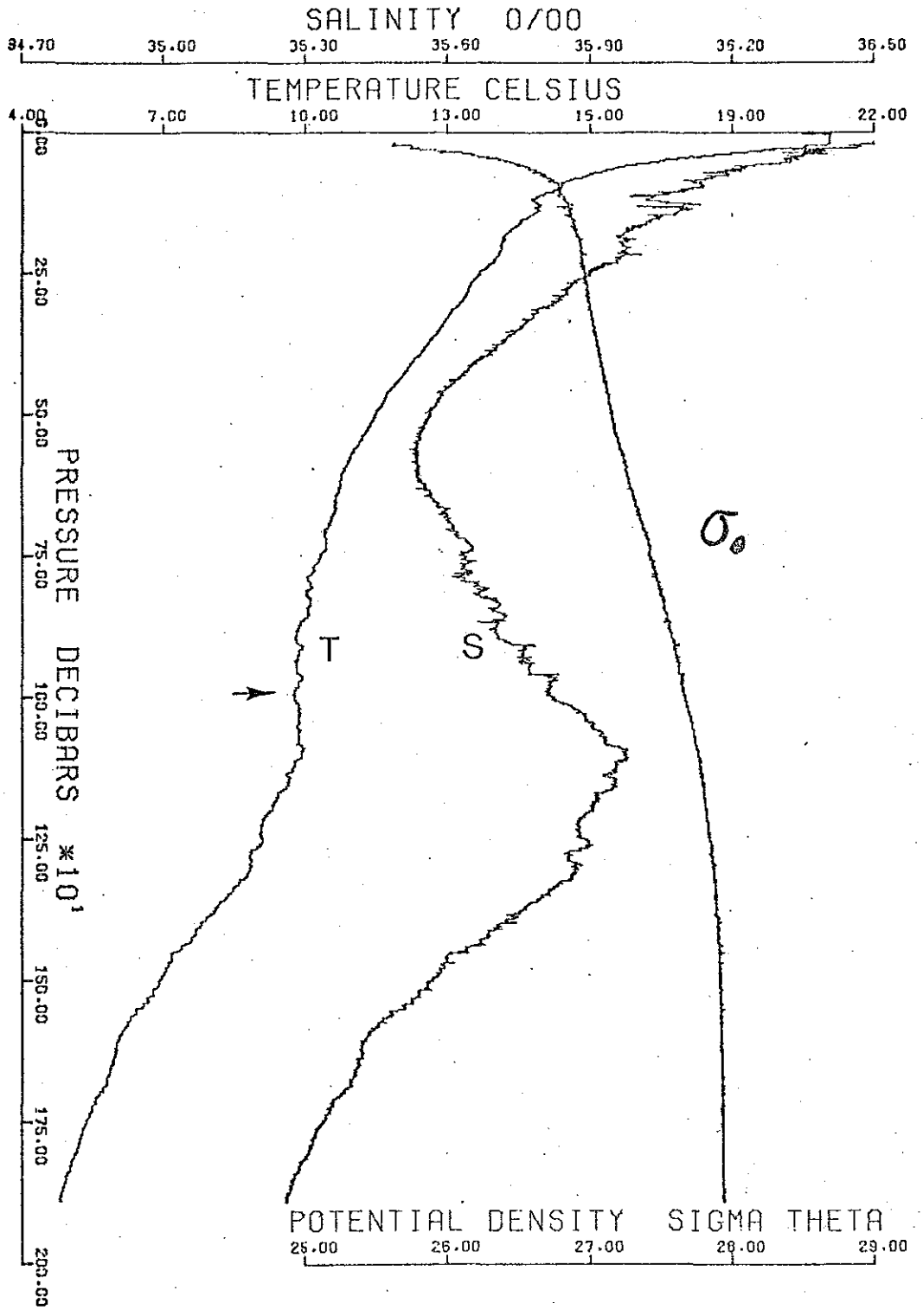

FIGURE 3.1 Profiles of temperature, salinity and potential density from SCIMP 2. The measurements were made from the R/V ATLANTIS II, 0017Z, 18 July 1973 at 34-16.1°N, 10-49.8°W. The arrow indicates where the OSFD was turned on.

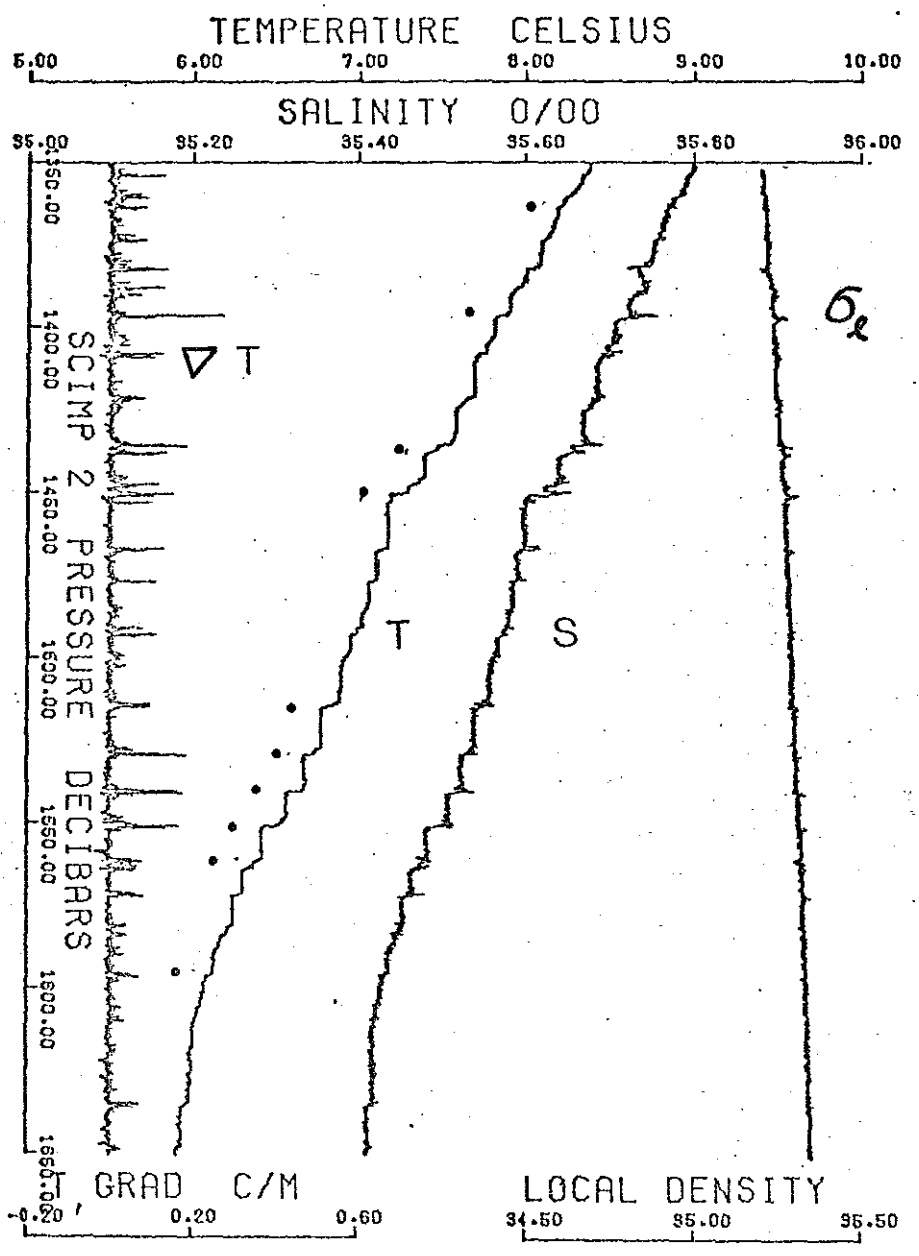

FIGURE 3.2 Expanded profiles of temperature, salinity, local potential density and temperature gradient for SCIMP 2 (Fig. 3.1). The stepped structure is included and the dots beside the temperature profile mark interfaces with high contrast banded structure in the shadowgraphs.

The images are recorded on 16 mm motion picture film. When they are viewed as a movie rather than examined as individual frames, the images are more apparent. In many cases, structures which are clearly visible in the movie cannot be identified in a still, but their location can be estimated by quickly stopping the projector and counting back a known number of frames. In this way, the location of a particular frame can certainly be located ±2 frames. Accordingly the following convention has been adopted for classifying images where there is vertically banded structure:

(1) no vertical structure.

(2) faint - can be seen in the movie, but no trace can be found on stills.

(3) weak - some contrast can be seen on a still but banded structure is not evident there.

(4) moderate - vertical banded structure is evident in still images.

(5) strong - high contrast bands in stills.

Even with this classification system, there is a fair amount of subjectivity in identifying images, particularly the weaker ones.

Just as every set of salt fingers may not be visible to the OSFD system for reasons described above, every image with vertical banded structure may not be salt fingers. It is certainly possible that a random variation in index of refraction as might be expected in turbulence would have shadowgraphs with lines in a vertical or near vertical orientation some of the time.

3.1.2 Interfaces with Salt Fingers

Theoretical models described above and extrapolations from laboratory experiments have allowed predictions of the relations among the properties of salt fingering interfaces under conditions in the ocean. As a first step toward describing salt fingers in the ocean, the interfaces where there are salt fingers on the films are summarized and compared to these models. First the interfaces where there are "strong" or "moderate" bands are examined in cases where the mean salinity is generally decreasing with depth. There are 18 interfaces in this category and some of their properties are summarized in Table 3.1.

Each interface is identified by a dive number and the approximate pressure at the observation. The values in the table have been determined by visual inspection of the profiles. Practically, the differences were determined between two layers, i.e., between two isothermal (for about 0.5 m) levels so that salinity and density could be reliably calculated. The apparent slow response of the conductivity sensor makes salinity questionable when the temperature gradient is large. The maximum temperature gradient ∇T that occurs on an interface is calculated as a finite difference over approximately 10 cm. This length was chosen to quiet the quantization noise from the pressure channel (0.05 db) while retaining as much small scale information as possible. The interface thickness given in the table is compatible with the difference measurements for salinity and density. The layer thickness is also included in instances where there was a clearly defined isothermal layer.

TABLE 3.1

Interfaces with Banded Shadowgraphs

Dive-pressure (decibars)	Differences across interface ΔT (°C)	ΔS (ppm)	$\Delta\rho$ (ppm)	$\frac{\alpha\Delta T}{\beta\Delta S}$	Max. temp. grad., ∇T (°C/m)	Interface thickness (m)	Layer above (m)	Thickness below
1-1264	.232	40	13	1.4	.6	0.4	10.6	5.6
1-1337	.191	34	13	1.5	.162	1.3	--	--
1-1372	.056	8	4	1.6	.273	0.4	5.5	18.4
2-1435	.180	30	11	1.5	.184	4.9	6	8
2-1450	.224	42	8	1.2	.156	8.8	8	14
2-1514	.112	19	8	1.5	.100	2.3	12	11
2-1540	.118	19	9	1.6	.163	2.3	8	7
2-1550	.161	30	6	1.3	.153	4.3	7	9
2-1563	.121	21	6	1.4	.083	2.8	9	6.5
2-1598	.044	5	5	2.3	.072	1.0	6	--
3-1431	.092	16	4	1.3	.100	4.5	--	5
3-1440	.083	15	4	1.3	.197	2.8	5	6
3-1477	.046	7	3	1.6	.452	0.6	--	--
4-1373	.078	9	9	2.3	.142	1.3	8.4	2.2
4-1384	.058	8	4	1.6	.114	2.0	3.2	4.4
4-1397	.094	14	6	1.6	.050	5.0	3	5
4-1640	.025	5	2	1.5	.036	1.0	4	7
5-1580	.027	4	2	1.6	.052	0.7	3	10.5
Mean	.106	18	6.5	1.6	.172	2.6	7.3	
Standard Deviation	.064	12	3.5	0.3	.144	2.2	3.6	
Normalized Standard Deviation	.60	.67	.54	.19	.84	.85	.49	

The parameters in Table 3.1 are characterized by a high degree of variability with the standard deviation of the samples typically (0.5 - 0.9) x (average). Such variability is unexpected in light of the high degree of regularity found in some of the stepped sequences, but not all of these regular steps have stronger salt finger images on the films. In addition a large fraction of the samples came from isolated interfaces rather than from a layered sequence where conditions may be closer to equilibrium. The Turner Number, $Tu = \frac{\alpha \Delta T}{\beta \Delta S}$, is the ratio of the increase in density across an interface due to temperature to the decrease due to the salinity difference. $Tu < 1$ is gravitationally unstable.

The analyses in Section 2 derived relations among some of these quantities and it is instructive to test some of these. Using two independent criteria, relations for the interface thickness have been derived in (2.66) and(2.73), which can both be written $$h = B \frac{\alpha \Delta T}{\beta \Delta S} (\Delta S)^{-1/3} \qquad (3.1)$$ where B is in both cases some combination of constant factors. Using the data from Table 3.1, the quantity $\frac{\alpha \Delta T}{\beta \Delta S} (\Delta S)^{-1/3}$ is plotted versus the interface thickness, h, in Figure 3.3. The data do not support the relation (3.1). It appears that the interface thickness is independent of the quantity $\frac{\alpha \Delta T}{\beta \Delta S} (\Delta S)^{-1/3}$.

Since the expression (3.1) has failed to describe the data, the assumptions that lead to it must be examined as well as the measurements summarized in Table A. The equilibrium model in Section 2.1.2 is applicable to infinitely long salt fingers that are truncated either by an unspecified convective mechanism (2.66) or by the "collective instability" mechanism due to a slowly varying wave field (2.73). In either case, the interface thickness is proportional to the "age" of the

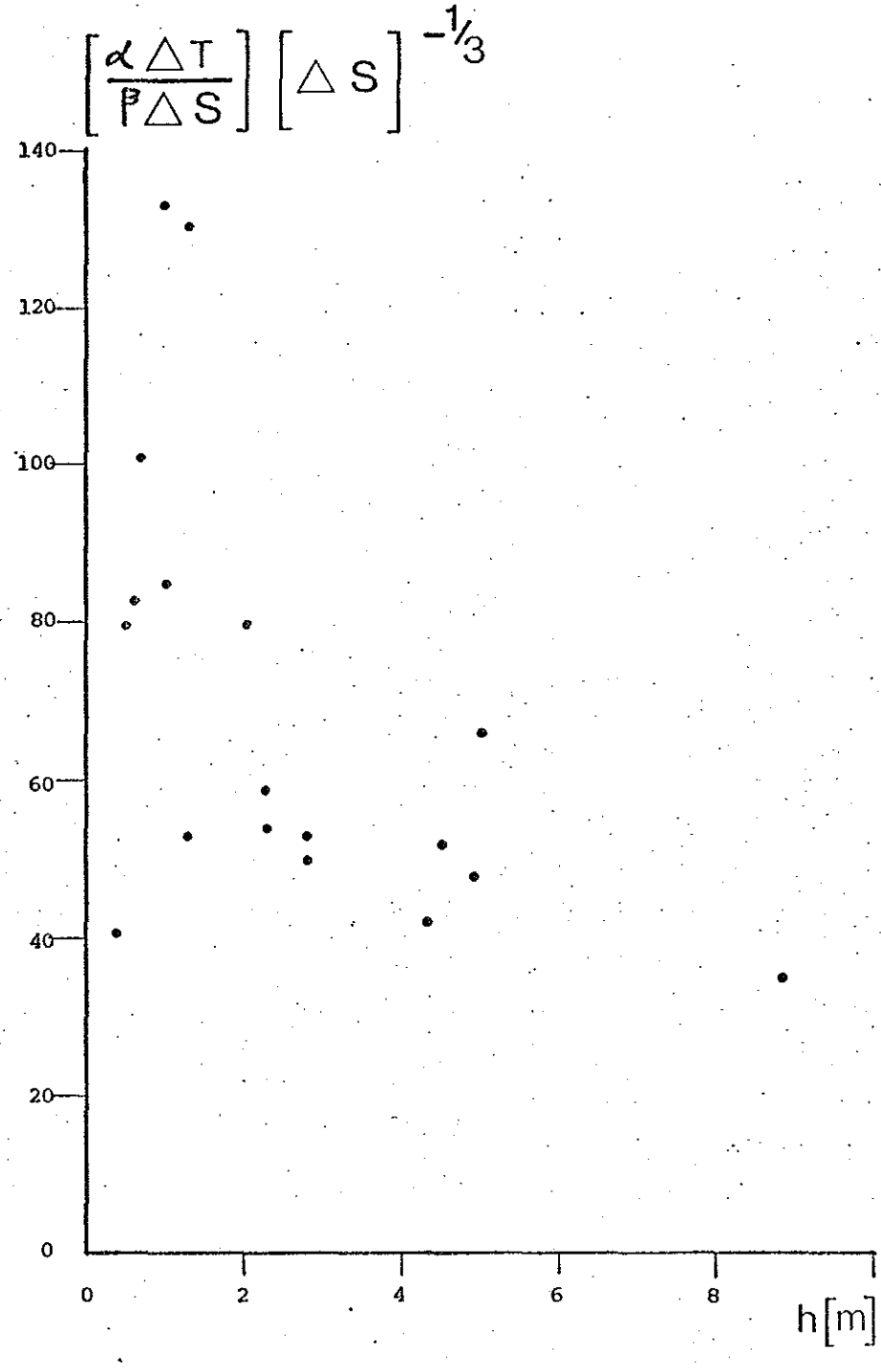

FIGURE 3.3 Comparison of calculated interface thickness to measured distance between mixed layers. The ordinate is proportional to the length of salt fingers calculated from the conditions at the interface. Each point represents an interface where there is high contrast banded structure in the shadowgraphs. The measured distance is not well represented by the calculation.

interface or the time since formation. According to Linden's (1973) observations in the laboratory, the interface grows at a constant rate which is much less than the vertical velocity in the fingers. It follows then that the age of the interface as well as the thickness is proportional to $\frac{\alpha\Delta T}{\beta\Delta S}(\beta\Delta S)^{-1/3}$. Although well defined initial conditions may be set up in the laboratory, their meaning is vague in the context of oceanic structures. What is observed is in an indefinite state of decay or regeneration making an assessment such as (3.1), which is based on a presupposed time history, suspect.

A further complication is introduced by the arbitrary criterion used for determining the interface thickness. In many cases it is obvious that the distance between two mixed layers will give the wrong answer such as when there are small mixed layers imbedded in the interface. This type of variability will be considered in detail below when the microstructure of the interfaces is examined. Finally the practical definition of the interface thickness includes the transition zones, and these regions may be quite variable in their thickness and in cases dominate over the salt fingering interface in size.

Thus, it appears that the distance between the edges of two mixed layers, which has an average of 2.6 m for the 18 interfaces with strong images of salt fingers, is not the relevant vertical length scale for salt fingers. This is substantiated by the films where there are rarely more than 2 or 3 consecutive frames with vertical bands. This corresponds to 20-30 cm. To get an independent estimate of the salt finger vertical length scale, h, the constant of proportionality in (3.1) must be estimated. In the context of the collective instability model,

$$B = \frac{D\nu}{C(1-r)} \qquad (3.2)$$

Using a theoretical model based on a variational technique where the salt flux or dissipation of salinity fluctuations are maximized, Stern (1976) has estimated D = 2 ± 1 and r = 0.25, which agree with the range of values determined in the laboratory. Turner (1967) has predicted C = 0.1 cm/sec is an appropriate value of the coefficient in the 4/3 power flux law in the asymptotic range $\frac{\alpha \Delta T}{\beta \Delta S} \rightarrow 1$. Using $\nu = 0.01 \ cm^2/s$

$$B = 0.27 \text{ cm}$$

From the graph in Figure 3.3, a reasonable value of the parameter $\frac{\alpha \Delta T}{\beta \Delta S} (\beta \Delta S)^{-1/3} = 60$, and

$$h = 16 \text{ cm}.$$

The discrepancy between the theoretical value of salt fingering interface thickness and measured distance between mixed layers has been previously noted (Stern and Turner, 1969), but measurements with sufficient resolution have not been previously available to differentiate between the two in the ocean. Since the distance between mixed layers is composed of two turbulent boundary layers called transition zones as well as the salt finger field, it is not surprising that this distance may be poorly correlated to the theoretical interface thickness. In practice these boundary layers are of the order of meters in thickness, and their highly variable turbulent structure may obscure the presence of the salt fingering interface. Because the

interface is turbulent, any one measurement may not be representative of mean conditions, and regions of high gradient within the interface may be transitory turbulent features rather than a quasi-steady field of salt fingers. But the photographs show that regularly spaced vertical structure of bands are not generally found through the distance between layers and are found only on 2-3 adjacent frames. This gives direct support to the theoretical interface thickness. The maximum gradient, ∇T, in Table 3.1 then appears to be the correct representation of the gradient in the salt fingering interface.

For comparison, some of the properties of interfaces where there are thin interfaces bounded by well-mixed layers but no bands on the films are summarized in Table 3.2. These interfaces were chosen because they were relatively sharp and bounded by well-defined isothermal layers. The interfaces in Table 3.1 were chosen because of bands on the photographs in a part of the water column where the salinity is generally decreasing with depth. The interfaces with bands generally have larger and more variable salinity differences. This is consistent with the notion that interfaces without bands may be older or in a run down condition, having expended some of the salinity difference to drive the convection which mixes the layers. Also the maximum temperature gradients within the interfaces with bands are larger while the interface thickness is less. Other parameters do not show significant differences.

3.1.3 Microstructures of Interfaces

The results above suggest that the distance between the edges of two isothermal layers is not the relevant vertical length scale for

TABLE 3.2

Interfaces with Featureless Shadowgraphs

Dive-pressure (decibars)	Differences across the interface ΔT (°C)	ΔS (ppm)	$\Delta\rho$ (ppm)	$\frac{\alpha\Delta T}{\beta\Delta S}$	Max. temp. grad., ∇T (°C/m)	Interface thickness (m)	Layer above (m)	Thickness below (m)
2-1382	.092	18	4	1.3	.137	0.8	8.3	3.8
2-1388	.094	13	5	1.5	.129	4.5	3.8	4.3
2-1408	.123	20	3	1.2	.123	7.3	4.8	11.6
2-1422	.110	16	8	1.6	.081	4.5	11.6	7.3
2-1476	.064	8	5	1.8	.113	1.4	6.8	6.8
2-1571	.064	10	4	1.5	.086	0.8	6.6	9.5
2-1687	.093	14	5	1.5	.047	4.8	13.3	8.4
3-1321	.138	23	10	1.6	.142	8.8	7.6	5.0
3-1552	.090	12	7	1.8	.106	6.2	9.3	7.0
4-1438	.038	8	1	1.2	.064	0.7	3.5	4.0
4-1482	.038	4	3	2.0	.043	1.8	6.3	4.8
4-1490	.063	11	3	1.4	.059	2.4	4.8	5.0
4-1496	.066	9	5	1.7	.175	1.4	5.0	3.8
4-1574	.078	12	5	1.5	.070	4.0	7.3	7.2
4-1588	.117	17	8	1.6	.067	7.5	7.2	3.5
4-1607	.042	6	3	1.6	.074	0.6	4.0	7.6
4-1616	.050	8	3	1.5	.187	0.3	7.6	6.8
4-1622	.059	8	5	1.8	.093	1.9	6.8	6.8
4-1633	.093	16	7	1.6	.092	5.6	6.8	3.9
4-1649	.055	9	3	1.4	.052	2.1	7.6	6.3
Mean	.078	12	4.8	1.5	.097	3.4	6.6	
Standard Deviation	.029	5	2.3	.2	.041	2.6	2.3	
Normalized Standard Deviation	.37	.42	.48	.13	.42	.76	.35	

the salt fingers in the interface, but that the latter scale is approximately 10 cm in the ocean. Analysis in Section 2.2 demonstrated that transition zones must exist between the salt fingers and the convecting layers, but few of the characteristics of these zones can be predicted. Further the separation into interfaces and layers is arbitrary and may not be realistic in some cases. To help interpret the measurements in these uncertain conditions, some specific interfaces are examined as measured both by the CTD and the OSFD.

In Section 2.2, a turbulent boundary layer model of salt finger convection was developed. To summarize, the salt fingers themselves impose an unstable buoyancy flux at the free flexible boundary of the layer, which consists of the transition zone and the adjacent convecting layer. The system is driven by the unstable buoyancy flux and there is no external mean velocity shear imposed. Such a turbulent boundary layer is poorly understood at present, but such an interpretation seems to be consistent with the physics of salt fingers

A turbulent flow is composed of random fluctuations which need not be small deviations from the mean conditions. Since the measurements in this section are single isolated observations of such a random field, they may not be representative of mean conditions. Hence, conclusions about mean conditions based on a single observation should be made cautiously.

The smallest length scale that can be measured with the CTD is determined by the sample rate and the response of its sensors. Here the sample rate is 2.5 Hz which corresponds to a data point every 5 cm

at the sink rate in this experiment. The response time of the platinum thermometer is about 1 s (see Appendix A). In this section, two groups of interfaces have been selected to compare the temperature structure at the smallest CTD scale of those interfaces with and without bands. For the comparison, expanded plots of the temperature and temperature gradient are shown and the points on the profiles where there are strong optical signals are indicated. The interfaces without bands appear to have a lower level of small scale temperature fluctuations even though they may have large gradients.

Although it is desireable to have salinity and density as well as temperature plotted for this discussion, the slow response characteristic of the conductivity sensor leads to small scale density distributions which are unrealistic and they are omitted in this section. The lack of salinity and density information in the use of salt finger convection is particularly unfortunate because temperature is inherently a poor measure of density over small length scales when the convection is driven by salt fingers.

The interfaces which are considered first come at a depth of 1400-1600 decibars and are taken from SCIMP 2. This part of the profile is shown in Figure 3.2, where temperature, salinity, potential density, and temperature gradient are plotted. It is clear from the profile that the density anomalies near the interface are an istrumental artifact.

Ideally, the most simple interface structure is a constant gradient separating two isothermal layers, but practically thermal diffusion and finite sensor response smooth the discontinuities in that distribution.

A close approximation to this ideal is shown in Figure 3.4a, which is an enlargement of the temperature structure of the interface found at a pressure of 1598 db in Figure 3.2. There are a couple of frames of shadowgraphs with strong bands at the center of the interface where the gradient is a maximum. The layer above the interface is nearly isothermal, while there is no well defined layer below. From Figure 3.2, it can be seen that this interface is at the bottom of a series of steps. If a straight line is fitted by the eye through the center of the interface, its slope is approximately $\frac{dT}{dz} = 0.07 \frac{^{o}C}{m}$ which is about seven times the mean gradient for the layer and interface system. A measure of the interface thickness is the distance between the intersection of the line drawn through the interface with the temperature levels above and below the interface. This distance is approximately 0.65 m. The distance measured in this way is compatible with the salt finger model where the interface thickness, h, is defined

$$h = \frac{\Delta T}{d\bar{T}/dz} \tag{3.3}$$

The curvature of the temperature distribution, d^2T/dz^2, is positive at the top of the interface and negative at the bottom, and the whole profile appears to be fairly smooth with no significant inversions present.

Although this interface contained banded images on the shadowgraph, it may be anomalous in some respects. In addition to its location at the base of a staircase, Table 3.1 shows that it is a relatively weak interface as measured by salinity difference, and consequently, the Turner Number, $Tu = \frac{\alpha \Delta T}{\beta \Delta S}$, is relatively large with a value over 2.

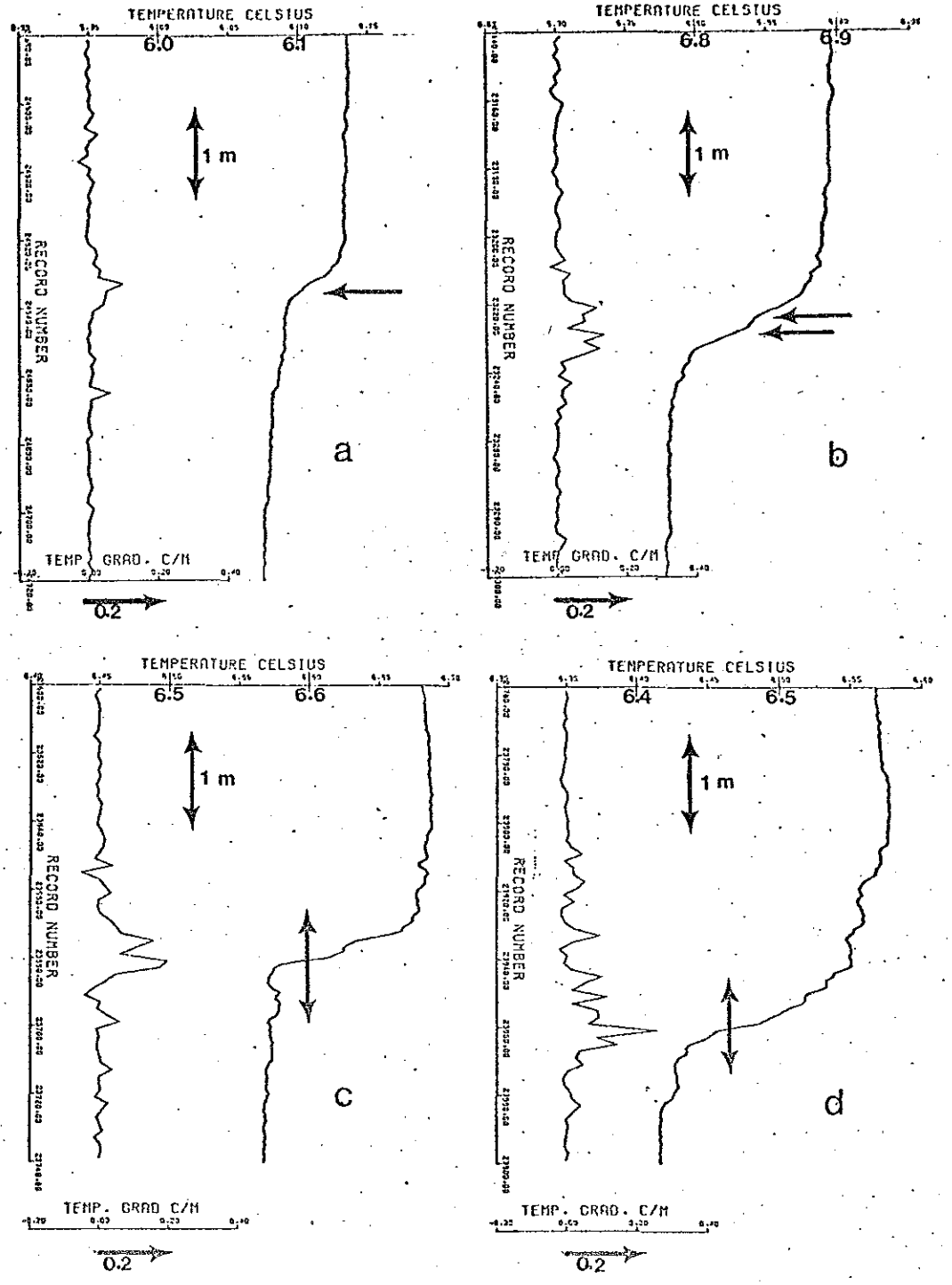

FIGURE 3.4 Interfaces with strong bands in shadowgraphs. The profiles of temperature and temperature gradient are shown with arrows marking the positions of the bands.

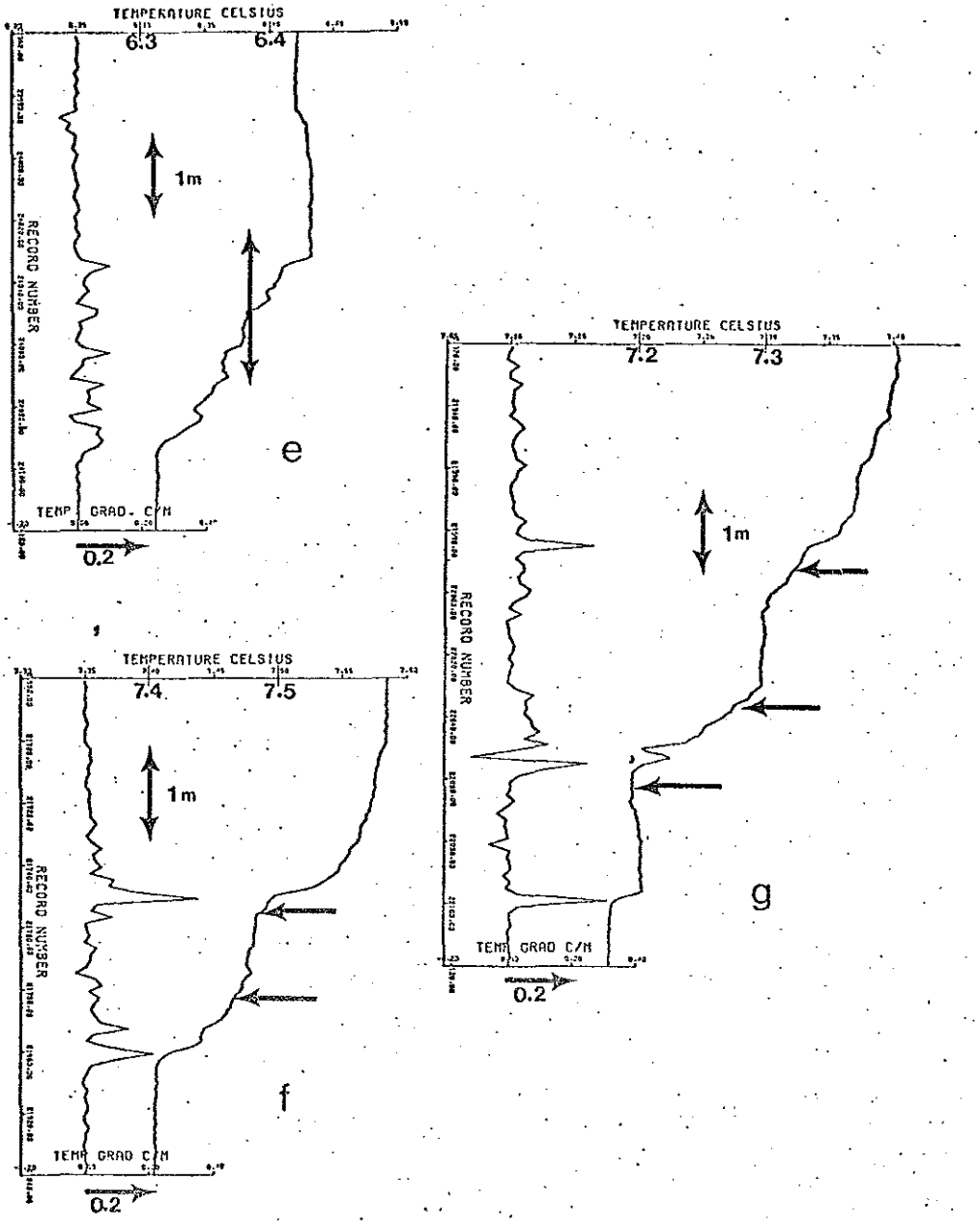

FIGURE 3.4 (continued)

Another example that is similar in form is shown in Figure 3.4b. This interface can be identified in Figure 3.2 at a pressure of 1514 db and it appears to be the uppermost interface in a series. It is similar in shape to the profile in Figure 3.4a but the temperature step across the interface is 2.5 times as great. Again fitting a straight line by eye through the core of the interface gives a gradient $\frac{dT}{dz} = 0.08 \frac{^{\circ}C}{m}$ and thickness h = 1.3 m. These values may differ from those in Table 3.1 because they are measured differently. This interface has several consecutive frames of bands on the shadowgraphs in the lower portion of the interface, but they are still contained within the high gradient region. The shape of the temperature profile is similar to that of Figure 3.4a with positive curvature above, negative below, but there is the suggestion of a higher level of small scale variability in these transitions. This can best be seen by comparing the gradient profiles.

Figures 3.4c and 3.4d are the interfaces at 1540 and 1550 db, respectively, and they can also be identified in Figure 3.2 and Table 3.1. They are near the center of the series of interfaces and display some of the most active images in the shadowgraphs both of bands and more random structures. This high level of microstructure is also seen in temperature and gradient profiles where there are inversions and other nonuniformities on a variety of length scales. The interface thicknesses as defined above are 0.8 m and 1.1 m, respectively. The arguments in the previous section suggest that most of this thickness is transition zone. The banded structure does not completely fill the high gradient region nor is it always confined to that region. This

is a reminder that this profile is one realization of a turbulent boundary layer and may not be representative of mean conditions. In Figure 3.4c there is evidence of temperature fluctuations a meter or so above and below the interface. In particular the temperature inversion below the interface, which is about 0.4 m thick and 0.01°C warmer than the underlying layer, is within the region of strong microstructure on the films and may be related to processes on the interface itself. Unfortunately, the density of this inversion cannot be calculated with sufficient precision to fully determine its dynamics. Consistent with the salt finger model is that this water has passed down through the salt fingers and is accumulating in the transition zone before sinking to the next density interface. If this is such an element it may be modelled as an intermittent plume, which drives the convection in the uniform layer. In order for such an element to sink, it must have an excess of salt relative to the layer that more than compensates in density for its higher temperature. According to the analysis in Section 2.2 such a density anomaly will be rapidly diluted with entrained fluid if the flow is assumed to be self-similar. With a linear growth of the plume diameter, the density decreases with the cube of the distance traveled. With such a rapid dilution the plume rapidly loses its identity and may become undetectable. Such inversions near the interfaces are not uncommon in the data and their presence is implicit in the salt finger model.

Figure 3.4d contains a similar structure at the base of interface where there is a warm layer that is still attached. This may be a developing plume or just a fluctuation in the turbulent boundary layer.

Above the interface core (the maximum gradient) is a layer that is suggestive of the latter, while on top of that is an isothermal layer one meter thick and 5 mC warmer than the layer above. Again the interpretation of such a layer is tentative because the profile is not the mean but a single measurement of a turbulent flow. It is tempting to identify the layer above the interface in Figure 3.4d as water that has sunk through the layer above and accumulated there as an aggregation of many plumes. But it may also have been advected there horizontally.

A more pronounced example of such a layer is shown in Figure 3.4e which is an enlargement of the interface 1563 db in Figure 3.2. In this interface the temperature profile does not have the simple layer interface structure of the profiles in Figures 3.4a and 3.4b. Instead the profile appears to be dominated by turbulent fluctuations so that a high gradient core is no longer recognizable. The inversion layer above the interface is nearly 3 m thick and about 7 mC warmer than the water above it. This inversion does not show microstructure on the shadowgraphs except at its lower boundary. This is consistent with near absence of any temperature fluctuations within the layer which in turn represents a larger length scale than the shadowgraphs. There are bands and turbulent structures on the shadowgraphs throughout the main part of the interface.

The above discussion illustrates how the thermal structure of interfaces appears to be dominated by the turbulent boundary layers of the transition zones, which may obscure the presence of salt fingers on the temperature profile. In other cases the distinction between

layer and interface becomes unclear when there are regions with relatively weak gradients embedded within an interface, and the question becomes when is such a feature a distinct layer. Such an ambiguous profile occurs within the interface at 1435 db, and it is shown in Figure 3.4f. Here the structure may be interpreted as a single distorted interface or two interfaces separated by a thin mixed layer. Although the former interpretation was used in Section 3.1.2 where the characteristics of salt fingering interfaces were summarized, acceptance of the short vertical length scale for salt fingers leads to the possibility of several fields of salt fingers in a single interface. The profile in Figure 3.4f can then be interpreted as two salt fingering interfaces that have become separated by about 2.5 m. The shadowgraphs do not substantiate this interpretation directly because the strongest lines are found where the temperature profile is flat. There are also some weaker lines on the lower high gradient section. Again the consequences of a single realization of a turbulent event must be kept in mind.

As a further example, the next deeper interface is shown in Figure 3.4g. This interface can be identified at a pressure of 1450 db in Figure 3.2. Its structure also strongly suggests the presence of 2-3 small scale interfaces between the two larger scale mixed layers. Again comparison with the films is inconclusive with lines found on both the upper high gradient regions, but the highest contrast bands are below the middle interface at a point on the profile where the gradient is weak.

For comparison, several interfaces are shown where there are no detectable salt fingers on the films. They are taken from SCIMP 4, which was made 2 days after SCIMP 2, but the launch positions were within 3 km of one another. The depth and temperature range for these interfaces are also the same, but the comparison falls short of saying that these are the same interfaces at a later time. Figure 3.5a is a very sharp interface taken from a depth of 1616 m. Using the above formula for interface thickness, an approximate value of 0.2 m is obtained with a maximum gradient of nearly 0.2 C/m. The layers above are quite uniform, more so than Figure 3.4a which is similar in form. The next deeper interface is shown in Figure 3.5b which is somewhat less sharp and is in fact very close in form to Figure 3.4a. Like Figure 3.4a, the temperature differences in 3.5a and 3.5b are small compared to 3.4b-g, so that in this case the shape of the interface appears to be related to the size of the temperature difference rather than the presence or absence of salt fingers on the interface.

The interface in Figure 3.5c is from a depth of 1500 meters and is a clear example of a single interface that is composed of two smaller ones. This interface has no activity on the shadowgraphs, and the differences here are again small compared to a similar interface which has salt fingers (Figure 3.4c). Further examples are shown in Figures 3.5d-f which illustrate that interfaces without activity on the films are often diffuse without any sharp gradients.

In summary, the microstructure of the interfaces can often suggest the presence of variability on a smaller scale as sensed by the OSFD. Sharp interfaces bounded by uniform layers are not necessarily

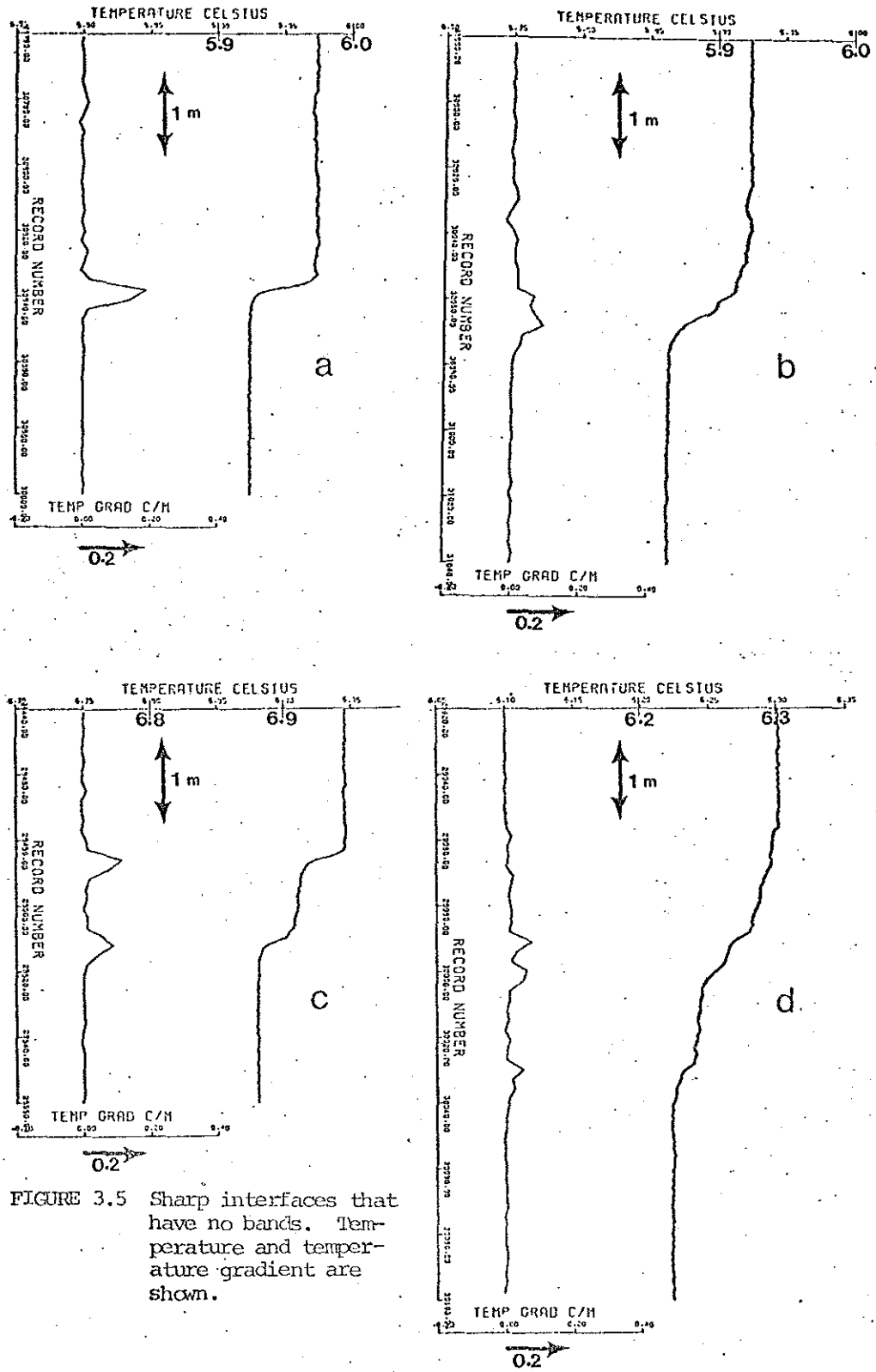

FIGURE 3.5 Sharp interfaces that have no bands. Temperature and temperature gradient are shown.

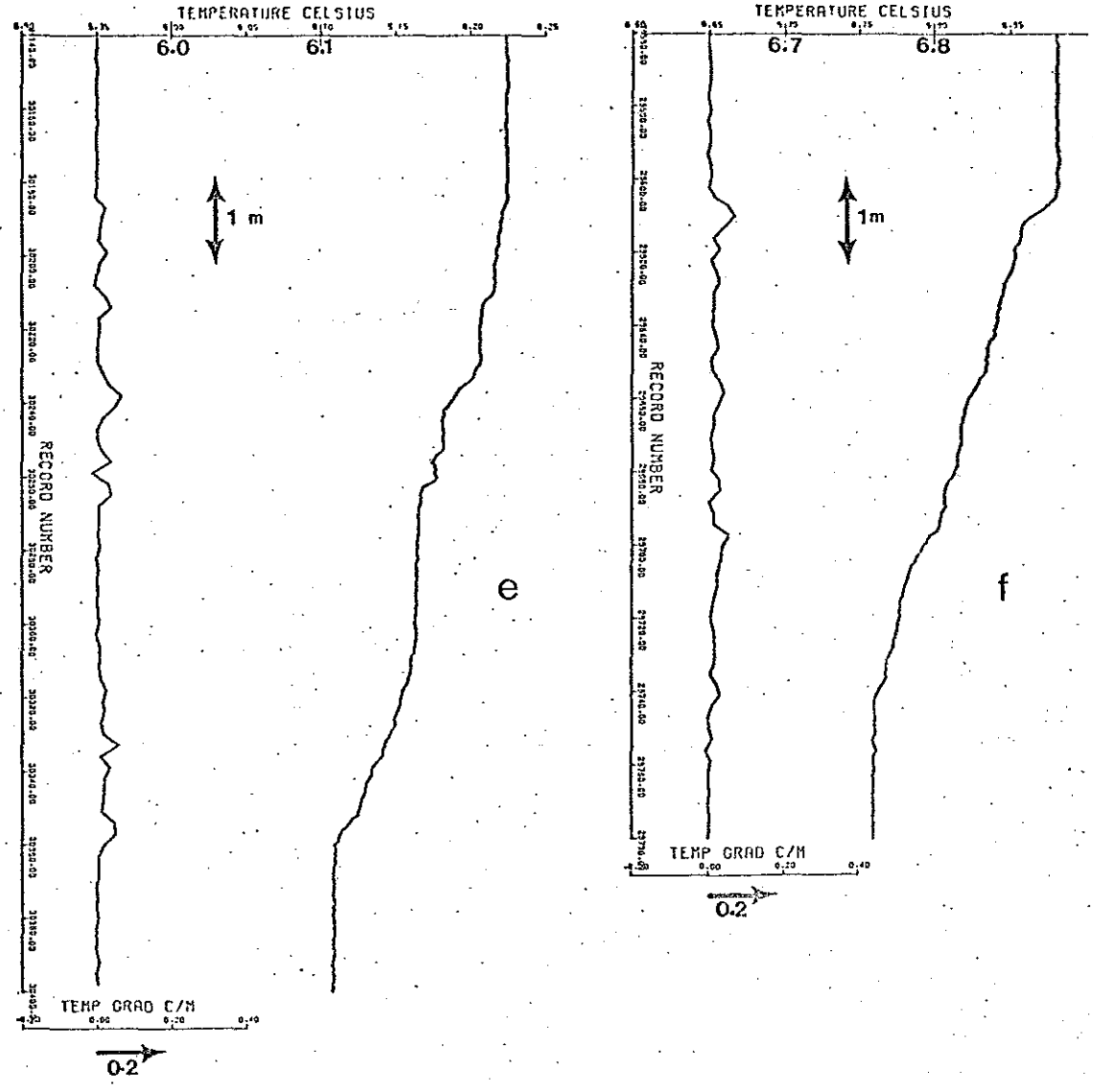

FIGURE 3.5 (continued)

indicative of salt fingers, but they can be present under these conditions. A more distinctive characteristic seems to be the small inversion layers within the interface or at its boundaries as seen in Figures 3.4c-e. This is consistent with a model that includes an unstable buoyancy flux due to salt fingers, while a sharp interface may be due to other causes.

3.1.4 Turbulent Interfaces

Most of the detectable optical signals on the films are from interfaces where the temperature and salinity decrease with depth, and the conditions are appropriate for salt finger convection. And most of the structure on the films has a preferred vertical orientation as may be expected of salt fingers. In this section a slightly different interpretation of the shadowgraphs is employed that does not depend explicitly on the salt finger model. All instances of detectable optical signals are lumped together as turbulent. Although strictly speaking the salt fingers themselves may be laminar, they must be terminated by the turbulent boundary layer called the transition zone. Thus fluid flowing in salt fingers must eventually become part of a turbulent flow. In other cases where the fluctuations in index of refraction are sharp enough to be visible on the millimeter scale, there must be a recent or sustained turbulent event. The question to be addressed then is what are the properties of interfaces where small scale turbulence is visible, and based on these properties what particular generation mechanism is suggested.

Each of the six SCIMP dives recorded shadowgraphs over a depth interval of approximately 800 meters starting at about 1000 meters.

Almost every turbulent observation on the films occurred where the gradients of temperature and salinity were at least several times the mean. In order to make comparisons between situations with turbulence and without, some operational definition of an interface must be adopted. In this section an interface is a place where the gradient of temperature or salinity is several times the mean when averaged over the interval of a few tens of centimeters to several meters. Although arbitrary and inexact, such definitions are often necessary to make any headway.

Two independent compilations have been made which form the basis of this section. In the first all interfaces on the profiles have been identified using the criterion described above, using only that section of the profiles where the shadowgraph system was operating. There were approximately 400 identified among the six profiles. In the second compilation, the films were scanned for all instances of turbulence and the location and intensity of these were noted. In comparing the two data sets, somewhat more than 100 of the interfaces were found to be turbulent while only a few instances of turbulence were not on an interface.

Figures 3.1 and 3.6 - 3.10 show the entire profiles of temperature, salinity, and potential density for the six dives. The level at which the descent weight was dropped to slow the instrument and the camera is turned on is indicated, and in all cases, the film lasted all the way to the maximum depth of the dive. The film is started at a depth that is shallower than the deep salinity maximum so that each dive includes segments with both increasing and decreasing salinity.

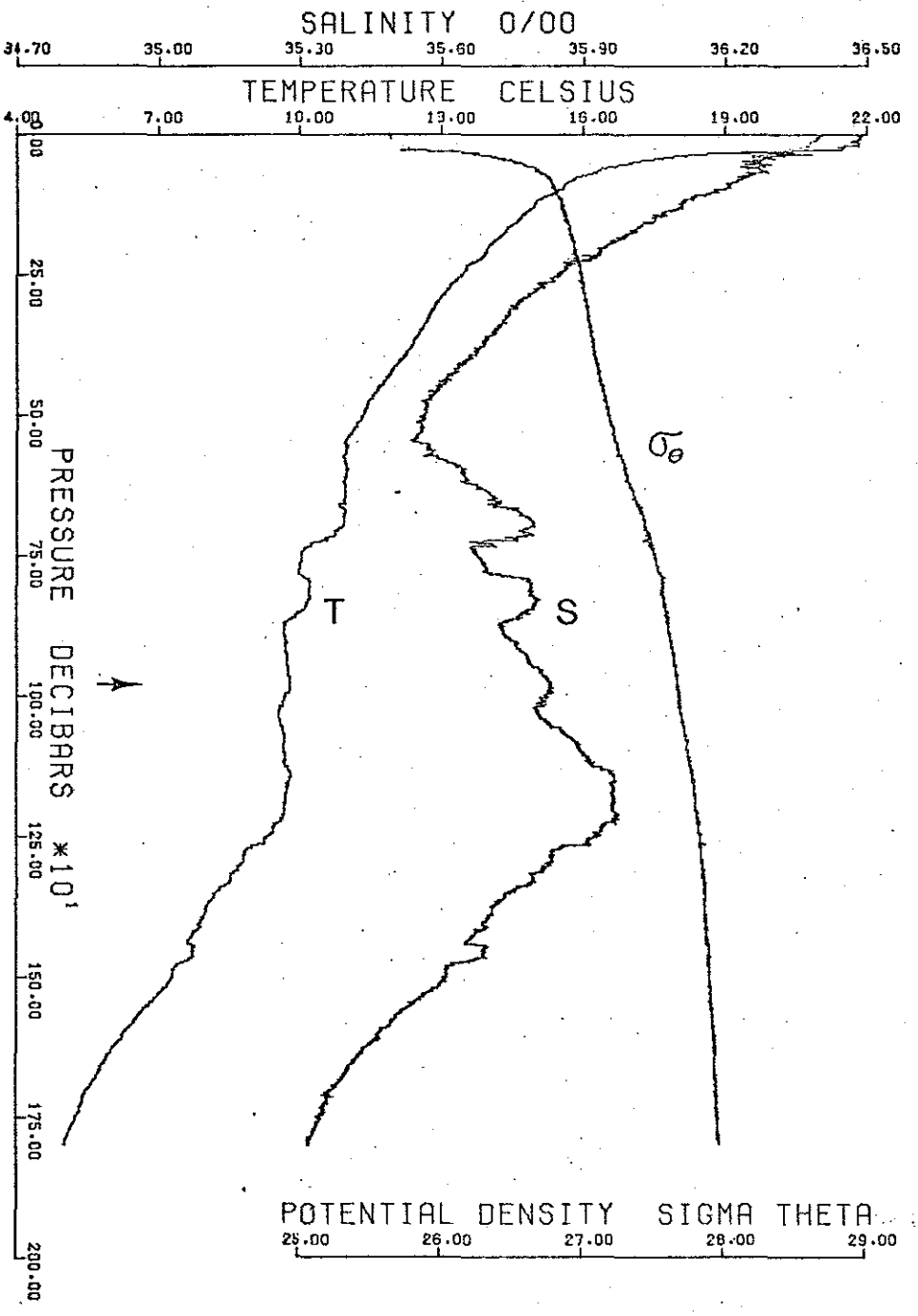

FIGURE 3.6 Profiles of temperature, salinity, and potential density for SCIMP 1. Launch at 0930Z, 16 July 1973; 34-58.4°N, 10-28.1°W. The arrow indicates where the OSFD was turned on.

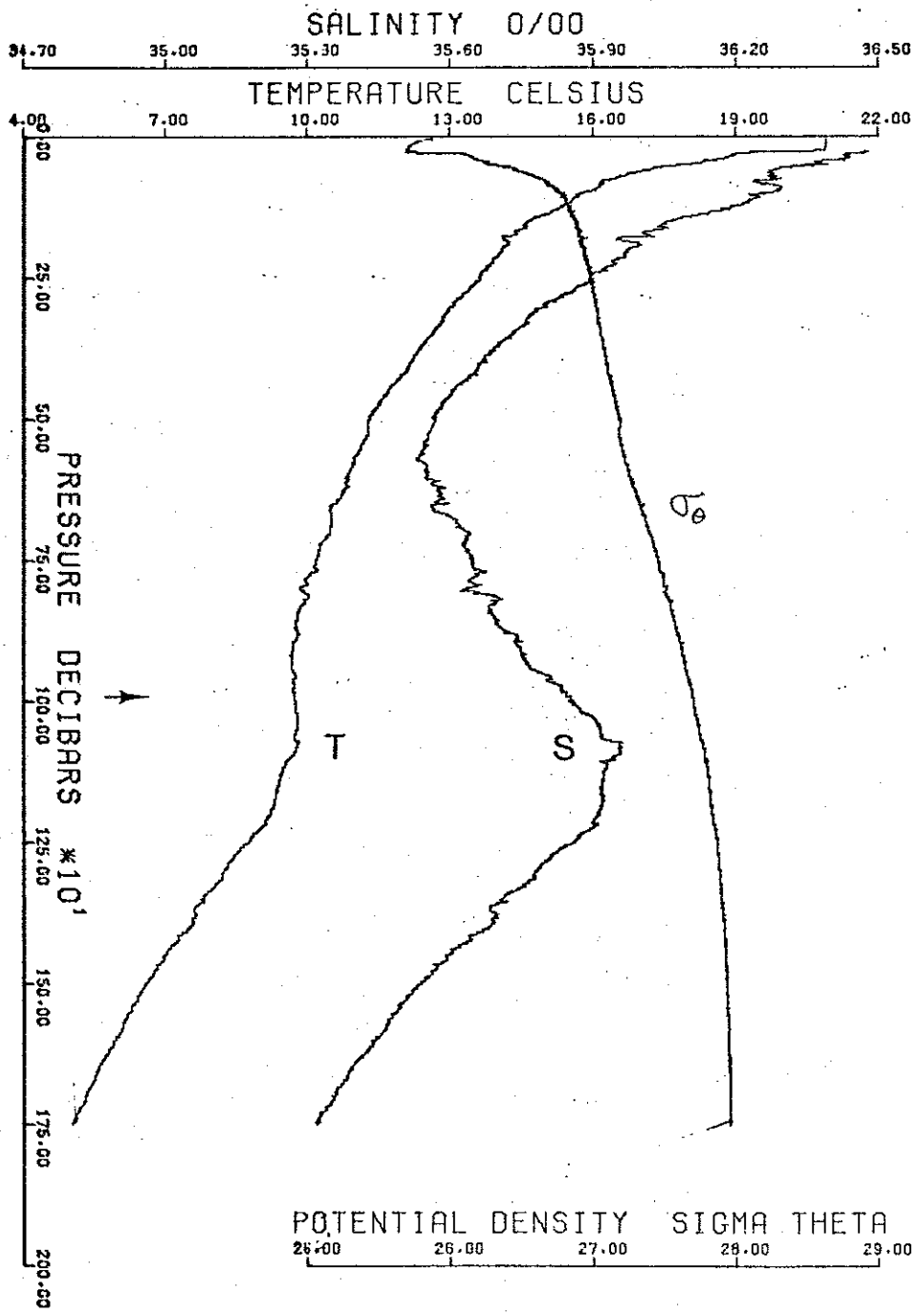

FIGURE 3.7 Profiles of temperature, salinity, and potential density for SCIMP 3. Launch at 0710Z, 19 July 1973; 34-06.0°N, 11-09.1°W. The arrow indicates where the OSFD was turned on.

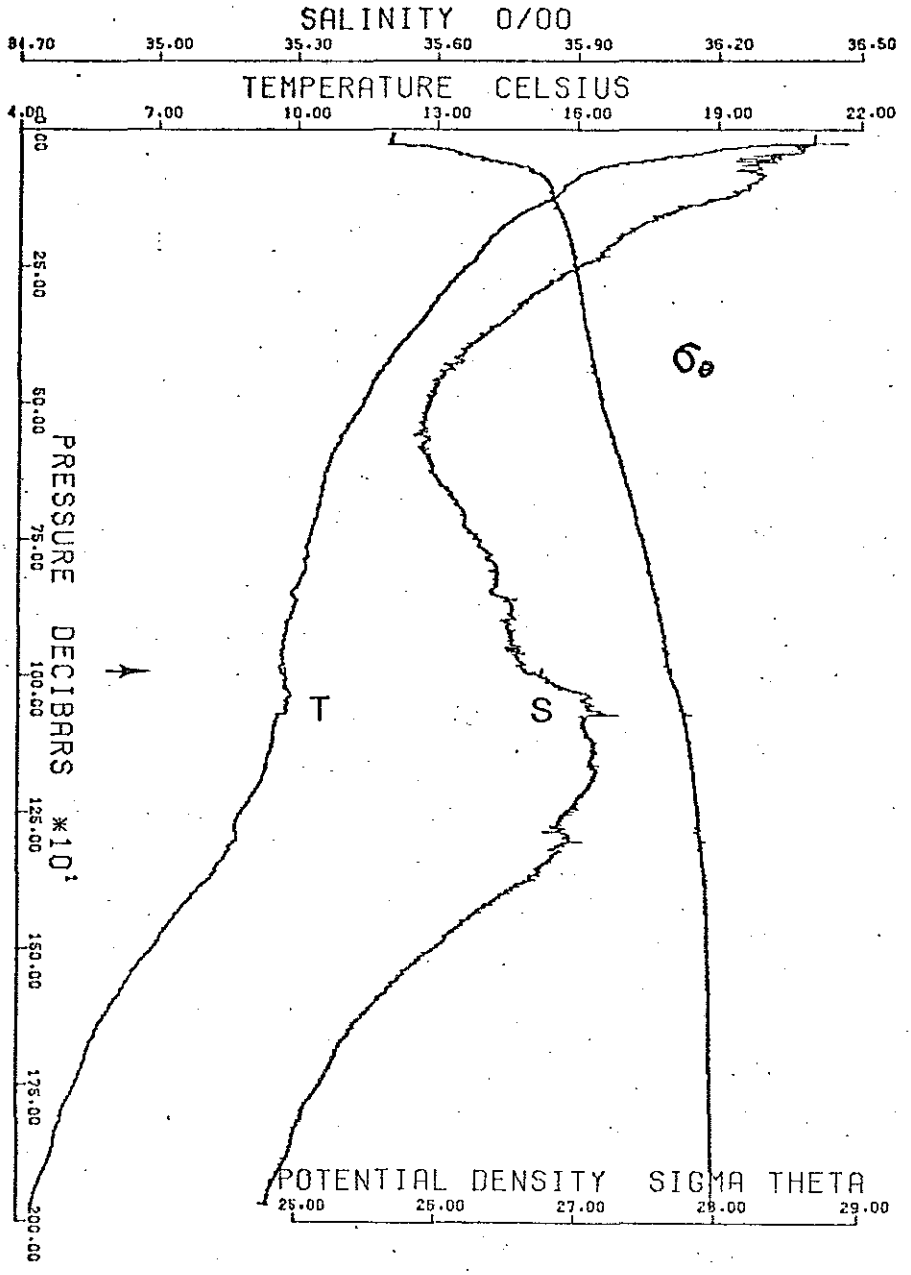

FIGURE 3.8 Profiles of temperature, salinity, and potential density for SCIMP 4. Launch at 0340Z, 20 July 1973; 34-14.0°N, 10-51.2°W. The arrow indicates where the OSFD was turned on.

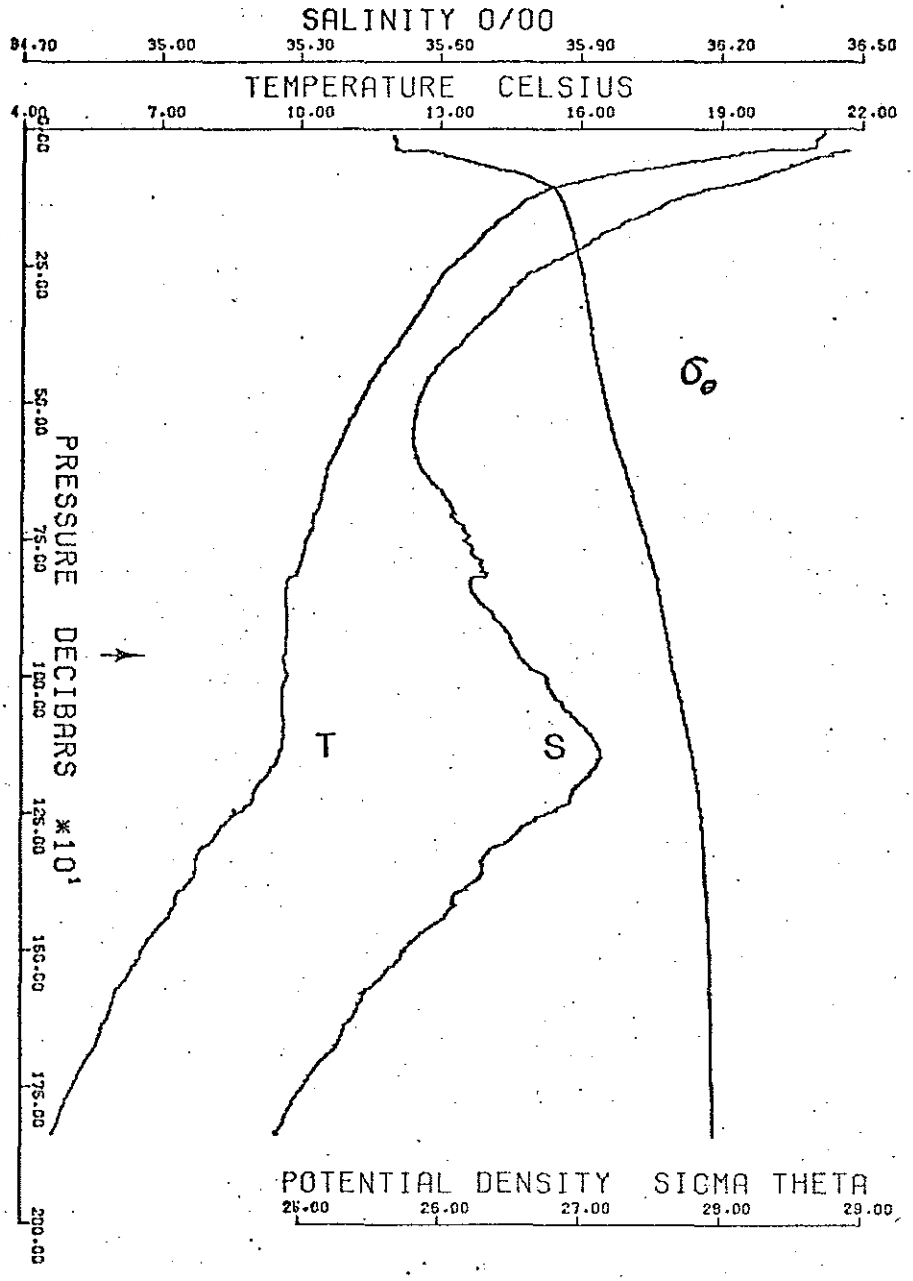

FIGURE 3.9 Profiles of temperature, salinity, and potential density for SCIMP 5. Launch at 1817Z, 20 July 1973; 34-22.5°N, 11-14.5°W. The arrow indicates where the OSFD was turned on.

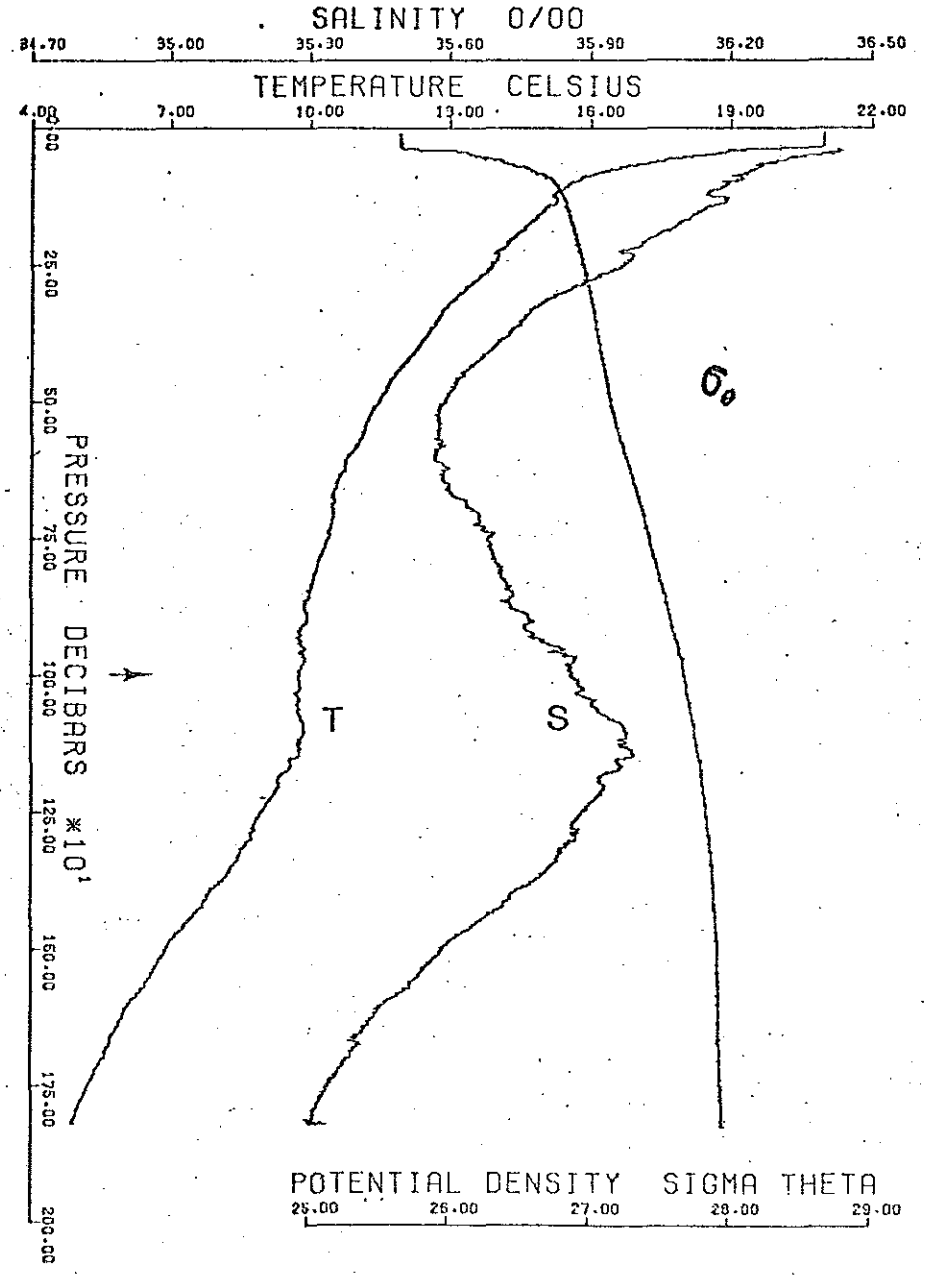

FIGURE 3.10 Profiles of temperature, salinity, and potential density for SCIMP 6. Launch at 0923Z, 21 July 1973; 34-15.0°N, 10-50.0°W. The arrow indicates where the OSFD was turned on.

Generally temperature decreases where salinity decreases and vice versa, but there are sections where salinity increases and temperature decreases. Increasing temperature with decreasing salinity is gravitationally unstable and is never seen. It has been shown above that double diffusive instabilities that lead to overturning and turbulence are possible when the temperature and salinity gradients are the same sign. On all dives the majority of the section where the camera was on had decreasing temperature and salinity.

The first thing to be examined is the distribution of both interfaces and turbulence with depth. Figure 3.11a shows the number of interfaces for each of the six SCIMP dives as a function of depth, which is divided into 100 m increments. The number generally decreases with increasing depth except for some lower values in the range 1.1 - 1.3 km. The distribution of turbulent interfaces shown in Figure 3.11b is similar in shape to the total number of interfaces, but the frequency of turbulence in the range 1.0 - 1.1 is no longer maximum. There is a pronounced peak in the 1.3 - 1.4 km range in this case. Also shown in Figure 3.11c is the fraction of total interfaces that have turbulence. This fraction seems to be nearly constant at about 0.4 - 0.5 in the interval 1.2 - 1.6 km, but it is 0.3 or less above and below this interval. It should be noted that all turbulent events are grouped together in Figure 3.11 no account being taken of the apparent variations of contrast in shadowgraph images.

The results of Section 2.3 imply that the shear of the internal wave motions is concentrated where the local density gradient is large. The criterion for breakdown by shear instability into turbulence depends

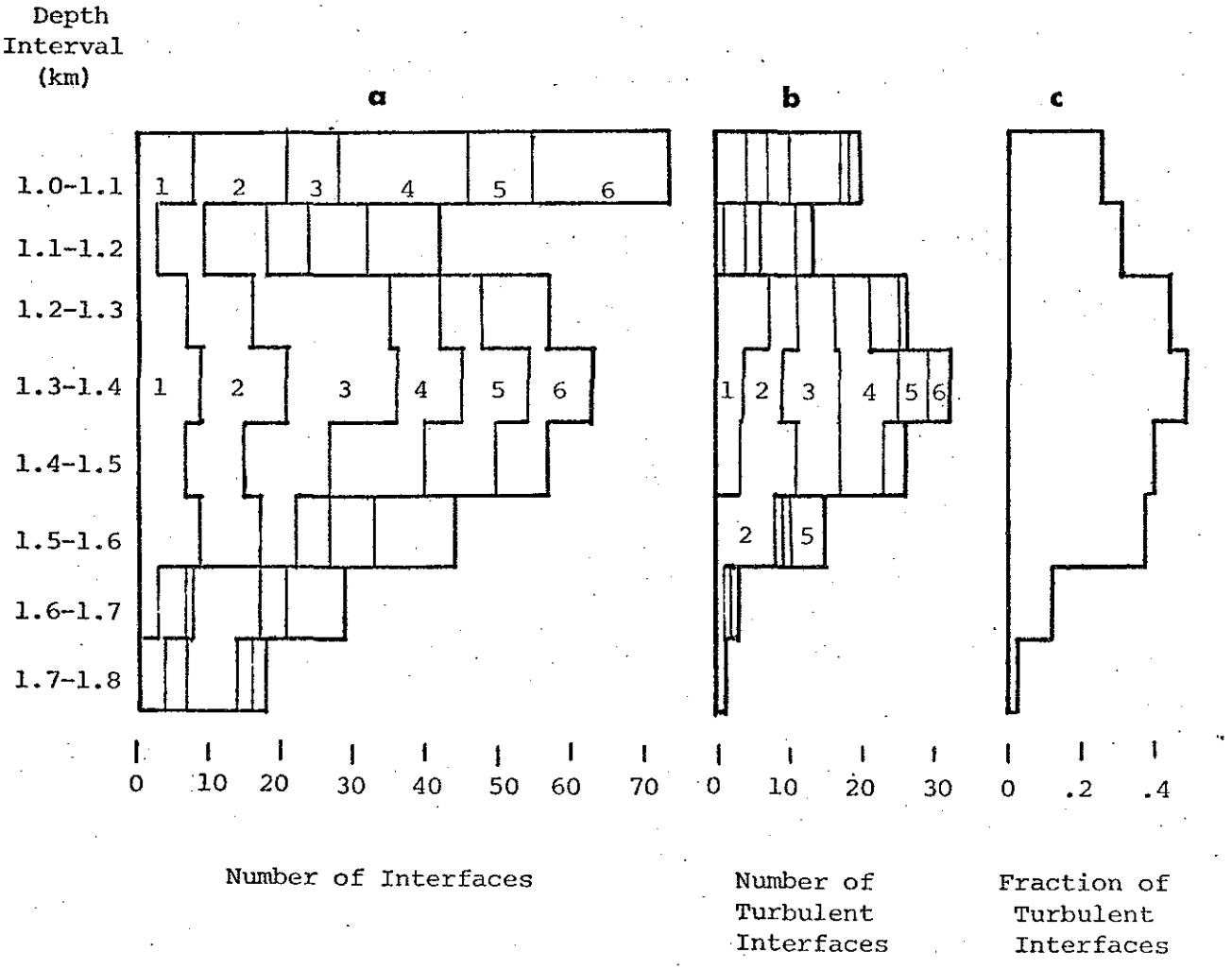

FIGURE 3.11 Distributions of interfaces and turbulent interfaces for the 6 SCIMP dives as a function of depth. The depth interval between 1.0 and 1.8 km is divided into 100 m increments for the census. The numbers within the diagrams show how the interfaces are distributed among the dives. The diagram on the right shows what fraction of interfaces are turbulent as a function of depth.

on the Richardson Number, Ri, which can be written for an interface of thickness h as

$$R_i = \frac{g}{\rho_0} \frac{\Delta\rho h}{(\Delta u)^2} \qquad (3.4)$$

where $\Delta\rho$ and Δu are the density and velocity differences across the interface. Flows are stable to shear when $Ri > 1/4$ and small disturbances may grow otherwise. If an extisting irregular vertical distribution of density is subjected to internal wave motion with a vertical wavelength that is large compared to the vertical length scale of the density irregularities, Phillips (1966) has shown that the internal waves reduce the local Richardson Number at the pre-existing maximum in the density gradient. This suggests that turbulence due to shear instability breakdown should be found preferentially on interfaces with a large density difference. To see if there is a relationship between the density difference and occurrence of turbulence, Figure 3.12 shows the distribution of interfaces and the distribution of interfaces with turbulence as a function of density difference across the interface. More than half of the interfaces have a density difference in the range 2-4 ppm, while the turbulent interfaces appear to be more uniformly distributed. This can be seen more clearly in Figure 3.12b where the fraction of total interfaces which are turbulent is shown as a function of density difference across the interface. The fraction generally increases with increasing density difference, so that only interfaces with $\Delta\rho > 6$ ppm have a turbulent fraction significantly greater than the average. An estimate of the order of magnitude of the velocity difference that

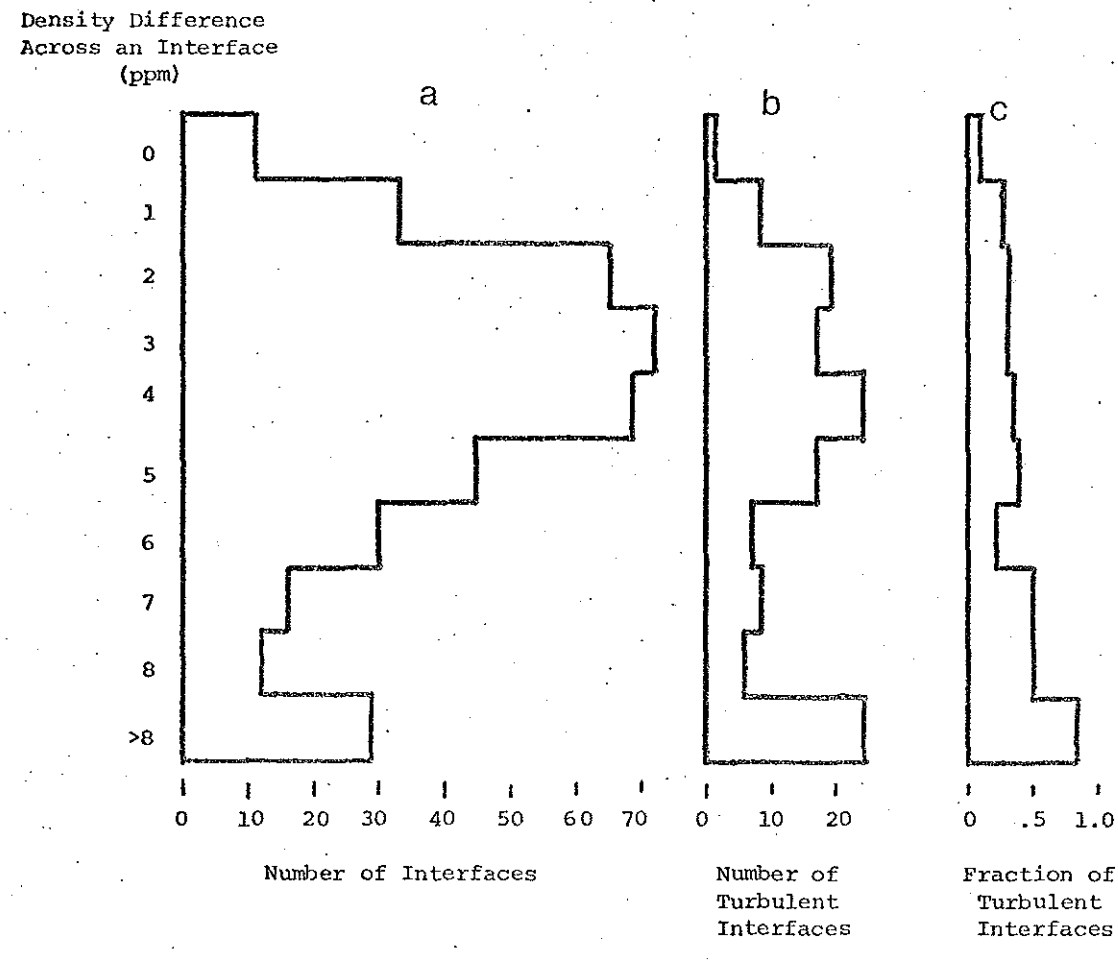

FIGURE 3.12 Distributions of interfaces and turbulent interfaces as a function of density difference across an interface. The fraction of turbulent interfaces is shown on the right.

may be associated with this turbulence can be made by taking Ri = 0.1, $h = 2 \times 10^2$ cm and $\frac{\Delta\rho}{\rho_0} = 10^{-5}$. This gives a velocity difference $\Delta u = 4.5 \frac{cm}{s}$, which is a very large shear for the deep ocean. Such a large requisite shear makes instability involving the entire interface unlikely. However, smaller scale shear instabilities within the interface are not ruled out by these data, and Woods and Wiley (1972) have observed that the proper length scale may be an order of magnitude smaller than the 2 m used in the calculation. The sensors used can not reliably measure large density differences over less than a meter and the interface thickness and corresponding velocity differences for instability may be much smaller than indicated by the measurements.

The two most likely causes of small scale turbulence in the ocean are shear instability and double diffusive convection. Shear instability is favored under conditions of strong density gradient in the presence of internal gravity waves, but the above calculations indicate that it is probably not responsible for the interface-layer structure in the Mediterranean Outflow. However, the evidence is weak and inconclusive and some more direct evidence in favor of double diffusive convection would be more satisfying. The vertical banded structure that is characteristic of salt fingers visible on many interfaces where salt fingers are to be expected is helpful, but some interfaces show vertical bands where salt fingers are impossible and some interfaces have no detectable optical signal where salt fingers should be present. This should not negate the value of the shadowgraphs, but some other confirmation based on the properties of salt fingers and the properties of the interfaces measured by the CTD would be reassuring.

Necessary conditions for salt fingers are derived from Section 2.1 above as

$$\frac{\alpha \, dT_s/dz}{\beta \, dS_s/dz} < \frac{1}{\tau} = \frac{K_s}{K_T} \cong 10^{-2} \qquad (3.5)$$

and dT_s/dz , $dS_s/dz > 0$. The first condition is a very weak constraint and is satisfied almost everywhere in the ocean where the second condition is fulfilled. Huppert and Manins (1973) have derived a slightly less restrictive form of (3.5) and verified it experimentally. They found a power law of $\tau^{-3/2}$ rather than τ^{-1} as derived above. Neither bound is approached for the data discussed here so salt fingers must be considered possible whenever dT_s/dz , $dS_s/dz > 0$.

The ability to see turbulence in the shadowgraphs depends on the curvature of the refractive index distribution. In the case of salt fingers this curvature is approximately proportional to the salinity difference between two adjacent fingers, which is in turn thought to be a constant fraction of the salinity difference between two convecting layers. Figure 3.13 shows the distribution of interfaces and the distribution of interfaces with turbulence as a function of salinity difference across the interface. According to the sign convection used, ΔS when $dS_s/dz > 0$, i.e., the salinity decreases with increasing depth. Approximately 2/3 of the interfaces have salinity differences in the range 0-14, and most interfaces with salinity differences greater than this show turbulence. This is shown most dramatically in Figure 3.13c where the fraction of turbulent interfaces is given as a function of salinity differences. Some of the extreme groups have been combined in the figure to make the number of samples

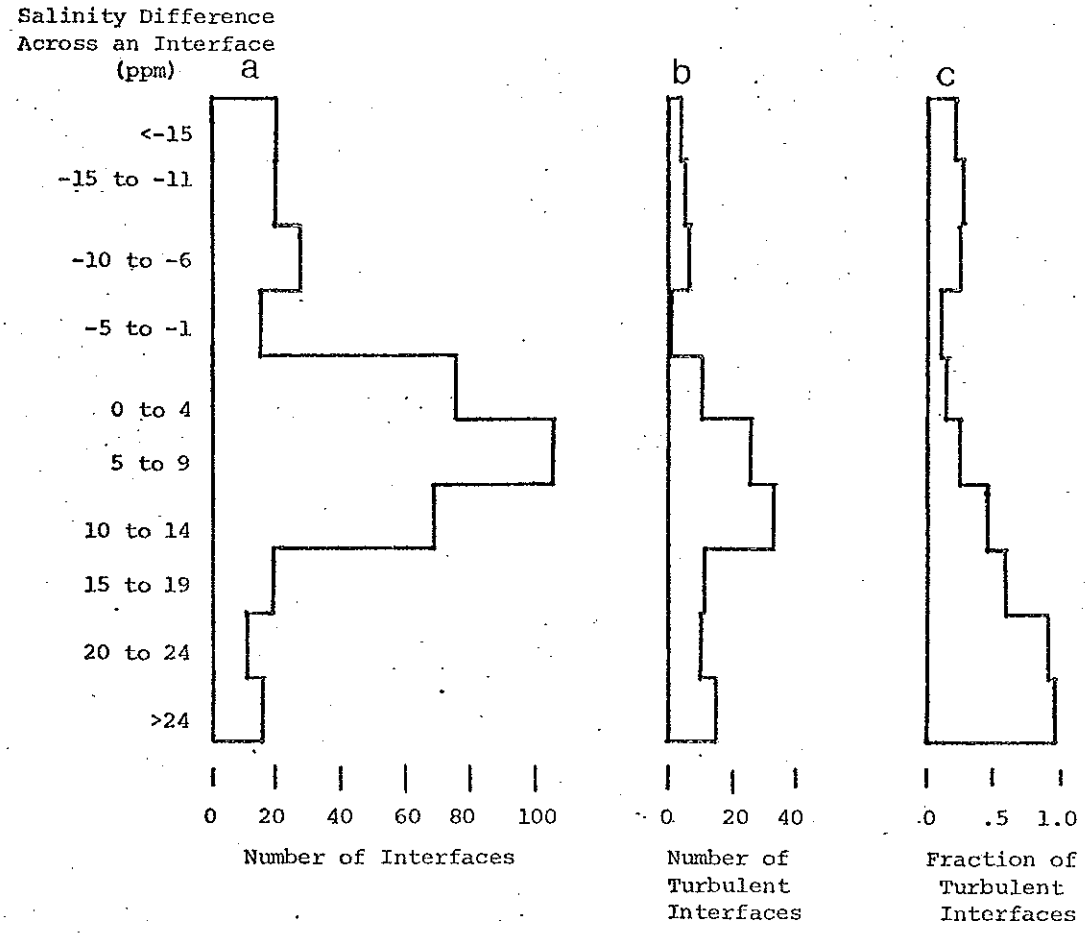

FIGURE 3.13 Distributions of interfaces and turbulent interfaces as a function of salinity difference. When salinity decreases with increasing depth, the salinity difference is positive. The fraction of turbulent interfaces is shown on the right, and it is monotonically increasing with increasing positive salinity difference.

in each group more uniform. Only interfaces with large positive salinity differences have an above average fraction of turbulence. Interfaces with large positive salinity differences tend to have large density differences, so there should be a more sensitive measure for discriminating between turbulence due to double diffusive convection and shear instability.

The ratio of the changes in density due to salinity to that due to temperature or the inverse has been called the Turner Number. Here the definition

$$T_u \equiv \frac{\alpha \Delta T}{\beta \Delta S} \tag{3.6}$$

is adopted, i.e., the density change due to temperature divided by that due to salinity. By comparison, the linear equation of state for constant pressure

$$d\rho = -\alpha\, dT + \beta dS \tag{3.7a}$$

can be rewritten

$$d\rho = \beta dS (1 - T_u) \tag{3.7b}$$

In the salt finger case where temperature and salinity both decrease with increasing depth, the distribution is stable, $\frac{d\rho}{dz} > 0$, where $T_u > 1$ since $\frac{\beta dS}{dz} > 0$. When temperature and salinity both increase with depth, the diffusive case, $\frac{d\rho}{dz} > 0$ when $T_u < 1$. In both cases, $T_u = 1$ represents neutral stability.

Laboratory measurements by Stern and Turner (1969) have shown that the nonlinear regime where salt fingers break down into sharp

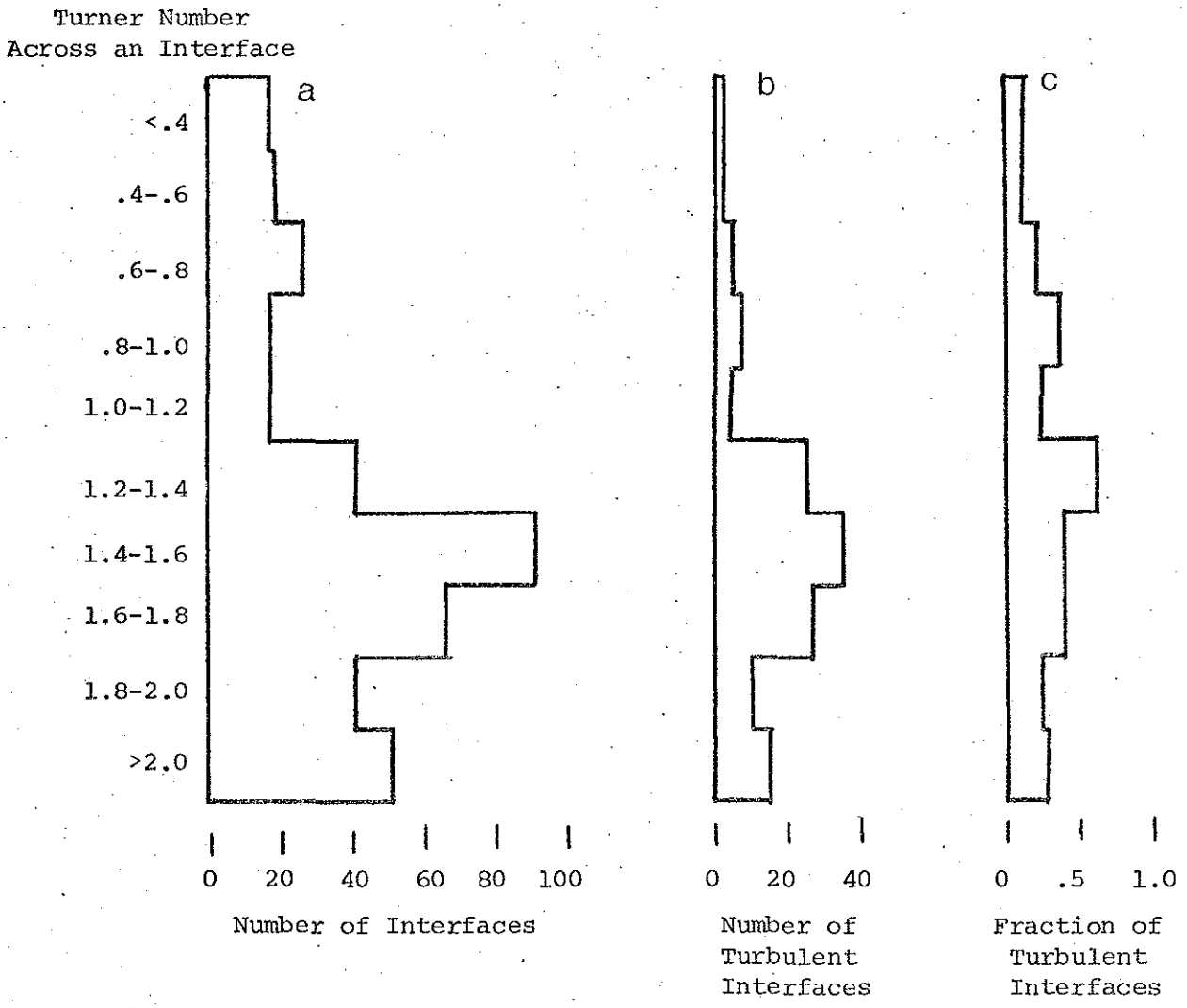

FIGURE 3.14 Distributions of interfaces and turbulent interfaces as a function of Turner Number, $Tu = \alpha\Delta T/\beta\Delta S$. The fraction of turbulent interfaces is shown on the right.

interfaces and convecting layers is favored as the Turner Number becomes small. Figure 3.14 shows the distribution of interfaces and the distribution of turbulent interfaces as a function of Turner Number. There are many more cases where the salinity decreases with depth than increases, but this primarily reflects the distribution of salinity in the sampling region. To see if a particular value of Turner Number may favor turbulence, Figure 3.14c shows the fraction of interfaces which are turbulent. This distribution has a distinct maximum at Tu = 1.2 - 1.3, where over 0.6 of the interfaces are turbulent. It is somewhat puzzling that such a small fraction of interfaces in the parameter range Tu = 1.0 - 1.1 are turbulent, but there are many weak interfaces in this range. That is, temperature, salinity, and density difference are all small. This means that the refractive index variations are correspondingly low and the images may be too weak to be detectable. Regardless, Figure 3.14 shows a tendency for a larger turbulent fraction near Tu = 1.0 (low stability) both for decreasing and increasing salinity. This should be taken as evidence in favor of double diffusive convection.

The gross properties of the water column can be compared to the occurrence of interfaces in the area. The mean gradients of potential temperature, salinity and local potential density (see Appendix C for definition and discussion) are shown in Figure 3.15. These profiles were compiled for each of the six SCIMP dives by taking differences over 100 decibar intervals. Each successive profile is offset to the right from the previous one to make comparison easier. The average profile for each is also shown and the standard deviation is

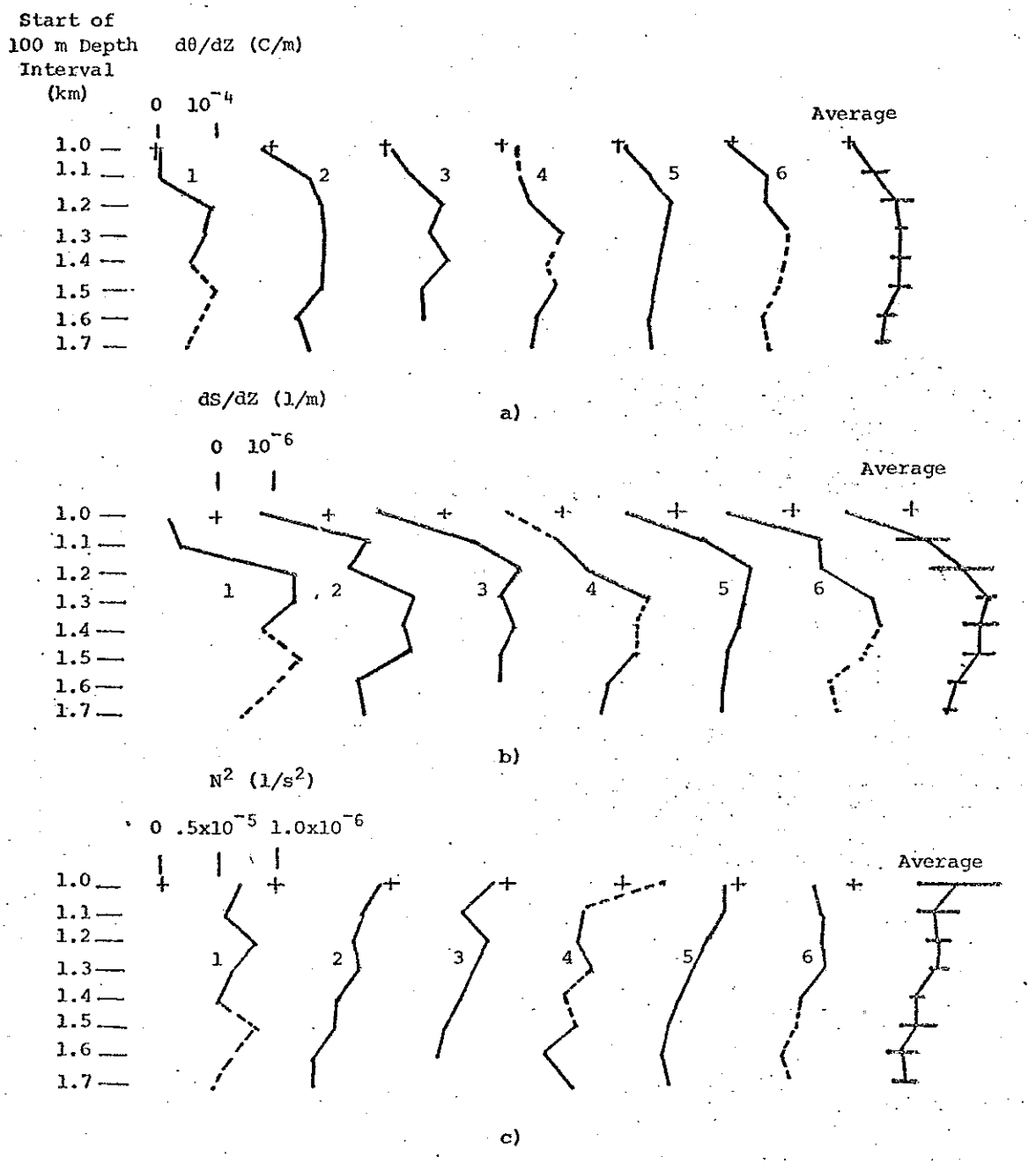

FIGURE 3.15 Mean gradient profiles of a) potential temperature, b) salinity, and c) density expressed as the square of the Brunt-Väisälä frequency. Each of the 6 SCIMP dives is plotted as well as the average of the 6. The standard deviation is shown as a horizontal bar at each level on the average. Each profile is offset horizontally by a constant distance as indicated by the positions of the crosses. The profiles are dashed where the pressure sensor was performing erratically.

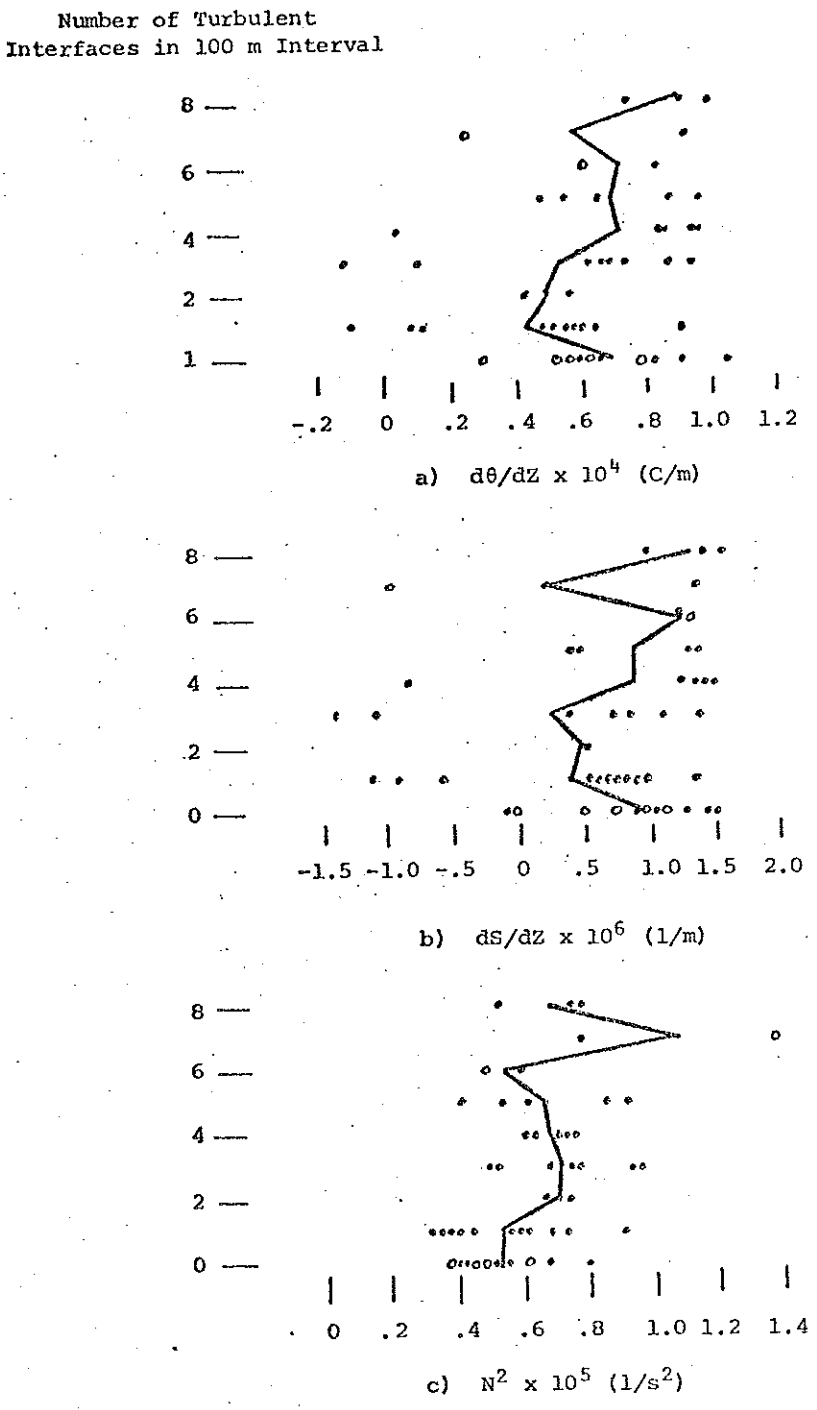

FIGURE 3.16 Number of turbulent interfaces versus mean gradients of a) potential temperature, b) salinity, and c) density expressed as N^2. Each point represents a 100 m interval from one of the 6 SCIMP dives. The open circles are from intervals where the pressure signal was erratic.

indicated by a bar on either side of the average. Sections of the individual profiles which are dashed are questionable because the pressure signal was acting erratically in that interval.

The average potential temperature gradient varies from slightly negative in some cases near a depth of 1.0 km to a maximum of near 10^{-4} C/m at 1.4 km. For salinity, the range is about -1.4×10^{-6} 1/m to 1.5×10^{-6} 1/m and density in terms of N^2 varies from about $.3 \times 10^{-5}$ $1/sec^2$ to 1.0×10^{-5} $1/sec^2$. Comparison of distribution of turbulent interfaces in Figure 3.13 with the profiles in Figure 3.15 suggests that there may be a correlation with large mean salinity gradient. To test this impression, Figure 3.16 shows the numbers of turbulent interfaces in a 100 m depth interval as a function of the mean potential temperature, salinity, and local potential density differences. Each data point represents one 100 m interval and the open circles represent points where the pressure was behaving erratically and the salinity and density may be poorly estimated. A line representing the average gradient for a given number of turbulent interfaces is drawn on each graph. The averages at 0, 6, and 7 turbulent interfaces may be unrealistic because half the number in the average are instances where the pressure is faulty. If those three levels are given less weight, the number of turbulent interfaces seems to increase systematically with increasing potential temperature and salinity gradient, but it does not appear to depend on the mean density gradient.

3.1.5 Spectra of Stepped Structure

Internal gravity wave motions are a fundamental characteristic of stratified fluids, and they often appear to dominate the measured

fluctuations in the parameter range of finestructure. Based on several sets of measurements, a model spectrum for internal wave fluctuations has been synthesized by Garrett and Munk (1972) and subsequently refined (Garrett and Munk, 1975). Since internal waves includes fluctuations in all three space dimensions as well as time, the power density of the model spectrum includes wave number and frequency dependence. The characteristics of internal waves that are usually measured are currents and displacements of constant density surfaces.

In this study the vertical profile of temperature is measured by SCIMP and by a CTD lowered on a cable. In the terminology of Garrett and Munk these can be used to compute "dropped spectra." Based on a set of measurements by Hayes et al. (1975), a model dropped spectrum for temperature has been formulated. It is derived from measurements at several depths in the western Sargasso Sea using a WHOI/Brown CTD. The temperature spectra are modeled with a constant slope of -2.5 independent of depth, by fitting a straight line. This is a purely emperical result which does not appear to have any theoretical basis. However, the assumption of a slope of -2.5 is consistent with the spectra from tows by Katz (1974) according to the internal wave model.

Garrett and Munk present scaling laws by which sets of measurements under different conditions may be related to the universal spectrum. In the case of vertical temperature profile, the resultant autospectrum has the units $(^{o}C)^{2}$/cycle/decibar. To relate this measurement to a characteristic of internal waves, it is assumed that the temperature profile is distorted from a more uniform state by internal

waves. The temperature spectrum is then converted to a displacement spectrum by normalizing it with the square of the mean potential temperature gradient. Calling the autospectrum of the vertical temperature profile $F_T(k)$, where k is the vertical wave number, the displacement spectrum is then

$$F_\zeta(k) = F_T(k) / (d\bar{\theta}/dz)^2 \tag{3.8}$$

where ζ is the vertical displacement of an isotherm and $d\theta/dz$ is the mean potential temperature gradient. When the temperature gradient is written in terms of $^{\circ}$C/decibar, then the dimensions of the displacement spectrum are

$$[F_\zeta(k)] = \text{(decibars)}^2/\text{cycle/decibar} \tag{3.9}$$

or in some cases meters are used interchangeably with decibars following oceanographic convention. The measurements of Hayes et al. suggest that the displacement spectrum may be universal, since these spectra agree to within a factor of two except within the Mediterranean Water. However, the Mediterranean Water is not correctly represented by the displacement spectra because temperature is not a good indicator of density there and the density is, of course, the important factor in the dynamics of internal waves. Garrett and Munk have suggested additional scaling of both the displacement spectrum and the wave number to obtain the universal spectrum. Using the local buoyancy frequency, N, as a scale factor, they derive

$$F_\zeta^*(\gamma) = N^2 F_\zeta(\gamma) \tag{3.10a}$$

where

$$\gamma = \frac{\chi}{N} \qquad (3.10b)$$

as the universal spectrum. From Hayes et al., it appears that this normalization does not lead to more consistent results than the unnormalized displacement spectrum.

Although the stepped structure was measured only a few times with SCIMP, a more extensive time series was made with the cable lowered CTD. Since the instrument used on this cruise was nearly identical to the WHOI/Brown CTD used by Hayes et al., a very good comparison can be made. The only known difference between the two instruments is the fast response temperature compensation network used in the instrument in the present study. A thermistor is used to compensate for the slower response of the platinum thermometer and extend the measured temperature spectrum to higher wavenumbers. The effect of this modification is negligible at low wavenumber. The data processing used here is thought to be identical to the procedures used by Hayes et al.

Before comparing the spectra from the WHOI/Brown CTD lowered on a cable to the results of Hayes et al., a particular aspect of vertical temperature spectra can be examined. Namely, how do ship motions affect the measured spectra when a CTD is lowered on a cable? Pingree (1971) has suggested that much of the stepped structure measured in the ocean may be attributable to ship motions. A related problem is how do ship motions impressed on a CTD traveling through layered structure affect the resultant power spectrum. Pingree's arguments are not relevant here because the stepped structure has been confirmed with

the CTD on SCIMP. Since SCIMP has no connection with the surface, it cannot be affected by surface waves. There may be some effective vertical velocities due to internal waves, but this effect appears to be small (based on examining the pressure record), and any significant effects should be at very low vertical wave number.

The first comparison considers an ensemble average of 5 CTD stations through the steps and a SCIMP dive at the same approximate location made sometime near the middle of the group of CTD's. Although it is not possible to identify common features between the set of CTD's and the SCIMP dive because of differences in calibrations, it is reasonably certain that they are measuring the same water column at the same time. Because the instruments have different sampling characteristics, the preliminary data processing is somewhat different. The CTD is lowered at a rate of 90 m/min. while pressure, temperature and conductivity are each sampled at 30 Hz. This gives a sample point approximately every 5 cm on the average compared to the pressure resolution of 0.1 dbar. The data points are not evenly spaced because of the ship motions and noise in the system. In the processing, wild points are first edited from the data when it is sorted to a uniform pressure series at 0.1 dbar interval. Most pressure values will have more than one data point assigned to it while some have none. The uniform series is then obtained by a combination of averaging and interpolating. By comparison, the SCIMP data need only be checked for wild points (which are rare). The assumption is made that the SCIMP sinks at a constant rate; consequently the data points are evenly spaced in pressure. This means that no pressure sorting is

necessary to create a uniform series, which in this case is sampled approximately every 5 cm.

Table 3.3 summarizes some of the mean properties of the temperature data used to generate spectra. The data was chosen to encompass the stepped structure rather than a specific temperature or pressure interval. SCIMP was deployed at a time between CTD 11 and CTD 12.

TABLE 3.3

Data Set	Pressure Interval (decibars)	Temperature Interval (°C)	$\overline{d\theta/dz}$ °C/km
CTD 8	1475 - 1675	5.8 - 7.3	7.7
CTD 10	1440 - 1640	5.9 - 7.8	9.6
CTD 10B	1450 - 1650	5.7 - 7.6	8.9
CTD 11	1390 - 1590	6.2 - 7.9	9.2
CTD 12	1360 - 1560	6.3 - 8.4	9.8
SCIMP 2	1370 - 1570	6.3 - 8.2	9.3

The SCIMP temperature profile was broken down into 4 pieces each 50 meters in length, while the 5 CTD stations were each considered as one series 200 meters long. Each piece was then prewhitened by first differences and the Fourier transform was taken using the Fast Fourier Transform technique. After recoloring, the autospectra were computed. The 4 spectra from the SCIMP data were ensemble averaged and then averaged across five bands before plotting. The 5 CTD spectra were ensemble averaged but not band averaged at low wave number. The equivalent number of degrees of freedom are 40 for the SCIMP spectrum and 10 for the CTD, but the resolution in the CTD spectrum is 4 times greater.

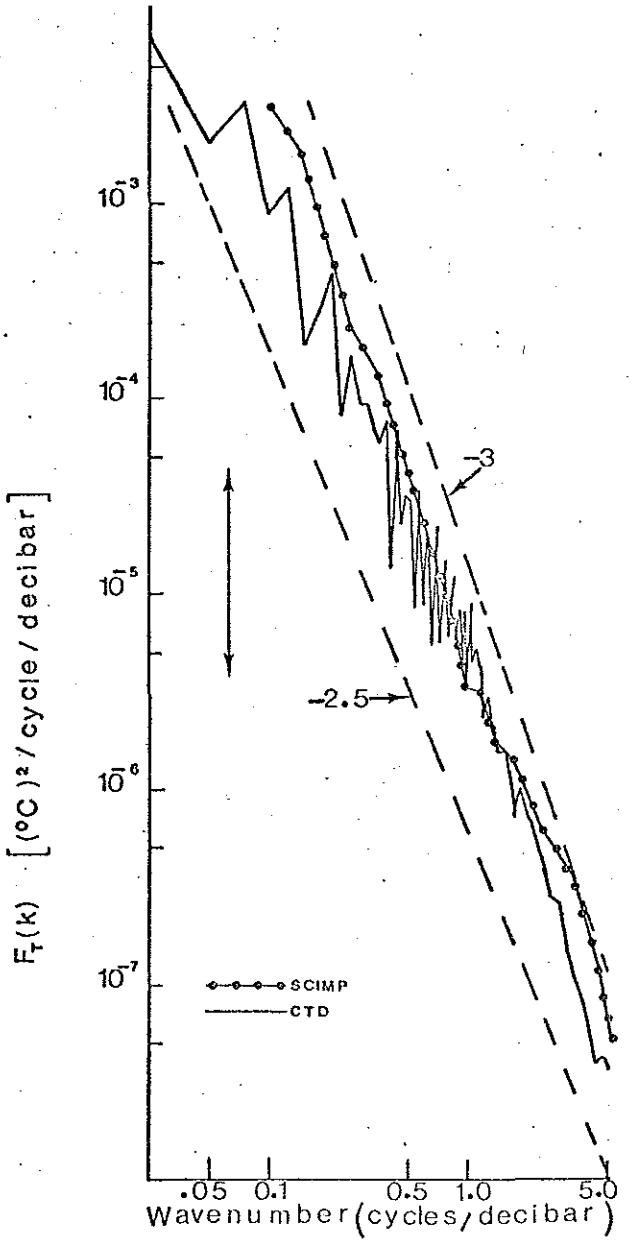

FIGURE 3.17 Autospectra of vertical temperature distribution through stepped structure from SCIMP and from a CTD on a cable. The CTD spectrum is an ensemble average of 5 lowerings. The dashed lines show slopes of -2.5 and -3. The spectrum from SCIMP is above the other at low and high wavenumber but nearly the same at the middle of the band. The 90% confidence limits for the CTD are indicated with a bar.

Figure 3.17 is a comparison of the two temperature spectra. Two reference lines with slopes -2.5 and -3.0 are also shown. The two spectra appear to be identical in the band between 0.5 - 2.0 cycles/m, but the spectrum from SCIMP has a higher level above and below this band. The lower power in the CTD at high wave number may be due to the sorting and averaging procedure used in preprocessing the data. Since SCIMP data is not subjected to this sorting, it retains its power at high wave number. The difference in power at low wave number is more difficult to justify. It seems likely that the SCIMP record is more energetic because the temperature profile itself has more variance at low wave number than the mean of the 5 CTD lowerings, and the difference is variability in the ocean. To see if this is the case, the individual spectra that make up the composite CTD spectrum are examined. Figure 3.18 shows the five individual CTD spectra and the SCIMP 2 spectrum in the low wavenumber band. Each of the CTD spectra has been averaged over five adjacent frequency bands in the plot as has the SCIMP data. The plot shows considerable variability among the CTD spectra but all are below the spectrum from SCIMP throughout the band. Hence the higher level for the temperature spectrum from SCIMP in the band 0.02 - 0.5 cycles/m cannot be justified by secular changes in the ocean.

To summarize the results thus far, power spectra of the vertical profile of temperature in a region where the profile is stepped have been computed for two CTD's. The one CTD is lowered on a cable from a ship and the other is on a freely sinking platform, SCIMP. In the band of vertical wave numbers between 0.05 and 5 cycles/m both spectra

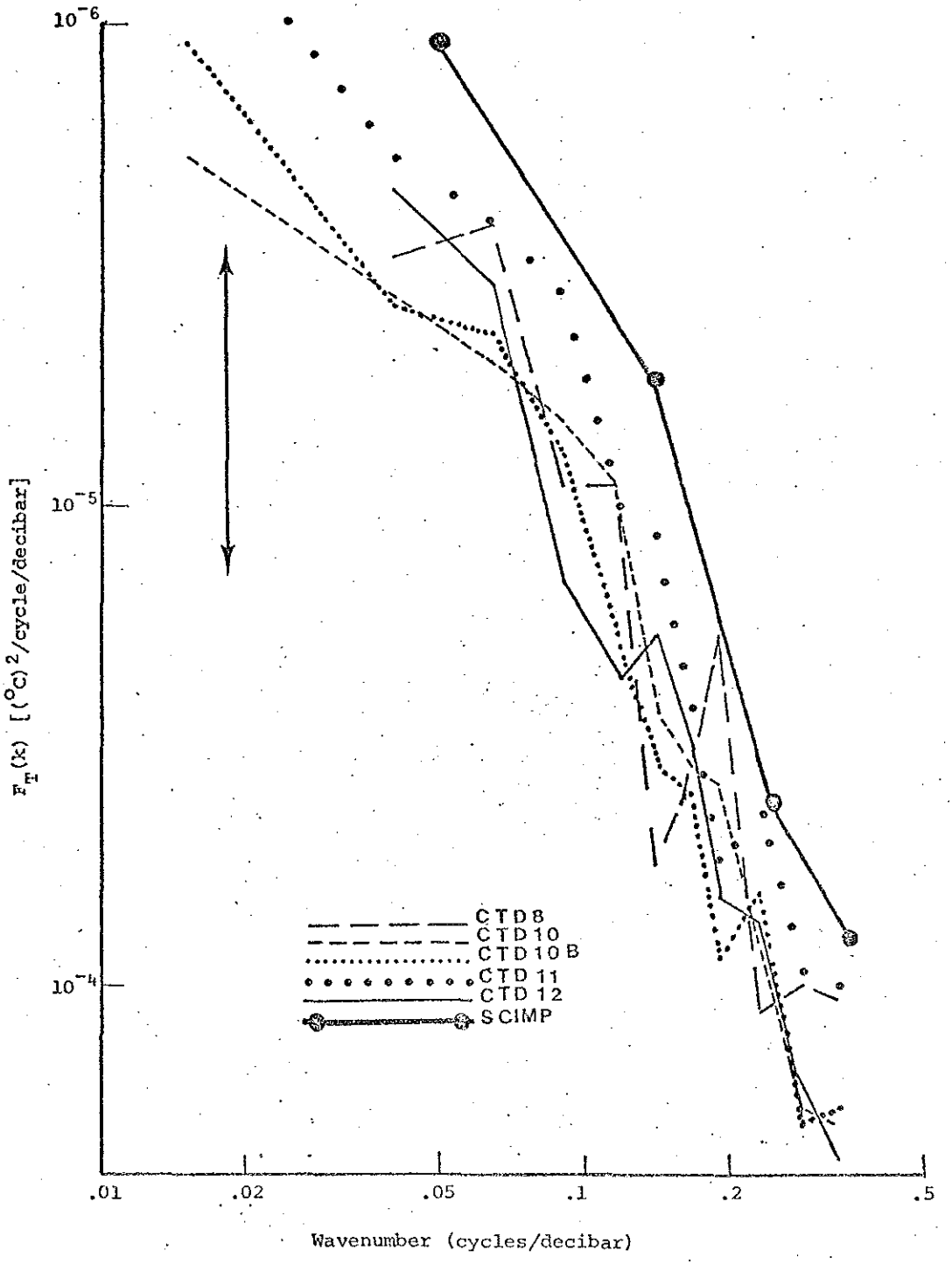

FIGURE 3.18 Comparison of individual CTD autospectra of vertical temperature with SCIMP in low wavenumber band. The spectrum from SCIMP is above the CTD's throughout the band. The bar indicates 90% confidence limits for the CTD.

have a slope in the range -2.5 to -3.0. Near the middle of the wave number band covered the two spectra agree in level, but the spectrum from SCIMP rises above at the extremes. At the high wave number end the loss of variance for the cable lowered CTD may be due to the averaging used to remove ship motions. The difference in level at low wave number is unexplained.

To compare the present results to those of Hayes et al. and the Garrett and Munk model, the displacement spectra must be calculated. The data from the cable lowered CTD is used for the comparison rather than the SCIMP data because it more nearly duplicates the instrument used in the other study. In computing the displacement spectra the processing is identical to that described above for the temperature spectra, but before the spectra are averaged each individual temperature spectrum is normalized with the square of the mean potential temperature gradient as shown in Equation (3.8). The resultant spectrum is plotted in Figure 3.19 along with the displacement spectra from Hayes et al. The level of the spectra from the steps is higher than all of the others by a factor that ranges from 2-10 except at high wave numbers where the spectra of Hayes et al. are dominated by noise. If the further normalization, (3.10), is employed the results remain the same. Figure 3.20 shows the normalized displacement spectra from the steps as well as from Hayes et al. The spectral level from the steps in the Mediterranean Outflow is generally higher than the others by as much as an order of magnitude whenever the spectra are not dominated by noise.

One of the outstanding features of the Garrett and Munk model spectrum is its apparent universality. Sets of measurements that do not fit the model seem to be rare and when they are found they should be carefully considered. The results described above are a case where the finestructure is not a direct consequence of internal waves. The finestructure here is due to turbulence which in turn is a result of salt finger convection, and it would be useful to identify the characteristic features of such finestructure.

Internal waves are not generally considered to be turbulent even though they are random flows. An essential characteristic that they lack is dissipation of kinetic energy at high wave number which is fed by a continuous distribution energy at lower wave number. Internal waves may break and form turbulence but this is an intermittent process and does not conform to the accepted picture of homogeneous turbulence. In the latter case there are theoretical results available which may be useful in interpreting the spectra from the steps even though they are not applicable to internal waves.

When the turbulence is homogeneous and the Reynolds Number is high enough, the universal equilibrium theory of turbulence due to Kolmogorov is applicable. This theory states that all dissipation in such a flow takes place at high wave number by molecular viscosity at a rate which is determined by the low wave number, energy containing eddies in the flow. Somewhere between these two extremes is a wave number band where the flow is isotropic and the spectrum is fully described by the amount of energy that is continually passed to higher wave numbers. This band is called the inertial subrange and the slope

of its kinetic energy density spectrum is -5/3. The essential characteristic for existance of the inertial subrange is high enough Reynolds Number to separate the low energy containing wave numbers from the high wave numbers where dissipation takes place. Turbulence with a spectrum that appears to follow the -5/3 power law has been observed in the ocean (Grant, Stewart and Moilliet, 1962), in the laboratory (Gibson and Schwartz, 1963), and it is commonly seen in the atmosphere.

When a fluid is stratified the temperature spectra may be modified by the effects of buoyancy at low wave number and by effects resultant from non-unit Prandtl Number at high wave number. In fluids where the Prandtl Number is greater than one, such as water, the turbulent temperature fluctuations persist to high wave number than the velocity fluctuations leading to an altered form of the temperature spectrum beyond the band where the kinetic energy is dissipated by viscosity (Batchelor, 1959). However, in the present discussion, the effects of stratification at low wave number appear to be more relevant to the observed spectra. The band of wave numbers where the effects of buoyancy are significant is known as the buoyancy subrange. Physically, the stratification places a restraint on vertical motion and the larger the eddy, the greater the effect. Energy is transferred away from the turbulence as the eddies do work against the buoyancy forces, and because of this energy loss the spectrum falls off more rapidly than the rate for the inertial subrange. Lumley (1964) has derived a form for the spectrum which covers the buoyancy and inertial subranges and approaches a -3 power law at low wave numbers and

-5/3 at high wave numbers where the effects of stratification become insignificant. Figure 3.17 shows that a -3 power law is not inconsistent with the measurements of the stepped structure.

With these results, the comparison between the spectra from the stepped structure and those from Hayes et al. can be reexamined. The levels of the former spectra are clearly higher by up to an order of magnitude as shown by Figures 3.19 and 3.20. Hayes et al. also noted that the displacement spectrum from the Mediterranean water in the Sargasso Sea was a factor of two higher than those from other water masses, and they attributed this higher level of variability to horizontal advection of water with different T-S properties. In addition, temperature is no longer a good measure of density under these circumstances. In the present case the increased variability is due to turbulence which is related to salt finger convection. The spectra in all cases appear to have a slope close to the -2.5 power law suggested by Garrett and Munk, but it is difficult to distinguish between a -2.5 power law and a -3, particularly when the number of degrees of freedom is relatively small. There is even some ambiguity about the difference between internal waves and turbulence influenced by buoyancy which is not yet resolved. But in spite of these difficulties, the important result here is that the temperature profiles made with a CTD in the stepped structure of the Mediterranean Outflow, when interpreted as normalized displacement spectra, have a level of variability in the finestructure band which is up to an order of magnitude greater than the model spectrum proposed by Garrett and Munk.

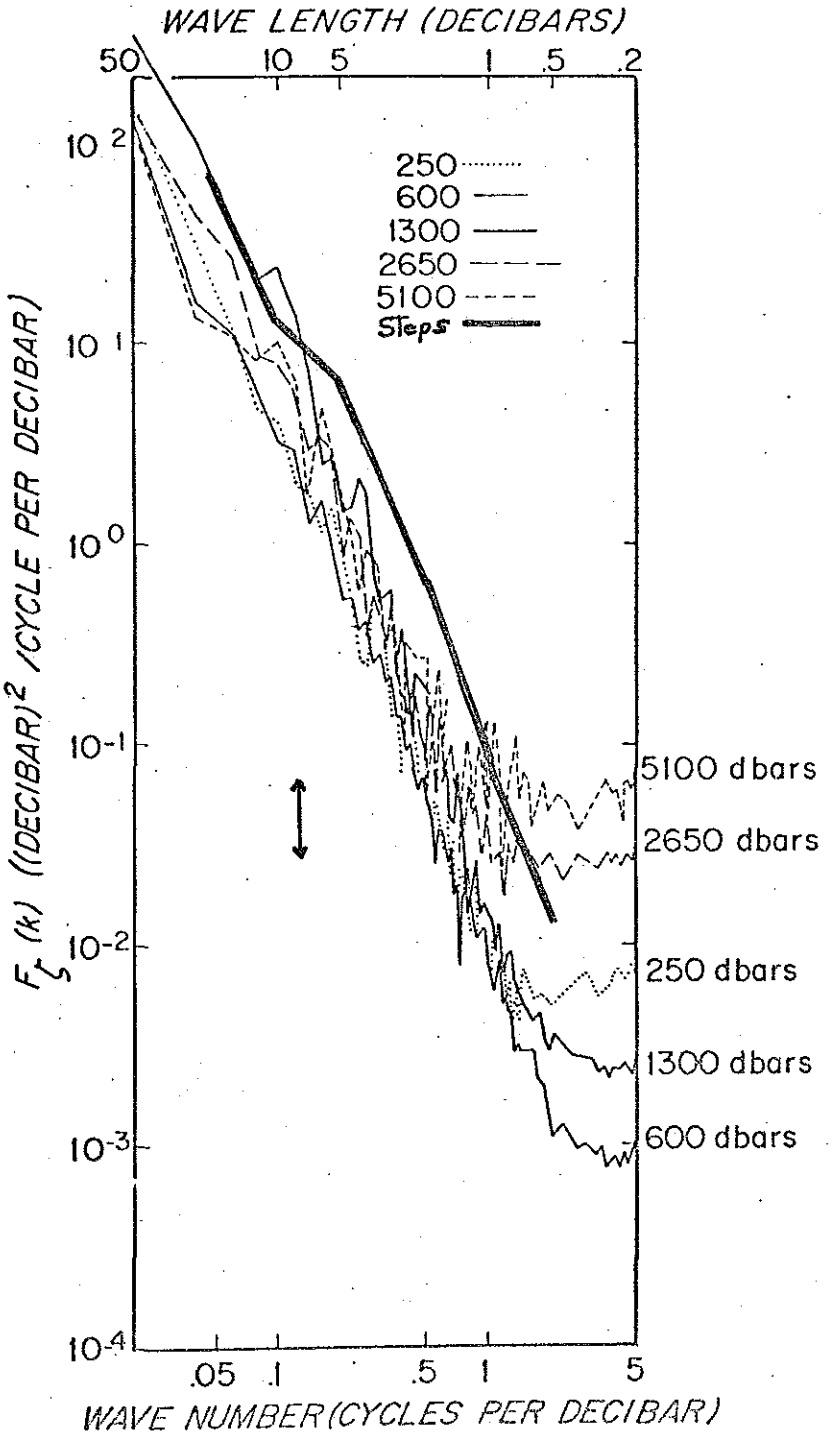

FIGURE 3.19 Vertical displacement spectra for stepped structure compared to various depths in the Sargasso Sea (Hayes et al., 1975). The spectrum from the steps has a higher level throughout except for very low wavenumber in the Mediterranean Water (1300 dbar) and for very high wavenumber where the spectra are dominated by noise. The bar indicates 90% confidence limits.

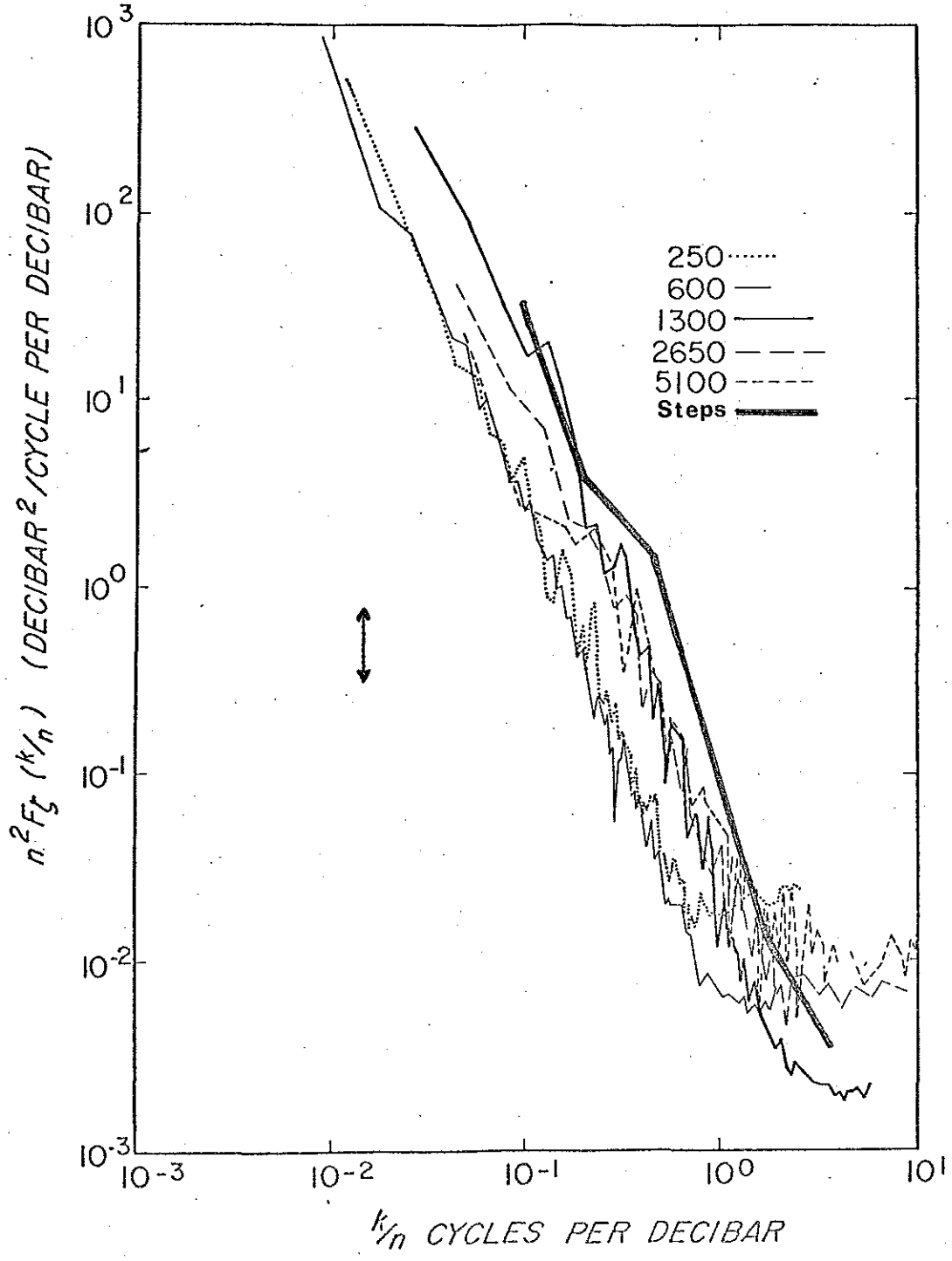

FIGURE 3.20 Normalized displacement spectra assuming Garrett and Munk 1975 model spectrum. The normalized spectra are essentially the same as the unnormalized displacement spectra in 3.19. The bar indicates 90% confidence limits.

On the basis of the above discussion, the temperature data from SCIMP seem preferable to those from the cable lowered CTD for examining the behavior at high wave number. It is particularly interesting to see what, if any, difference can be found between the temperature spectrum from the stepped structure and another where the temperature profile is relatively featureless. Further, is there evidence of separate wave number bands which are 1) affected by buoyancy, 2) inertial and homogeneous, or 3) indicative of dissipation?

From theoretical work on turbulence (Batchelor, 1959, and Lumley, 1964), there are several results which may be applicable here. As stated above, the temperature spectrum in the inertial subrange (if it exists) is characterized by a slope of -5/3, and below this wave number band the flow may be affected by buoyancy forces. The wave number, k_B, at which the flow is affected by buoyancy forces depends on the energy in the flow, ϵ_o, and the stratification which is parameterized by the stability, N^2. Dimensionally, these must be related,

$$k_B \cong \left(N^3/\epsilon_o\right)^{1/2} \tag{3.11}$$

The temperature spectrum below this wave number is characterized by a slope of -3. At the high wave number end of the inertial band the turbulent fluctuations in the velocity field are dissipated at a lower wave number than the temperature fluctuations. This is because the molecular diffusivity for momentum is larger than that for heat ($Pr > 1$) in water, hence the velocity fluctuations are dampened more efficiently. The thermal microstructure persists to higher wave number, but the char-

acter of the fluctuations is changed because the temperature field is no longer distorted by turbulent velocity fluctuations. The wave number at which viscous dissipation takes place is approximately

$$k_v \cong \left(\epsilon/\nu^3\right)^{1/4} \tag{3.12}$$

while the thermal microstructure persists to higher wave number of order

$$k_T \cong \left(\epsilon/\chi_T\right)^{1/4} \tag{3.13}$$

where ϵ is the rate of energy dissipation, ν is the kinematic viscosity, and χ_T is the thermal diffusivity. For the wave number band between these two, Batchelor has derived a temperature spectrum with a slope of -1.

To test these arguments and the Garrett and Munk model for internal waves, temperature spectra from SCIMP are plotted for two selected profiles in Figure 3.21. These spectra are temperature gradient spectra in contrast to the temperature spectra in Figures 3.17 and 3.18. To transform the temperature spectrum to the temperature gradient spectrum, each band is multiplied by k^2, where k is the local wave number. As a result of this transformation, slopes of -3, -5/3, and -1 in the temperature spectrum relatively become -1, +1/3, and +1 in the temperature gradient spectrum. This transformation has been employed here because it is difficult to determine the slope of a spectrum well when it is steep and also because the level

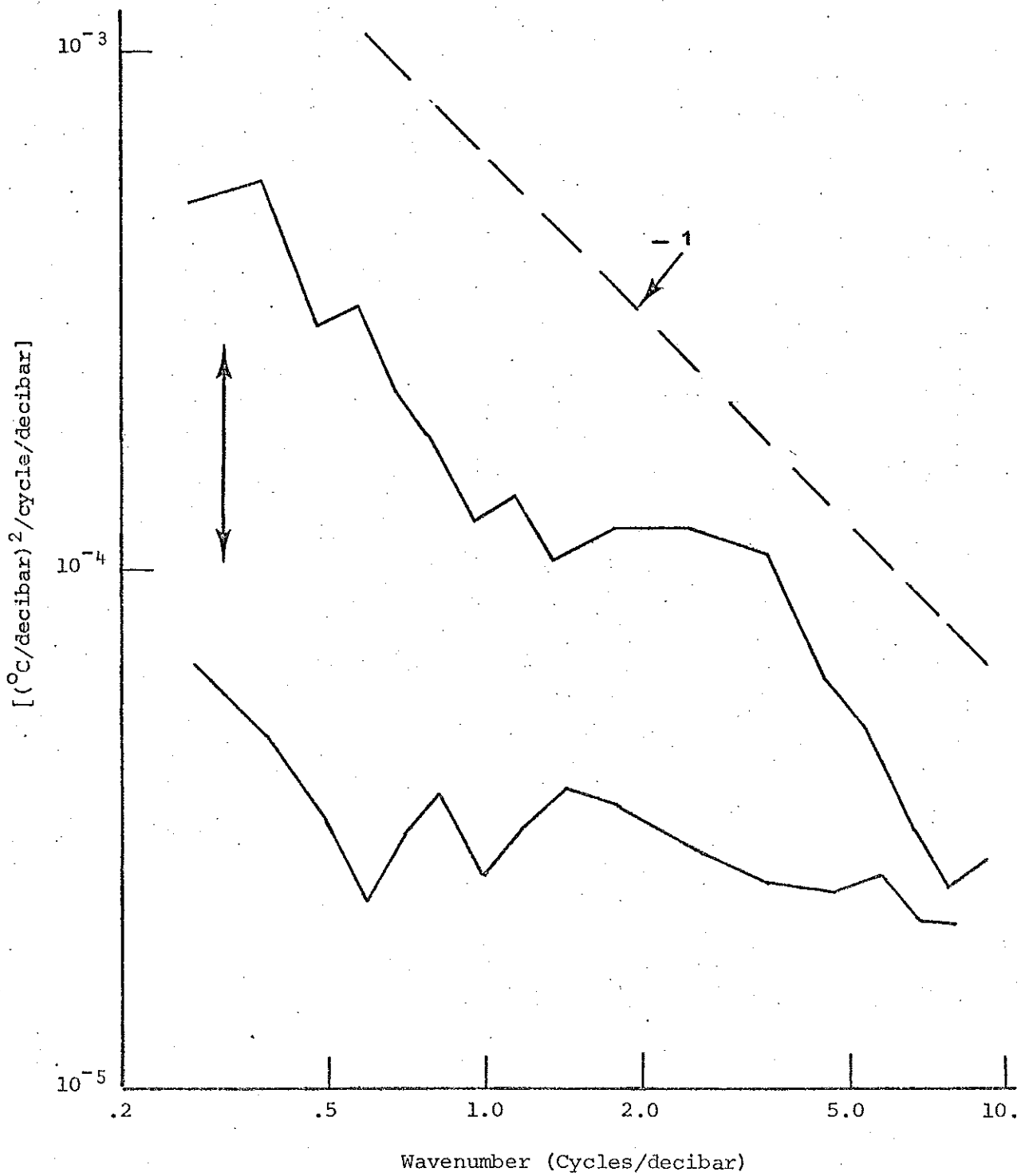

FIGURE 3.21 Temperature gradient spectra from SCIMP. The upper solid line is from the steps measured on SCIMP 2; the lower is from a featureless portion of SCIMP 5. The dashed line has a slope of -1. The 90% confidence limits are indicated with a bar.

of the gradient spectrum is proportional to the dissipation of temperature fluctuations.

The upper curve in Figure 3.21 is the gradient spectrum from SCIMP 2 in the stepped structure and is derived from the same data as the temperature spectrum in Figure 3.17. The lower curve is calculated from a section of the profile from SCIMP 5 where there was relatively little finestructure and no regularly spaced steps in temperature. The shadowgraphs from this region also show a relatively low level of activity. The two spectra are clearly different, both in shape and level, but they approach each other at high wave number where the spectrum is determined by the response of the platinum thermometer. Neither spectrum has a significant band with positive slope, though both have portions where the spectrum is nearly flat. This suggests that the inertial subrange does not exist in these data or it is outside the bandwidth of instrumentation. Likewise, the dissipation range, which must exist if the flow is turbulent, must lie at a wave number beyond the resolution of CTD. The images on the shadowgraphs from the steps in SCIMP 2 suggest that there are fluctuations in index of refraction at higher wave numbers, and the dissipation of temperature fluctuations may also be there.

The temperature gradient spectrum from the quiet region is nearly flat throughout with a mean slope between zero and -0.5, while the gradient spectrum from the steps has a mean slope near -1 with some sections steeper and a band from 1 to 4 cycles/meter where it is flat. The interpretation suggested here is that the spectrum from the quiet region is characteristic of regions where there is no turbulence, but

there may be some distortion of the temperature field by internal wave motions. The level of the spectrum is low and the slope is somewhere between the -0.5 measured by Hayes et al. and zero which was predicted by Phillips (1971). By contrast the gradient spectrum from the steps is much more energetic at low wave number where the layer interface structure itself dominates the spectrum and falls off in a way consistent with turbulence modified by buoyancy forces. At a higher wave number, of order a few cycles/meter, the vertical length scale of the salt fingers introduces additional variability into the temperature distribution resulting in a flattening of the spectrum in this band. Identifying this wave number as $k^*=2$ cycles/m, then the equivalent vertical length scale, h, is

$$h \cong \frac{1}{2\pi k^*} \cong 0.07\ m \qquad (3.14)$$

which is in fair agreement with the vertical length scale implied on the shadowgraphs and derived in Section 2.1. At higher wave number the spectrum again falls off at a rate close to -1, which is consistent with turbulence affected by buoyancy.

3.1.6 Intrusions

Regularly spaced steps in temperature and salinity are such an unexpected feature of ocean stratification that they justly deserve an explanation. The previous section has been an attempt to relate this structure to the dynamics of salt finger convection. A critical parameter in the salt finger model is the strength of the mean salinity gradient relative to the temperature gradient, and large values in the

proper sense leads to convection. When there is a relatively deep region where a large destabilizing salinity gradient is maintained, breakdown into convecting layers is possible and has been seen in the laboratory (Stern and Turner, 1969) and in the results described above. When the salinity gradient is strong but not sustained over a deep region, theoretical calculations suggest that salt fingers should exist and shadowgraphs often confirm their presence in such situations. In this case there may be a single sharp interface with salt fingers and poorly developed convecting layers above and below. Such situations may occur when a water mass with a T-S characteristic is advected laterally into new position where it appears as an intrusion. Then large differences in temperature and salinity may be possible both above and below such an intrusion, while density differences may be small.

In one sense the Mediterranean Water itself represents an intrusion of high salinity water from the Mediterranean Sea into the North Atlantic, but here thinner layers are considered with thicknesses from a few tens of meters down to less than a meter. These intrusions occur within the body of the Mediterranean influenced water, and the distribution is such that this water mass may be thought of as an ensemble of these smaller intrusions. That is, the water column in the region of the Mediterranean Outflow between about 600 m and 1600 m is composed of layers with various thicknesses and T-S characteristics. Figure 3.22 is a plot of temperature vs. salinity (a T-S plot) from SCIMP 1, which illustrates the interleaving of water masses. A single water mass is represented as points in a

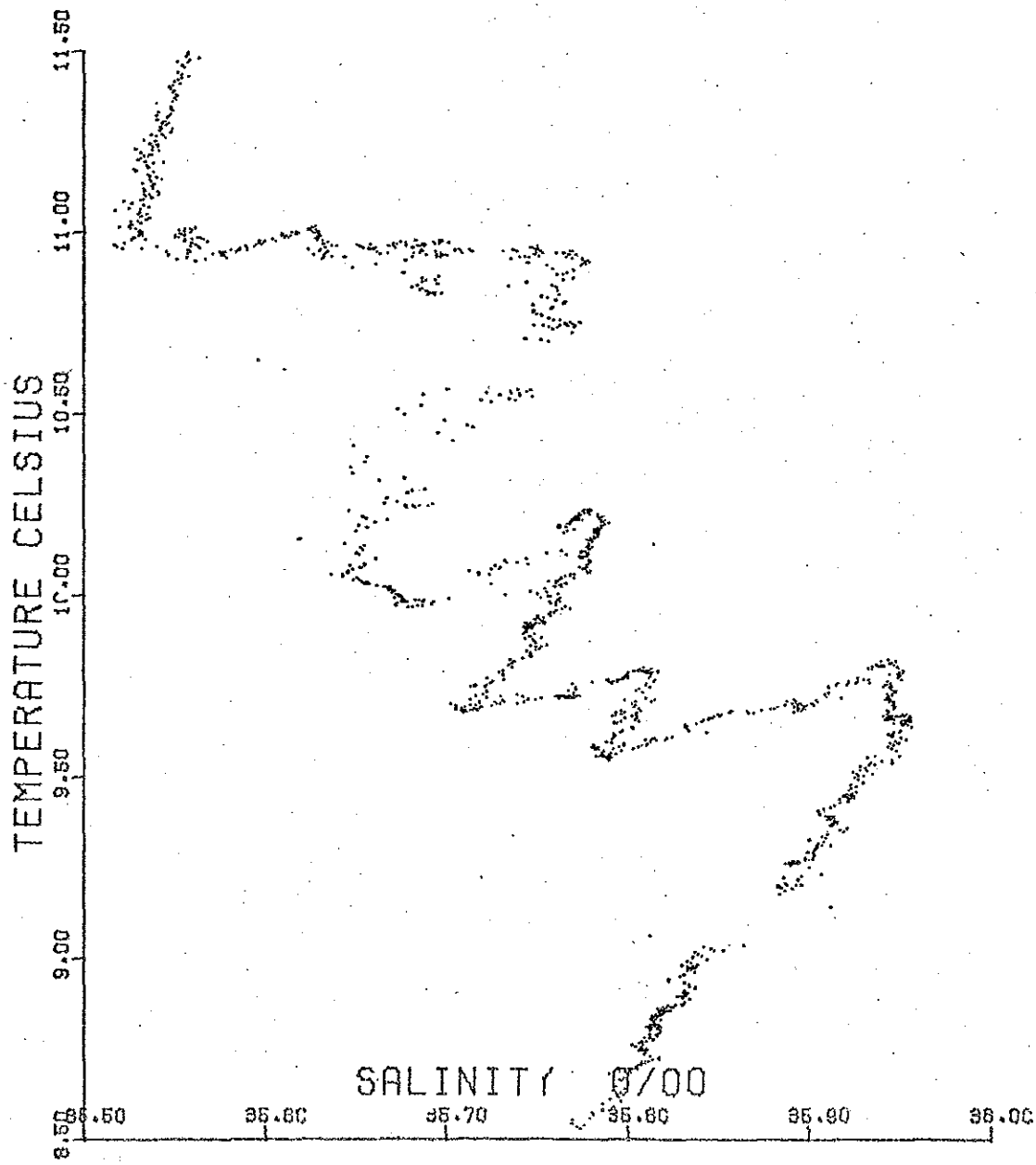

FIGURE 3.22 T-S plot for SCIMP 1 covering the depth interval 500-1300 m. The jagged appearance of the curve shows that the water column at this level is formed by a complex interleaving of layers with different T-S characteristics.

straight line of such a plot and the saw-toothed appearance of Figure 3.22 shows that there are many water masses or intrusions present. In this section several intrusions are examined in detail with particular attention to features which may show how they interact with the environment. This includes, of course, shadowgraphs of salt fingers and turbulence.

Figure 3.23 shows a part of the profile from SCIMP 1 where there is a prominent intrusion of warm salty water at a pressure of 1450 decibars, well below the salinity maximum. There is also a smaller intrusion about 40 decibars above. Defining the thickness of such a warm intrusion as the distance from the local temperature minimum on the top to the point where the temperature drops again to that value on the underside, this layer is 29 m thick. The core of the intrusion is nearly homogeneous in temperature salinity and density except for a warmer, saltier layer 5 m thick at the top. In addition to temperature and salinity, a density referenced to a nearby level is shown in Figure 3.23. The reasons for using this function rather than the more conventional surface reference (σ_θ) is explained in Appendix C. The salinity and density are fairly noisy here because the conductivity cell was apparently responding slowly compared to the platinum thermometer. The magnitude of the temperature and salinity inversions on the upper side of the layer are respectively 0.17°C and 0.04°/oo, while 0.05°C and 0.01°/oo of this is contributed by the 5 m layer at the top. Estimates of density differences where the temperature is changing rapidly are tenuous, but there appears to be an increase of 2 ppm from the temperature minimum above the intrusion to the local temperature

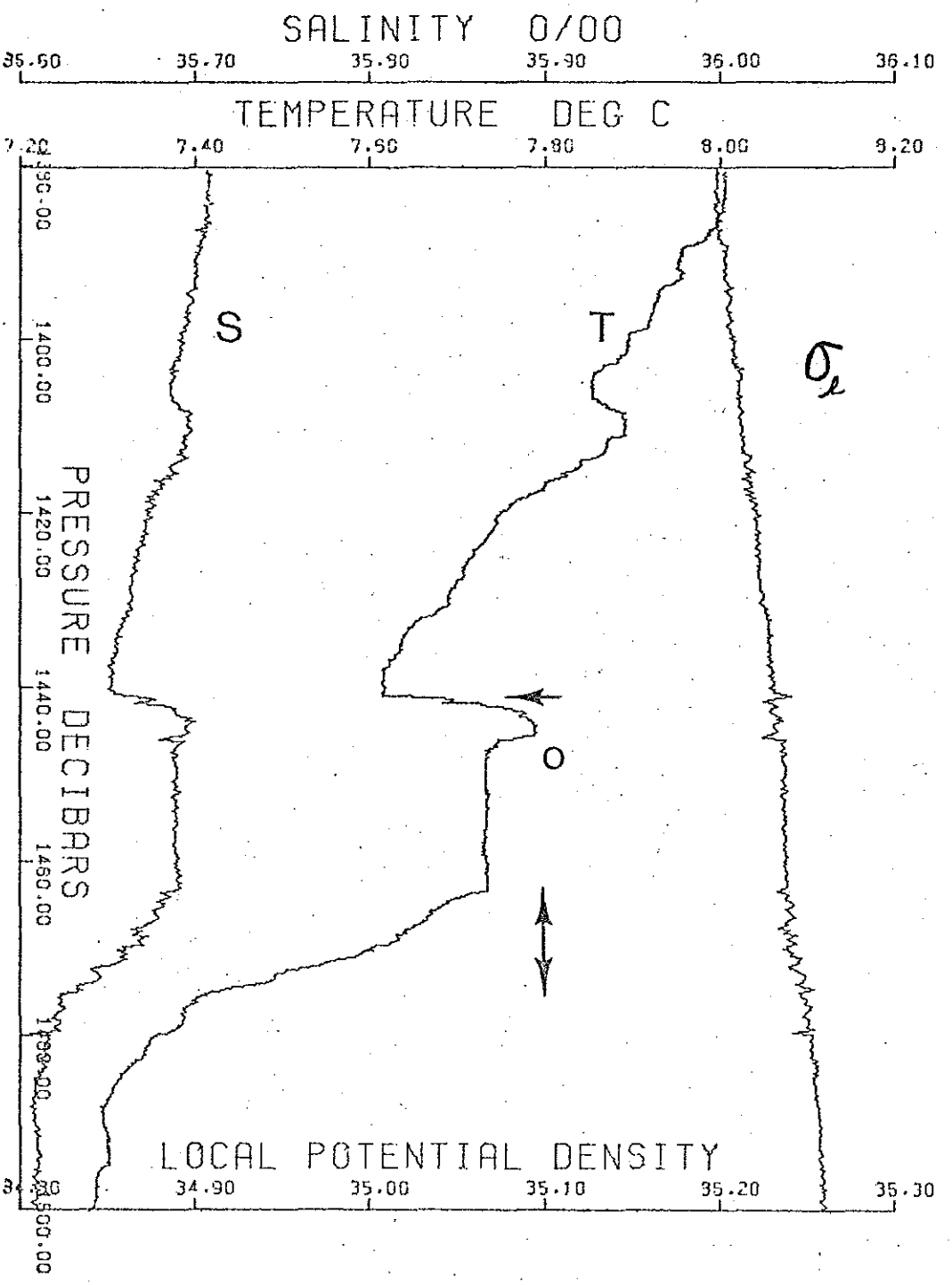

FIGURE 3.23 Warm, salty intrusion from SCIMP 1. On the shadowgraphs there are bands at the top of this intrusion and a long sequence of bands and turbulence on the underside. At the point marked with an O, there are no images even though the conditions are correct for salt fingers.

maximum, and a further increase of about 5 ppm from the temperature maximum to the homogeneous core. Density cannot be resolved below the core with any confidence until well below the intrusion at a pressure of 1477 decibars where the temperature flattens out somewhat. The density there indicates that the underside of the intrusion has a density stratification approximately the same as the mean for that depth, 11 ppm in 14 m or N = 1.6 cycles/hr. In summary, the density increase is small at the top of the intrusion, and density gradient is near average on the underside. There is a relatively large density difference at the bottom of a smaller warm layer near the top of the main body of the intrusion.

The shadowgraphs show that there are several optical events associated with the intrusion, and the locations of these are also indicated in Figure 3.23. There is strong vertically banded structure at the top interface where salt fingers are not possible and also some weaker lines near the bottom of this interface. These bands may be related to the diffusive mode of double diffusive convection, which is permissible under the conditions of this interface. Production of turbulence by shear is also possible at the interface but does not appear to be favored there because of the small density contrast. If either of these mechanisms has produced the small scale fluctuations in index of refraction seen by the OSFD, then it is not clear why there should be a vertical alignment to the structure. This is an observation which cannot be explained completely satisfactorily. The interface at the bottom of the intrusion has structure in the shadowgraphs nearly continually from just below the bottom of the core to

near the flat spot in the temperature profile at 1477 decibars. The structure consists of vertical lines and random lines interspersed and varying in contrast and would appear to be a turbulent interface 10 m thick. Temperature and salinity gradients are proper for salt finger convection and the vertical bands in the films suggest that there may be several sets present within this 10 m interface. There are also small inversions in temperature similar to those seen on some of the interfaces with strong salt fingers between convecting layers above. In contrast to this, the interface at 1445 decibars at the top of the homogeneous core has no detectable images on the shadowgraphs even though the gradients have the proper sign for salt fingers. However, the salinity difference here is relatively small, $.01^{o}/oo$, and the density difference correspondingly large. These two factors respectively tend to discourage salt finger convection and damp possible turbulent fluctuations. As in the earlier results the salinity difference seems to be a more important parameter than the gradient for breakdown. Again, little can be said about the level of fluctuations in the homogeneous core of the intrusion, because there can be no fluctuations in index of refraction in a layer that is homogeneous in temperature and salinity even if there are turbulent velocities present. However, there does appear to be a thin layer (3 m) at the bottom of the core where the temperature is more nearly constant than above. This may be a layer that is well mixed by salt finger convection below or it may be a result of the strong nearby density gradient.

SCIMP normally records CTD data when ascending, though at that time signals are somewhat degraded because the sensors are in the wake of the upper part of the vehicle. Figure 3.24 is the profile of an intrusion that was observed by SCIMP while ascending on the same dive as it measured the intrusion in figure 3.23. Although similar in many respects, the two are sufficiently different that some doubt exists as to whether they are indeed the same layer. Some properties of the two are summarized below.

	P (db)	T ^{o}C	C mmho/cm	thickness m	θ ^{o}C	S $^{o}/_{oo}$	σ_T
descending	1452	7.735	37.224	29	7.581	35.671	27.860
ascending	1366	7.723	37.194	18	7.579	35.691	27.877

Because of horizontal currents, SCIMP will not rise through the same column of water that it descended through and here the time separating the two measurements is 1.5 hr. First note that the layer is 86 m shallower on ascending. Erratic performance by the pressure sensor makes this measurement suspect (see Appendix A), but it appeared to be working properly at the time of both measurements being discussed. Such a vertical excursion due to internal wave motion seems large, but not impossible. This possibility is given support by the temperature and potential temperature measurements. Since internal wave motions are adiabatic, potential temperature should be conserved even though local temperature may change. A difference in potential temperature of $0.002^{o}C$ is close to the limits of accuracy of the system. However, the conductivity difference and hence the salinity and sigma-t differences are not consistent with an adiabatic expansion, where salt is conserved. The difference in sigma-t in the two measurements is par-

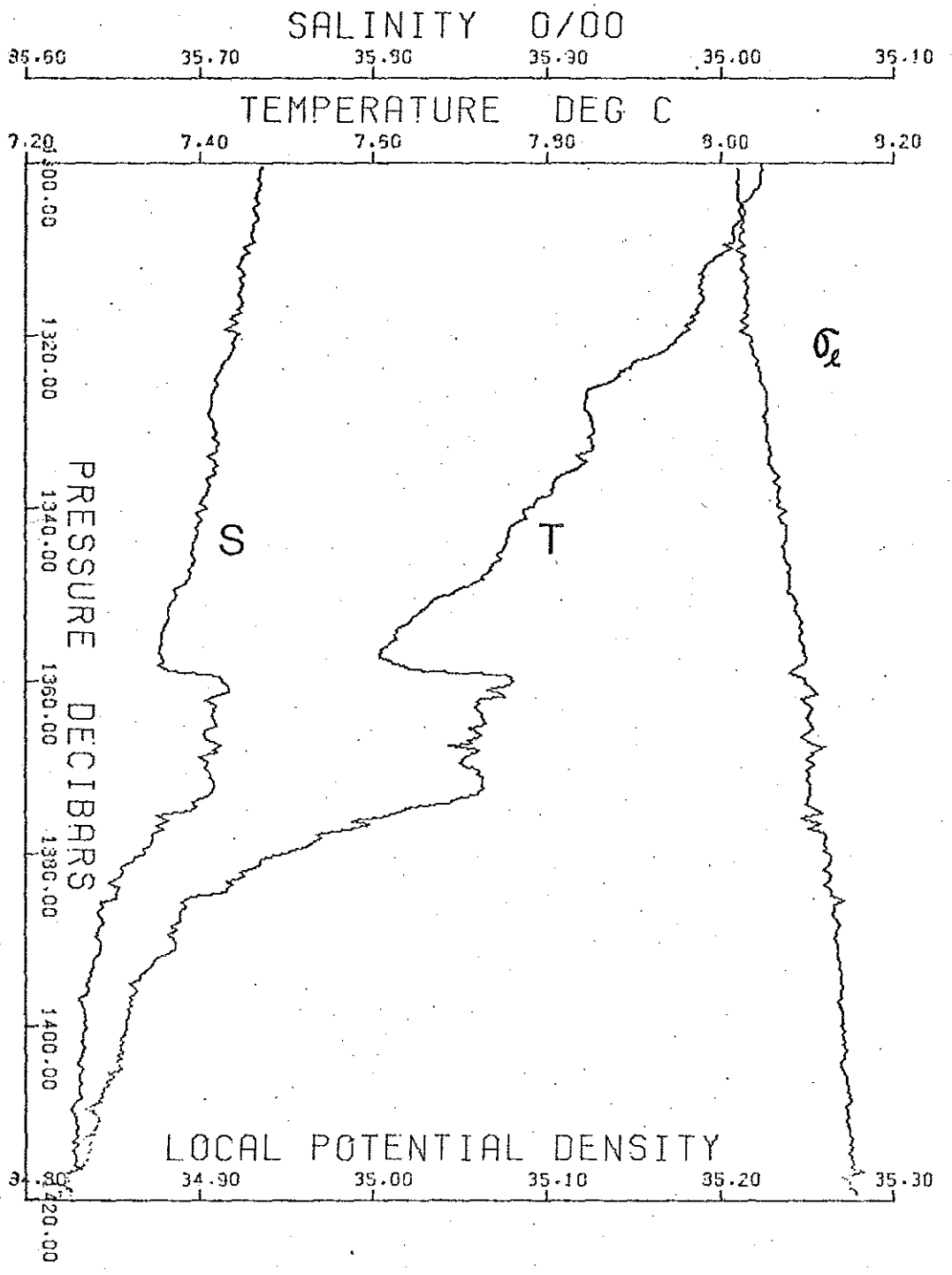

FIGURE 3.24 Warm, salty intrusion from the ascending portion of SCIMP 1. Although similar in many respects to the intrusion in Figure 3.23, there are several significant differences.

ticularly troubling because the denser water appears to be shallower, implying a steep slope in isopycnal surfaces. In view of this last inconsistency, there is a strong likelihood of a bad pressure measurement. Even so, there appears to be some difference in the two layers and they may be distinct. It should be noted that no similar intrusion was present on the CTD lowering taken 3 hours before SCIMP was launched, which also points to possible horizontal variability.

There are numerous other measurements of intrusions by SCIMP, and some of there are considered below to illustrate some important characteristics, particularly the appearance of turbulence relative to them. Examples are chosen from near the salinity maximum where the absolute maximum or a strong relative maximum in salinity often has strong microstructure and salinity gradients on its underside. Intrusions here are generally thought of as warm and salty in a cooler, fresher background because the source of the former is the nearby Mediterranean Sea.

Of the 6 SCIMP dives, all but one has high contrast activity on the shadowgraphs, including bands just below the deep salinity maximum, and strong secondary maxima have similar images. Similar results have been reported by Gregg (1975) where the levels of thermal microstructure and dissipation were found to be greater on the underside of saline inversions than any other location except the base of the surface mixed layer. Three events are chosen for discussion below which have high contrast sustained images on the shadowgraph films. These constitute some of the strongest activity in all the data from the cruise.

The most definitive example of salt finger images is found below the salinity maximum at a pressure of 1264 decibars on SCIMP 1. (Appendix B describes measurements of the banded structure here using a simple photodensitometer and a digital Fourier analyzer.) Figure 3.25 shows the profile from above the salinity maximum to below this interface, with temperature, salinity, and locally referenced potential density plotted. Although the images at 1264 decibars are by far the strongest, there are several other active interfaces between the salinity maximum at 1209 decibars and this interface. By comparison there is only one interface with images between the salinity maximum and the local minimum above, which occurs at a pressure of 1020 decibars, and this interface is in the middle of a sequence of steps where temperature and salinity both increase sharply with depth.

The interface at 1264 decibars is unique because of the large salinity difference, more than $0.05^{o}/oo$ in less than a few meters (salinity spiking prevents a more accurate measurement of the thickness of the salinity interface). Temperature also has a large change here of 0.29^{o} C since the interface is statically stable, though the local density change is relatively small at $0.013^{o}/oo$, and so is the Turner No., Tu = 1.3. Above the interface is an 8 m thick isothermal layer in which salinity and density increase with depth. This observation is not consistent with the usual picture of a convecting layer where the mean density is neutral or decreasing with depth. Closer inspection reveals that the strongest vertical bands are confined to a thin high gradient region which is approximately 30 cm thick and both above and below this are layers where there are many small tempera-

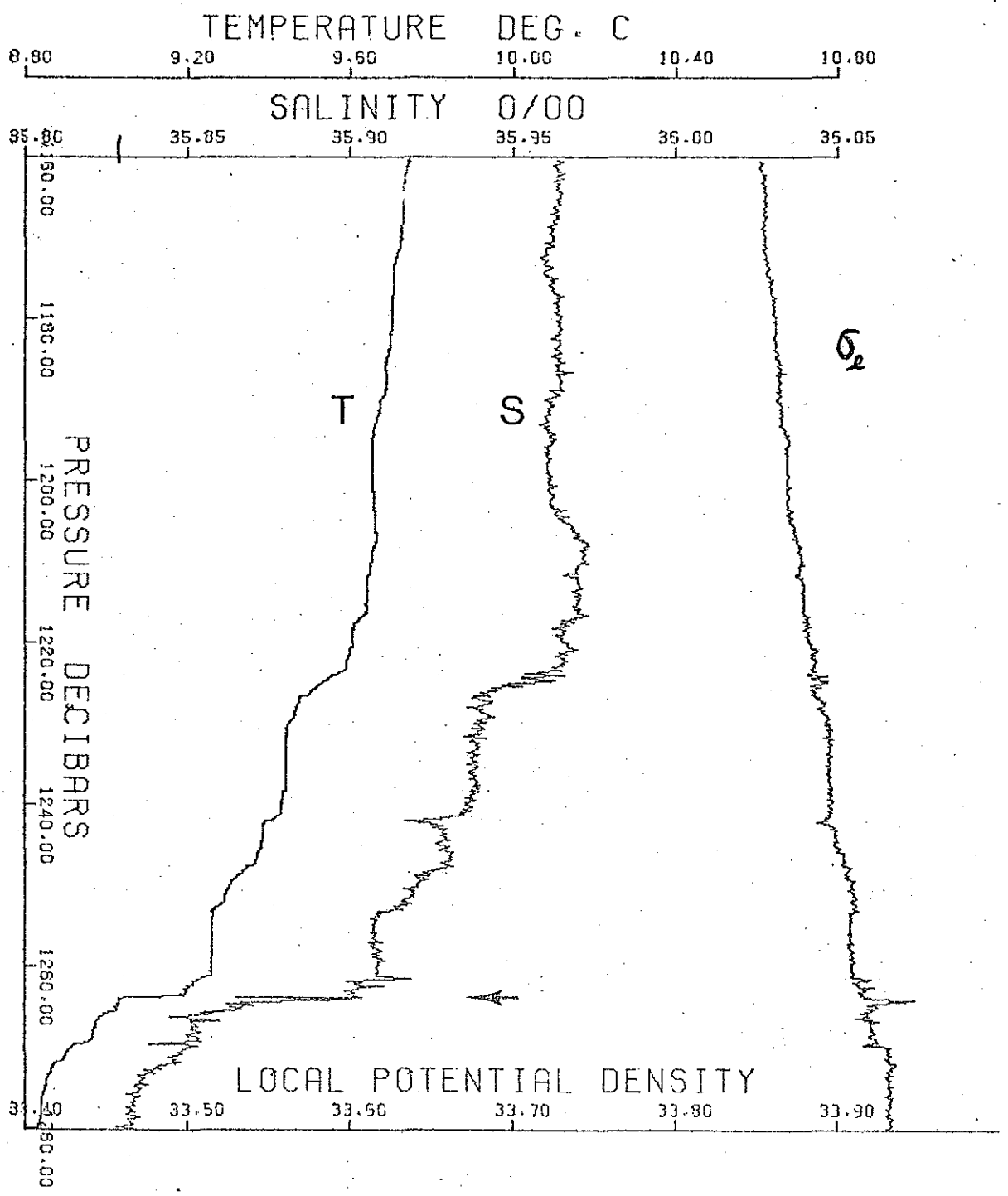

FIGURE 3.25 A section of the profile from SCIMP 1 showing the very sharp interface at 1264 db and its relation to the salinity maximum at 1209 db. The shadowgraphs from this interface have very distinct bands. The arrow is at the point where the bands are strongest.

ture inversion and turbulent images on the films. There is tenuous evidence that this upper turbulent layer is separated from the isothermal layer above by a density contrast which would isolate the latter from the convection below. In this case the isothermal layer centered at 1258 decibars may be more closely related to the interface above than the one below. There is activity on the films including vertical bands throughout the interface which extends from 1238 decibars to 1253. Another observation that is consistent with this picture is that there is no isothermal layer with a thickness of order 8 m below the interface at 1264. By the symmetry of the salt finger system, a layer mixed by salt finger convection above should be accompanied by a similar layer below. Instead there is a thin layer (approx. 1 m) with small temperature inversions and turbulent images below as well as above. The conclusion is that a relatively thin region (approx. 2.5 m) is centered on and under direct control of the salt fingering interface at 1264 m and that this region is in some ways different than those found within the stepped structure. The interface above, centered at 1248 decibars, is more like those found within the stepped structure in many ways, with all of its parameters within the range measured there and isothermal layers above and below. The interface at 1264 is extreme in its characteristic parameters and may represent a different regime of the salt finger convection. It is tempting to speculate that this very thin interface with extremely large gradients and poorly mixed layers above and below may evolve into a broader interface with homogeneous layers above and below as it runs down. This picture is entirely consistent with the data.

Naturally the original vertical temperature and salinity contrast must be set up by lateral advection of dissimilar water types, an intrinsic feature of intrusions.

Other sharp salinity interfaces below local salinity maxima also have high contrast images on the shadowgraphs associated with them. In the example just discussed, the relationship between the shadowgraphs and the profiles is very clear, with high contrast vertical banded structure coincident with large temperature gradients and turbulent structures above and below. This is consistent with theoretical models of salt fingers on an interface driving convection with an unstable buoyancy flux. In other cases the relationship between the profiles and shadowgraphs is less precise and the images themselves are more ambiguous. Some of the images appear to be periodic and have a vertical orientation, but most are not. Even though the distinctive optical signature of salt fingers is missing, these interfaces appear to be directly related to salt finger convection. Also, the similarities among these interfaces suggest that there is some generality in form and perhaps dynamics.

The two structures to be discussed below, like the previous two, have been chosen because they have sustained high contrast images on the shadowgraphs. They also have some of the largest temperature gradients measured, though these may not coincide with the images, and the interfaces are located immediately below relative salinity maxima. The first is from SCIMP 4 just below the deep salinity maximum at 1070 decibars. The second is from below a secondary maximum at 1270 decibars on SCIMP 2, and their profiles are shown respectively, in Figures 3.26

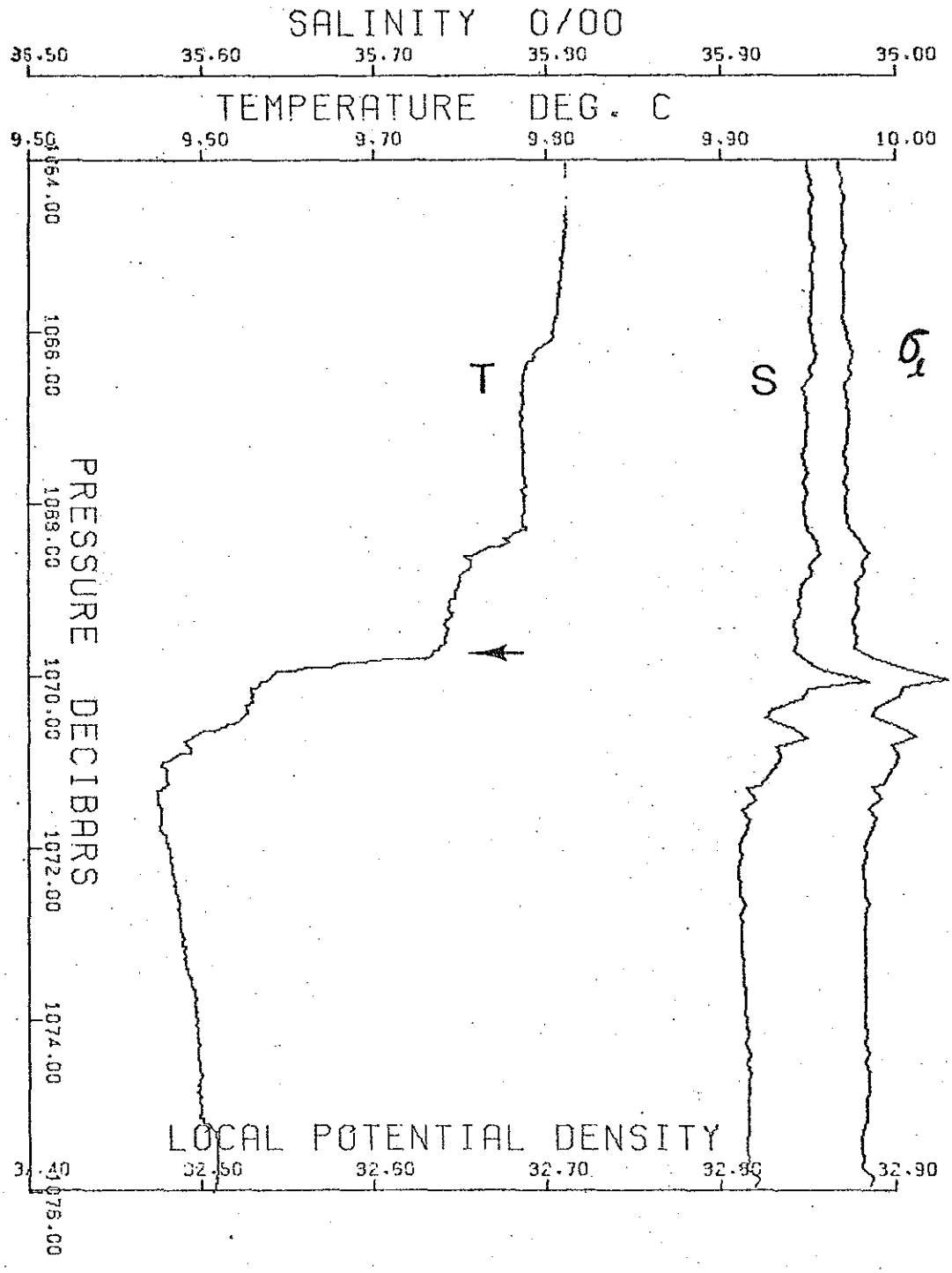

FIGURE 3.26 Interface just below deep salinity maximum from SCIMP 4. The arrow marks the point where the shadowgraph images have highest contrast.

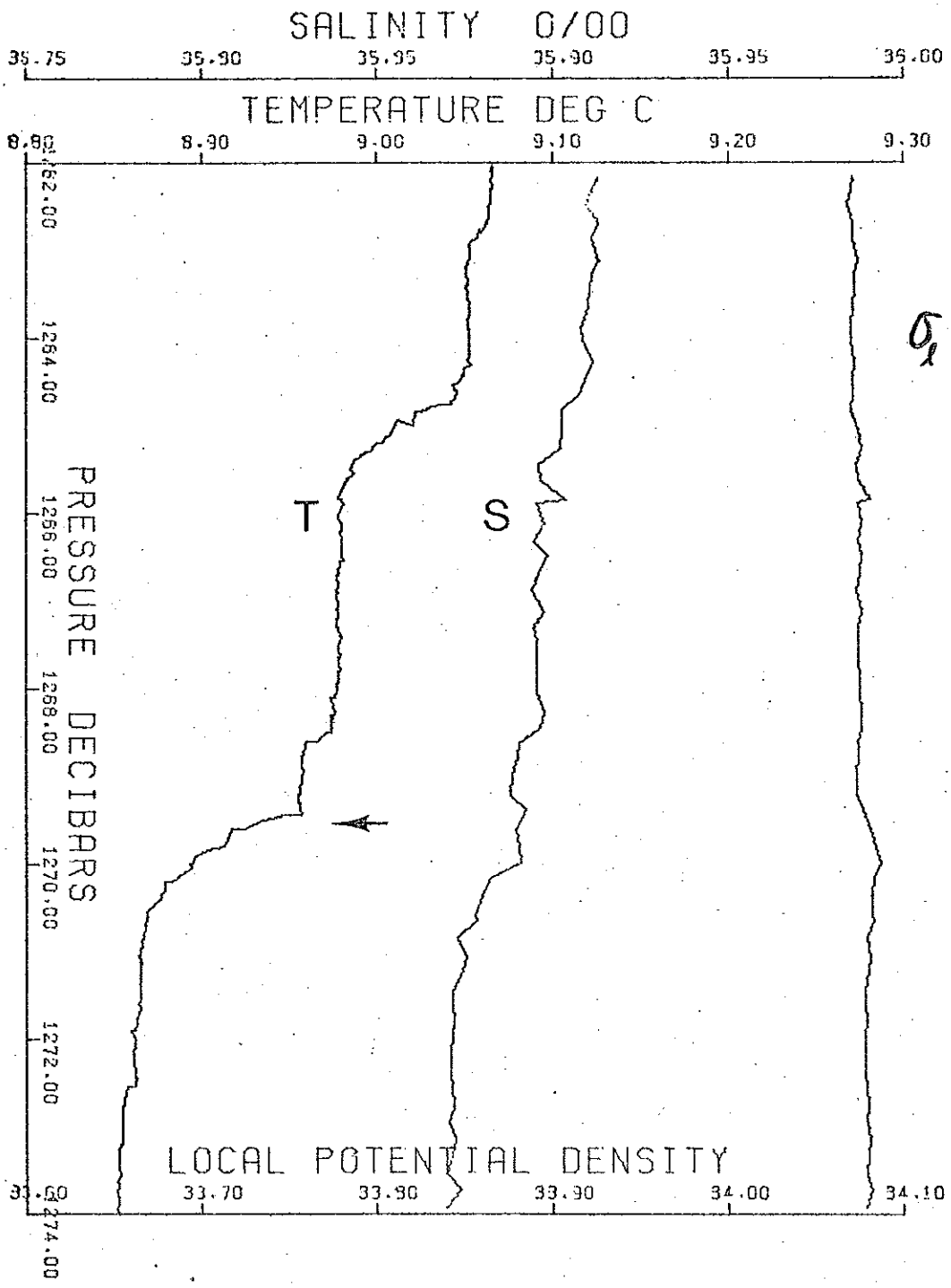

FIGURE 3.27 Profiles of temperature, salinity, and local potential density just below a secondary salinity maximum from SCIMP 2. The arrow marks the position of high contrast images in the shadowgraphs.

and 3.27. In both profiles the salinity spiking is severe so that only where the temperature is constant for about a meter can salinity and density be determined with any confidence. The regions of strong images in the shadowgraphs are also indicated on the profiles. Each of the events consists of one very sharp temperature interface 20-30 cm thick with a turbulent layer about 2 m thick below which the shadowgraph impages have particularly high contrast, weakening with distance from the interface. There are also several lesser interfaces above the strongest one before the local temperature maximum is reached in both cases. (Again it would be preferable to discuss the salinity structure rather than the temperature, but the salinity is unreliable.) Each is terminated below by rising temperature, salinity and density so that there is no chance of stepped structure development below the sharp interface.

Table 3.4 summarizes some properties of the four interfaces found below salty intrusions discussed thus far. From this it appears that low Turner Number, or a strong salinity gradient relative to the temperature gradient, is characteristic of these features. In Section 3.1.4, less than 1/5 of the total number of interfaces where the salinity decreased with depth were found to have $Tu < 1.4$. Naturally these 4 were included in this number and all were identified as being turbulent

TABLE 3.4

Properties of interfaces found on undersides of salinity maxima.

Interface Dive Pressure (decibars)	$\Delta\Theta$ ^{o}C	ΔS $^{o}/oo$	$\Delta\rho$ $^{o}/oo$	T_u
1-1264	.29	.056	.013	1.30
4-1070	.20	.038	.010	1.34
2-1270	.13	.024	.006	1.32
1-1470	.35	.064	.011	1.22

It now seems possible to explain many of the common features of these intrusions in terms of salt finger convection. But first there must be some explanation of why the intrusions appear at all. It seems very probable that the deep water which appears to be anomalous by salt in this area had its origin in the Mediterranean Sea. Depending on what its mixing and dilution history was after flowing out through the Strait of Gibraltar, this water is more or less salty for a given density.

Before leaving the Mediterranean Sea, the water has a salinity of about 38.4°/oo and a temperature of 13°C (Sverdrup et al., 1942). After crossing the sill at a depth of 320 m in the Strait of Gibraltar and reaching the open Atlantic, its salinity is much reduced. The dilution process is undoubtably very complicated due to tidal and topographic effects within the strait so that many different small water masses are produced each with a different mixing history. When a water mass has had relatively little dilution compared to other water of the same density or it has been diluted by water with a more salty characteristic, it may be a warm, salty intrusion when it appears as a layer in a profile, in the Atlantic. Alternatively, a salty layer may have taken a more direct path to the point of observation, compared to its surroundings, and the mechanisms which tend to dilute the layer may have had less time to act.

Salt fingers are one way that these salty intrusions may decay, and this mechanism can only operate on the underside of such an intrusion, where turbulence has repeatedly been observed. Although salt fingers are possible nearly any time warm salt water overlies cooler fresher water (Equation 2.34 above), the transport of both salt and

heat too depends on the salinity difference. The salt flux is

$$\beta F_S = C(\beta \Delta S)^{4/3} \tag{3.15}$$

while the ratio of fluxes is given by

$$r = \left(\frac{\beta F_S}{\alpha F_T}\right)^{-1} = f_n\left(\frac{\alpha \Delta T}{\beta \Delta S}\right) \tag{3.16}$$

where C is thought to be a slowly varying function of $\alpha\Delta T/\beta\Delta S$. The buoyancy flux, $F_B = (1-r)\beta F_S$, also depends on the salinity difference, and it is the buoyancy flux that generates the turbulence in the salt finger model. Then it is the salinity excess presented by the intrusion that provides the potential energy to drive the convection that produces the turbulence. During the process, salt falls reducing the magnitude of the salinity anomaly, which in turn reduces the fluxes. In the discussion above of the interfaces between regularly spaced steps, it was shown that salt fingers do not span the entire distance between the uniform layers and that only a fraction of the salinity difference drives the convection. The situation is similar on the undersides of intrusions where there are generally several high gradient regions within the system. In the examples the interfaces are dominated by a single gradient, but there are other weaker gradients present. In Figure 3.27 there is banded structure on the interface at 1265 m as was there on the smaller interface above the main on in Figure 3.25. Laboratory experiments by Turner and Chen (1974) have shown that a sequence of layers may be found by double diffusive convection above

and below an intrusive layer. There is some evidence for this type of behavior in these intrusions with vigorous salt finger convection below the warm, salty layer.

There is a fundamental asymmetry in the intrusive system that acts to disrupt the symmetry of the salt finger convection. This is because the upward development of layers and interfaces is terminated by the salinity maximum, while layer formation below can extend until another intrusion is encountered or the salinity differences are no longer strong enough to drive convection in layers. In the examples above, Figures 3.23-3.27, there have been only a few interfaces and the layers are not particularly well developed below the intrusions. This may be because the intrusions are relatively "young" in the sense that the salinity gradient is strong relative to the temperature gradient. Or it may be because downward development is terminated by a second intrusion below.

Preceding discussion suggests that sharp interfaces with salt fingers separated by uniform layers that are stirred by convection may be the preferred state below a salinity intrusion unless this structure is inhibited in some way. Two more observations from below relative salinity maxima are now chosen which support this view. The first of these is taken from SCIMP 1, below a relative salinity maximum, which is at 980 decibars. Figure 3.28 shows the temperature, salinity and local potential density for the underside of this inversion, and there are four interfaces separated by layers with prominent inversions. Again salinity spiking seriously degrades the quality of the salinity and density measurements. Although not as strong in con-

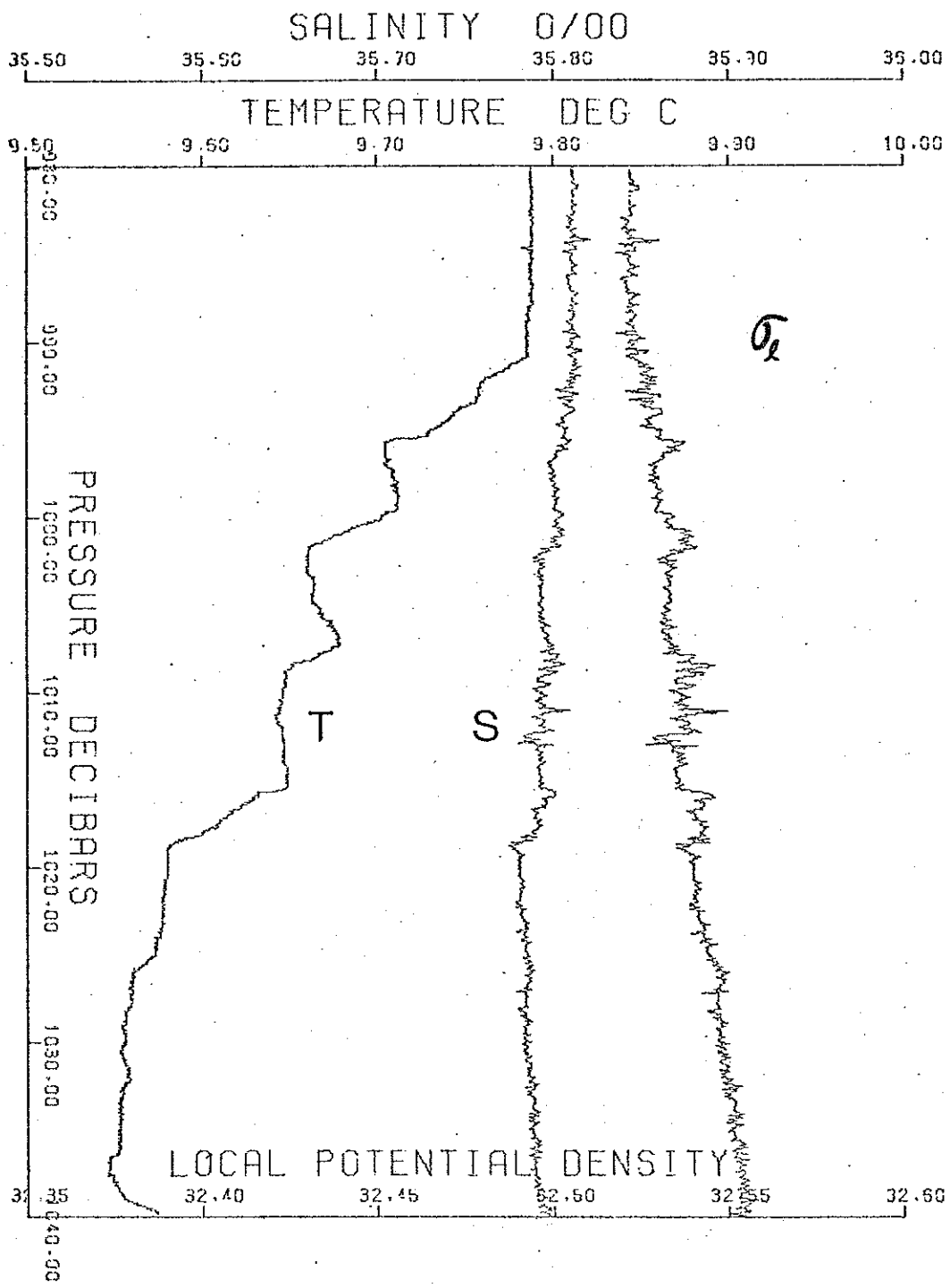

FIGURE 3.28 Series of steps below a secondary salinity maximum from SCIMP 1. At the bottom of the steps the salinity begins to increase.

trast as some of the others, there are weak to moderate contrast images on each of the interfaces and some have a banded structure to them. As before the development downward has been determined by a layer with increasing salinity, but here the layers are more clearly developed than with other intrusions. The salinity difference here is smaller both absolutely (~10 ppm/interface) and also relative to the temperature differences. In terms of Turner Number, Tu = 1.7, for this group of interfaces as compared to $Tu = 1.3$ for the earlier interfaces. The former value is close to that seen earlier where there were regularly spaced steps. The temperature inversions seem at the bottom of several of the layers are also similar to those seen within the stepped structure, but no assessment of their role dynamically can be made because of salinity spiking.

Finally, to see the distribution of properties within the layers, and possibly within the interfaces, where there is stepped structure immediately below an intrusion, a section of the profile from SCIMP 3 is chosen. The response of the conductivity cell in SCIMP 3 appears to be faster than the thermometer, but only by a small amount so that the features in salinity and density are fairly well represented. Although this is not the best example of regularly stepped structure, there is a sequence of layers and there are some relatively strong banded structures on films.

Certain features are obvious immediately in Figure 3.29. There are three layers where the temperature is constant to ± 2 mC for more than 5 meters. For purposes of identification, they are referenced by the approximate pressure at their centers, i.e., 1420 db, 1435 db, and 1445 db. Below these layers is a fourth layer that is not as well mixed

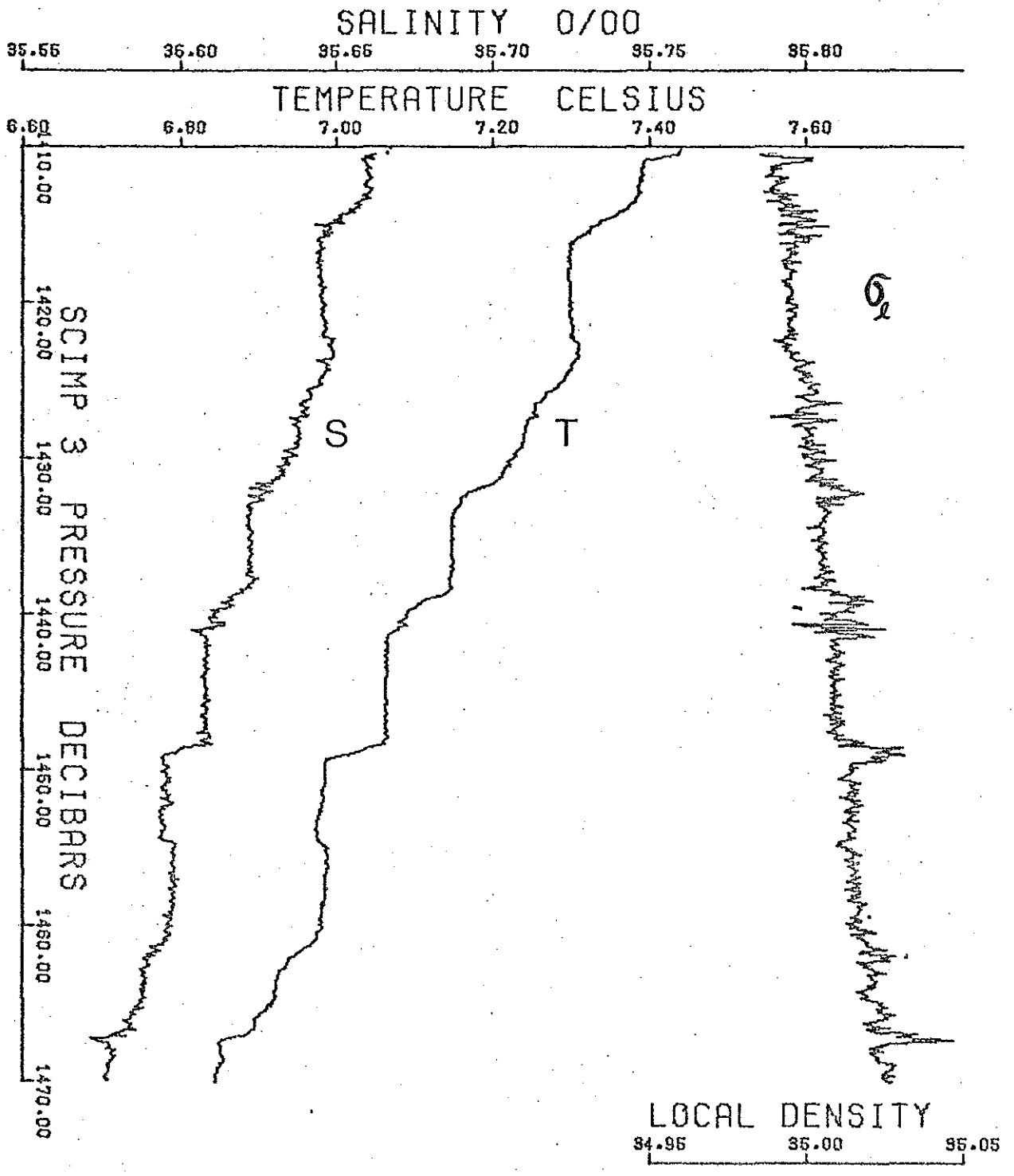

FIGURE 3.29 Series of steps from SCIMP 3. These layers appear to be more homogeneous than those in Figure 3.28.

and then a slight (0.012 C, .004°/oo) inversion in temperature and salinity at 1455 db. Beneath this inversion is a very sharp temperature and salinity interface at 1467 db that has strong banded structure on the films, but it does not have well developed mixed layers either above or below it. In this respect, this interface is similar characteristic to those described earlier.

The salinity structure of these layers is less homogeneous than the temperature in equivalent density units. For this temperature, pressure, and salinity, an increase of one part per million salinity has approximately the same effect on density as a decrease of 6 mC. The layer at 1445 db is homogeneous in salinity and density to the degree that the CTD can measure, but the other two layers have salinity and density increases of approximately 1 ppm across the layer. This suggests that these layers are not as actively stirred as the layer at 1445 db, because a completely well mixed layer has constant (potential) temperature, salinity, and (potential) density. Then the stratification in the layers decreases from the layer at 1420 to the layers below, and the images on the films have higher contrast on the interfaces between the deeper layers.

To put these observations into a more comprehensive framework, additional coverage of the same profile is shown in Figure 3.30. Situated above the steps just discussed is a double peaked inversion in both temperature and salinity. This intrusion inverts the prevailing gradients in temperature and salinity on its upper boundary (1374 db) where temperature and salinity both increase with depth. The salinity difference is relatively larger in terms of density so that there is a net

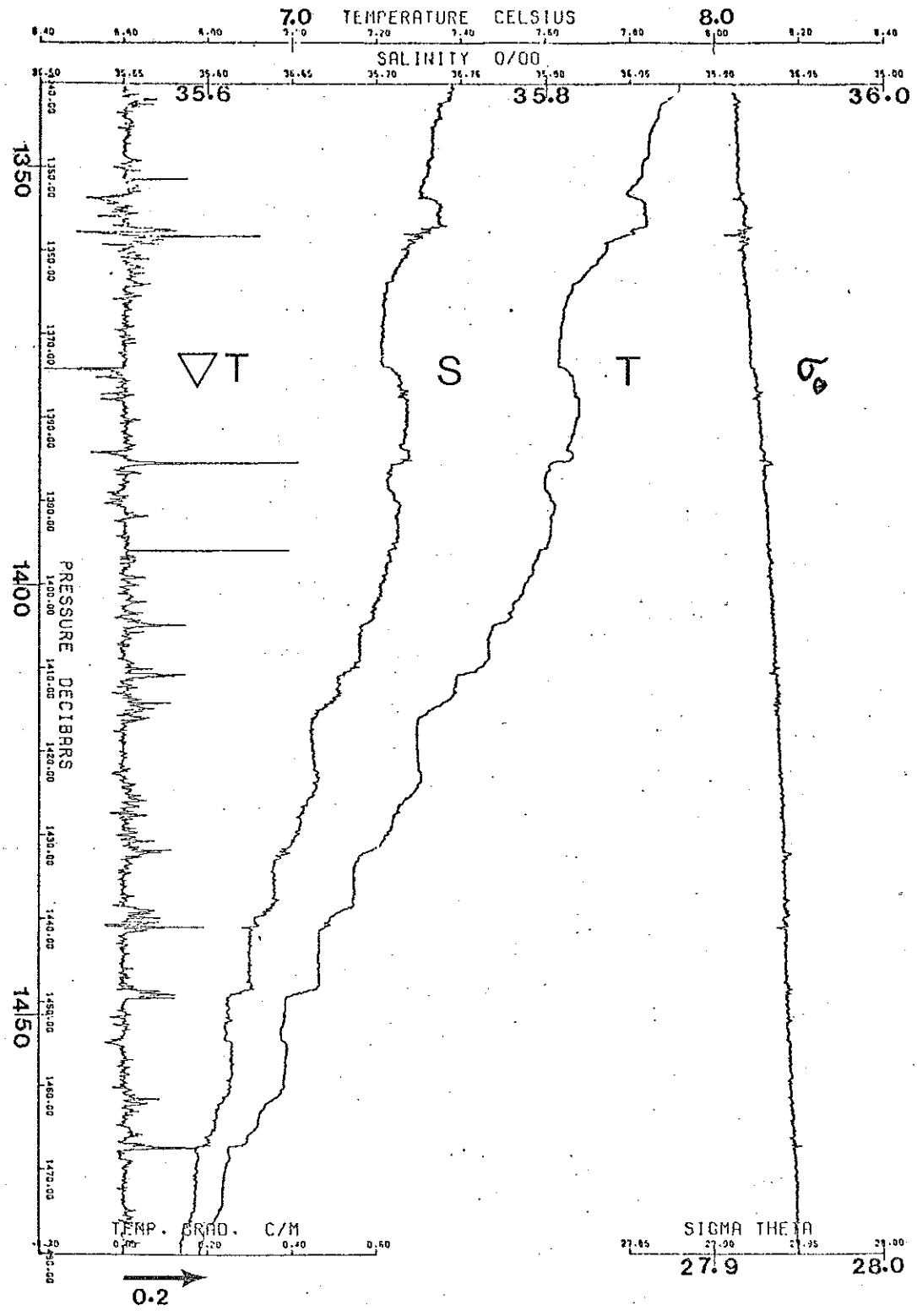

FIGURE 3.30 Weak inversion and steps below from SCIMP 3. The steps are the same as those in Figure 3.29. The layering appears to be the result of salt finger convection. The warm, saline intrusion increases the mean salinity gradient below, stimulating the convection.

density gradient at the top of the intrusion. Beneath the intrusion temperature and salinity both decrease with depth and these gradients are intensified, and their proportions are such that the density gradient on the bottom of the intrusion is also strong. A picture that emerges that is consistent with the character of the layers and images on the films is a cascade of salt below the intrusion which mixes deep layers under certain specific conditions. In this particular instance, layer formation occurs 20-50 meters below the local temperature and salinity maxima.

Implicit in the above discussion is the idea of an equilibrium salinity gradient. That is, given that both temperature and salinity decrease with depth, there is a maximum salinity gradient that can be sustained before the water column breaks down into convecting layers driven by salt fingering interfaces. The convection transports salt downward weakening the original mean salinity gradient until it is below the critical value. The value of this critical salinity gradient is probably not a constant but a function of density stratification (or mean temperature gradient), molecular properties and velocity shear. Also consistent with this model is a salinity excess propagating downward forming mixed layers successively. In some circumstances the salinity excess will dissipate by spreading over the water column, but in Figure 3.29 the step development has been terminated by another intrusion at 1455 db. Continued salt finger convection requires a monotonic salinity profile.

Most of the features of the model described above have been observed in the laboratory by Stern and Turner (1969). Some of these can

be readily identified in Figure 3.30. Assume that the water column was originally stratified in such a way that there are no convecting layers, the density is monotonically increasing with depth, and the temperature and salinity both monotonically decrease with depth. None of these need be a very smooth function of depth. Then a layer of water that is warmer and saltier than the ambient water at the equivalent density level intrudes into the water column. Why such an intrusion takes place is not important to the present discussion, but it suggests that there are many paths with different dilution histories that Mediterranean Water can take into the Atlantic Ocean. Also implicit in the presence of the intrusion is velocity shear, but this should be concentrated where the density gradient is large; and the total shear may be quite small. The situation is analogous to the experiments where a layer of warm salty water is floated on a deep layer that is stratified by temperature. In the Stern and Turner experiments, a sequence of layers formed progressively below the salty layer when the salinity contrast was large and the temperature stabilization was weak. Using these experiments as a guide, the interfaces that are closest to the intrusion are older than those that are further below.

Stern and Turner have also described how the character of convecting layers and salt fingering interfaces changes with time. As the system runs down the salinity difference across the interface decreases faster than the temperature difference combining for an increasing density contrast. Also, the fingers lengthen, resulting in a thickening of the interface at the expense of the layers. Finally, they report that although the convection had apparently stopped, the distortion

of the temperature, salinity and density profiles persisted.

To see how the profiles in Figure 3.30 can be related to the experiments just discussed, begin with the interface at 1448 db. This interface ought to be the youngest of the group and accordingly it is the thinnest, being less than one meter thick. The layer above it is the most homogeneous of the group with constant temperature, salinity and density to within the accuracy of the measurement, suggesting that it is well mixed by convection. The shadowgraphs that were taken at this interface showed vertical lines, but they seem to have a finer horizontal scale, i.e., the fingers have a small diameter or large wave number. Because the layer below this interface is not particularly well mixed, the density is difficult to determine unambiguously, but it appears that there is a density increase across the interface of about five parts per million.

The interface at 1440 db is about 2.8 m thick. There is a temperature inversion of about 0.01 C and a little less than one meter thick within the interface, but the salinity and consequently the density are not resolved on that scale. There appears to be a density difference of 4 ppm across the interface. Vertical banded structure is seen on several frames within this interface, making it an obvious case of a salt fingering interface. The temperature inversion may be a feature of the poorly understood boundary layer region between salt fingers and convecting layers. In their paper, Stern and Turner describe "buoyancy elements (generated by the salt fingers) accumulating and moving through the entire layer. These elements retain their identity...and they could in this way produce reversals in the sugar and salt gradients." Accordingly,

the temperature inversion just noted could be an accumulation of dense water from the sinking fingers, but the salinity resolution is inadequate to measure the density. At 1423 db there is another small inversion that could well be an element that has sunk from the interface above. It is located at the bottom of the mixed layer and it is about 1.5 m thick with increases of temperature, salinity and density of 0.008 C, 2 ppm, and 1 ppm, respectively.

Other features in the profile are less clear cut. For example, it is difficult to say whether the section between 1424 db and 1433 db is one thick interface or two interfaces with a thin relatively poorly mixed layer at 1428 m. But such details are less important than a consistent overall picture, particularly when such critical parameters as initial conditions and velocity shear are unknown.

Although a definitive statement cannot be made from these data, there appears to be an intimate relationship among intrusions, stepped structure and small scale turbulence. The unifying element among them is double diffusive convection.

Gregg (1975) has shown that the undersides of warm salty intrusions are the sites of intense thermal microstructure. The shadowgraphs from the OSFD show that these locations also have strong fluctuations in index of refraction. Both sets of measurements resolve very small scales (down to millimeters) and the high levels of variability at this scale indicate active mixing. Salt finger convection is the likely cause for microstructure because the mean gradients are correct for salt fingers and because the banded structure often seen in the shadowgraphs there is typical of salt fingers as seen in the laboratory.

The intrusions themselves are formed by lateral motions of layers with different T-S characteristics. They are constrained to flow at levels where their density is between the layers above and below, but there is no direct dynamic influence on the temperature and salinity structure. The vertical distributions of temperature and salinity may be altered to intensify, weaken or even change the sign of the prevailing gradients. When the salinity decreases rapidly with depth salt fingers and turbulence is favored.

In cases where the salinity gradient is very strong, the convection takes the form of a single interface with salt fingers and intense microstructure. Above and below the interfaces there are mixing layers, but these need not be homogeneous. There may also be nearby interfaces where the level of microstructure and the salinity step are considerably weaker. Figures 3.24-3.28 are examples of this situation and they all have sharp interfaces just below relative salinity maxima.

When the mean salinity gradient is weaker, but it is sustained over a deep region, a sequence of homogeneous layers separated by relatively sharp interfaces may develop. In this case the interfaces may have salt fingers, but they are not always seen on the shadowgraphs. The best example of this situation is seen in Figure 3.2, but there are also well developed in SCIMP 4 and SCIMP 6. The latter two have not been plotted at an expanded scale, but they are similar in character to the steps from SCIMP 2. Between the two limiting cases of a dominant sharp interface below a salinity maximum and the regular sequence of steps are situations where there are a few steps just below a salinity maximum. This is illustrated in Figures 3.28 and 3.30, where

in both cases, the sequence of steps is terminated by a salinity inversion that blocks downward development of the steps.

3.2 Measurements in the Tyrrhenian Sea

There have been measurements of stepped structure in many areas of the ocean, but nowhere is it more pronounced than in the Tyrrhenian Sea. Numerous attempts have been made to measure this structure since it was discovered in 1968 and it appears to be always present. (Johannessen and Lee, 1974; Molcard and Williams, 1975). The steps in the Tyrrhenian are different in some respects than the similar features found in the Mediterranean Outflow, the layers being generally thicker, more uniform and varying systematically with depth. These layers have some interesting properties in their own right, and it is also useful to compare these layers with those discussed earlier from the Mediterranean Outflow.

The Tyrrhenian Sea is one of the basins of the Mediterranean Sea. It is bounded by Sicily and the Strait of Sicily to the south, by Sardinia and Corsica to the west, while the western coast of Italy completes its triangle perimeter. The water depth is greater than 3000m in the central portion of the basin and there are several seamounts there which rise to within 2000m of the surface. The Tyrrhenian Sea is connected to the Eastern Mediterranean through the Strait of Sicily where the sill depth is approximately 300 m and with the rest of the Western Mediterranean (the Balearic Sea) through a passage with a sill depth of 1500 m. Four major water masses have been identified by Wüst (1961) using the core method, and their interactions may be important to layer formation. The surface waters down to a depth of approximately 75 m are of Atlantic

origin and probably unimportant in the subsequent discussion. Between 200 and 600 m is the Levantine Intermediate water, and this water is found throughout the Mediterranean at various depths. It is formed near Rhodes in late winter at a temperature of 15°C and a salinity of 39.1% at a time when convection allows it to penetrate to a depth of 100-200 m. The salinity maximum of approximately 38.7% is at a depth of approximately 400m. The sill depth is 1500m so deep water is formed locally or it flows in at that depth from the Balearic. There is some evidence for bottom water formation in the northern part of the Tyrrhenian Basin in the Ligurian Sea, but the deep water of the Tyrrhenian could also originate in the Balearic Basin. The Deep Water between 1500 and 3000m is the third water mass, while the fourth is the Bottom Water found at depths greater than 4200 m.

The stepped structure is found at a depth of 500-1500 m near the center of the basin where it is deepest. This represents a transition zone between the two core water masses identified above, viz., the Levantine Intermediate Water above and the Deep Water below. The situation seems analogous to the spreading of the Mediterranean Water in the North Atlantic, and in fact, the Levantine Water can be traced to form the core of this intrusion (Wüst, 1961). Step formation at the underside of a high salinity intrusion suggests salt finger convection here and this is why SCIMP was deployed in the region. Although this aspect of the experiment was not entirely successful because the images on the films were very weak, the precision CTD measurements themselves are a very interesting data set.

The data to be discussed below was taken with SCIMP from the R/V

Maria Paolina G. in May of 1973. The cruise was undertaken specifically to study the stepped structure of the Tyrrhenian Sea and the primary instrument was a Bissett-Berman STD. In addition to the survey work with the STD, SCIMP was deployed to measure the smaller scale structure and also to photograph inhomogeneities in index of refraction. A total of seven dives were made with SCIMP, the last two of which were YO-YO excursions. Table 3.5 summarizes the data set. The layering is not prominent in all the dives but it can be identified at least in part of the profile, in the last five. The Yo-Yo stations are particularly useful because the layers were well developed there and the last two dives represent eight profiles through them. Since the layers in the Tyrrhenian are generally thicker and more uniform than those in the Mediterranean Outflow, they are easier to trace from one porfile to another. There is great uncertainty in trying to follow any feature in the earlier data set, but here the continuity is nearly certain.

The configuration of SCIMP for this experiment was identical to that for the Mediterranean Outflow experiment described earlier and it suffered from some of the same malfunctions. Most serious of these was the slow response of the conductivity sensor which led to salinity spiking and the loss of small scale salinity and density information. Also, the pressure signal was erratic on some of the dives and had to be inferred on the basis of temperature and continuity of the drive.

As mentioned earlier, the shadowgraph images on the films from the Tyrrhenian Sea are very weak. In fact there are only a few frames from the deep water where any image can be identified in a still frame. By viewing the film as a motion picture, images are often clearly visible

TABLE 3.5

SCIMP Series 3 Data Summary

Dive	Time/Date	Latitude	Longitude	Maximum Depth	Comments
1	0955/4-5-73	39 33.7 N	13 13.2 E	550 m	
2	1257/7-5-73	40 18.4 N	12 46.0 E	960 m	
3	1332/8-5-73	39 26.2 N	12 34.0 E	1500 m	
4	0918/10-5-73	39 28.5 N	12 46.0 E	1200 m	Pressure Bad
5	1732/10-5-73	39 27.6 N	12 47.6 E	1200 m	Pressure Bad
6	1420/11-5-73	39 30.1 N	12 48.0 E	910 m	910 m/580 m/870 m Yo-Yo
7	2244/11-5-76	39 30.1 N	12 47.3 E	870 m	820 m/540 m/870 m Yo-Yo

and they have vertical orientation to their structure. The images are found on the interfaces between the well mixed layers and they are usually associated with high gradient regions within the interface. But as in the Mediterranean Outflow data, the relationship between images and large gradients is a loose one.

In this section, the layers in the Tyrrehenian will be examined to test some scaling laws based on salt finger convection and to apply a convective turbulent boundary layer model to the interface. Because of their size and uniformity, these layers must certainly be near an extreme of the parameter range. Also the layers have been observed repeatedly for five years which suggests an equilibrium or slowly varying phenomenon. For the boundary layer calculations, the SCIMP Yo-Yo stations provide eight profiles which are essentially in the same position within a 20 hour period.

3.2.1 Layer Thickness

The homogeneity of some of the layers in the Tyrrehenian Sea is truly remarkable. There are layers which are in excess of 100 m thick that are as well mixed as the W.H.O.I./Brown CTD can measure. Which is to say that the potential temperature is constant to within $0.001^{o}C$ while salinity and potential density are constant to within $\pm 0.001^{o}/oo$. Figure 3.31 shows the profile of potential temperature, salinity, and potential density for one of the dives in the region of the steps, SCIMP 4. The steplike structure in all three plotted variables is evident and the layers appear to become thicker and more uniform with depth. These layers are much thicker than those in the Mediterranean Outflow, which showed no systematic variation with depth. Although the

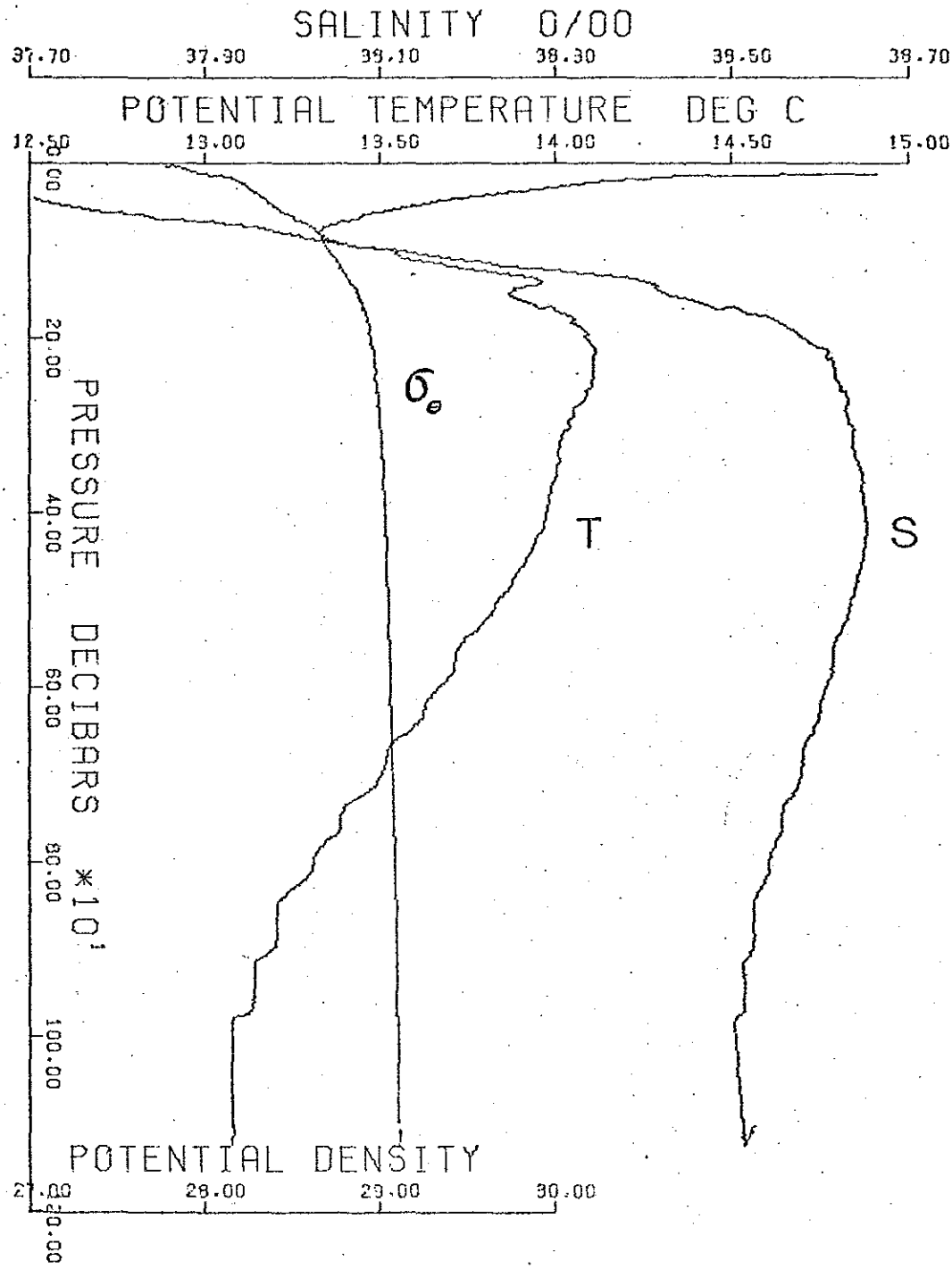

FIGURE 3.31 Profiles of temperature, salinity, and potential density from the Tyrrhenian Sea. The stepped structure is prominant below 700 decibars. The layer thickness increases with depth to more than 100 m.

layers in the depth range 500-800 m are not well mixed in this profile, subsequent dives found these layers to be well mixed at progressively shallower depths.

In Section 3.1 an expression for layer thickness, H, was derived based on the dynamics of salt finger convection, viz.,

$$H \leq \left(\frac{D\nu}{(1-r)C}\right)^{3/4}\left(\frac{\alpha\Delta T}{\beta\Delta S}\right)\left(\frac{\beta\, dS_s}{dz}\right)^{-1/4} = B\,\frac{(\alpha\Delta T/\beta\Delta S)}{(\beta\, dS_s/dz)^{1/4}} \quad (3.15)$$

but the constant of proportionality, B, is a combination of several poorly measured constants that may not even be constants. Note that this relation is not entirely explicit because the approximation $H = (\beta\Delta S)(\beta\, dS_s/dz)$ has been used in the derivation. Using this approximation again yields

$$H \leq B_1\left(\frac{\alpha\Delta T}{\beta\Delta S}\right)^{4/3}(\beta\Delta S)^{-1/3} \quad (3.16a)$$

where

$$B_1 = B^{4/3} \quad (3.16b)$$

There are many approximations involved in deriving the above formula, some of which may not be justified. One that appears to be contrary to the observed data is that the entire salinity differerence between two uniform layers derives the salt finger convection. As in the interfaces in the Mediterranean Outflow, there are often several smaller interfaces embedded within the larger interface and the $\beta\Delta S$ in

the salt finger flux law may be only a fraction of the difference between the layers. This is also consistent with the images on the shadowgraphs, both here and from the Mediterranean Outflow where there are often several bursts of bands found on a single interface.

To evaluate the above scaling, the function,

$$\frac{H(\beta\Delta S)^{1/3}}{(\alpha\Delta T/\beta\Delta S)^{4/3}}$$

is calculated for several layers in the Tyrrhenian Sea, for the mean of layers with salt fingers in the Mediterranean Outflow, for the layers in the small staircase in SCIMP 1 from the same experiment, and for other published cases of layering where the conditions are correct for salt fingers.

Figure 3.32 shows the salt finger layer thickness scale plotted against layer thickness for the measurements indicated. If the scaling were correct, the function would be a constant. From the graph it appears that the function increases with H and the scaling based on the total salinity difference is inappropriate.

3.2.2 Convective Boundary Layer

If the layers in the Tyrrhenian Sea are uniform because they are stirred by convection due to salt fingers, then the interfaces between the layers must consist of the field of salt fingers and the boundary layers where there is a transition between the salt fingers and the mixed layers. According to this model the boundary layers are convective because they are driven by the unstable buoyancy from the salt fingers. The governing parameter n convective flows is the Rayleigh

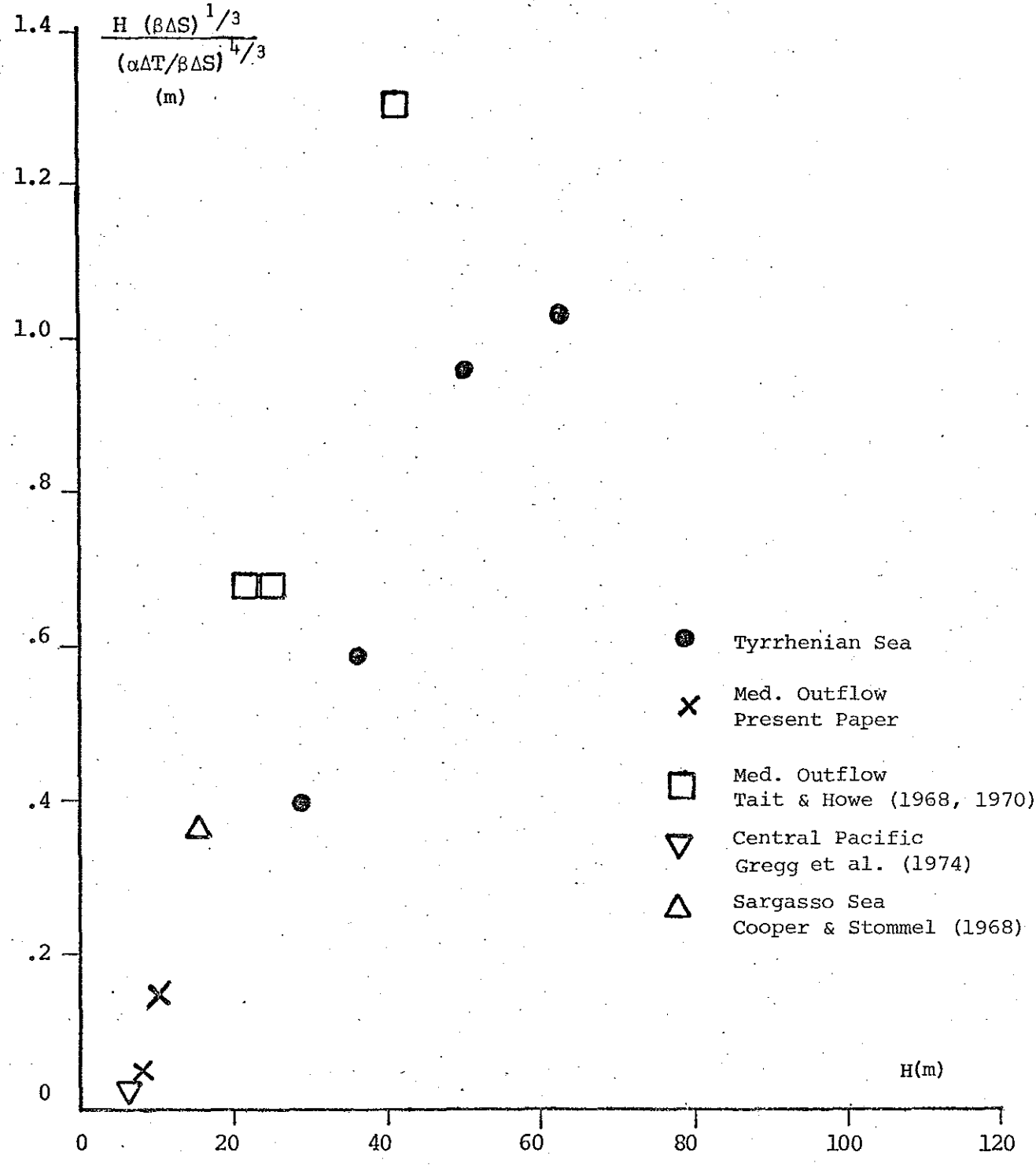

FIGURE 3.32 Evaluation of dimensionless layer thickness calculated for salt finger convection. The abcissa is the measured layer thickness for examples of regularly spaced steps where the gradients allow salt finger convection. If the measurements supported the theory, the value of the ordinate for the points would be a constant.

number,

$$R_a = \frac{g\alpha \Delta T \ell^3}{\nu K_T} \tag{3.17}$$

which was originally derived for the flow of a fluid between two horizontal plates. The distance between the plates is ℓ and the lower plate is warmer than the upper by ΔT. In the more general case, which applies to the interfaces, the flux Rayleigh number for buoyancy is defined

$$R_{af} = \frac{F_B \ell^4}{K_B^2 \nu} \tag{3.18}$$

where F_B is the buoyancy flux and K_B is the diffusivity for the property whose anomaly causes the density anomaly. In the case of salt fingers,

$$F_B = \beta F_S - \alpha F_T = (1-r)\beta F_S \tag{3.19}$$

and the density anomaly is due to salt, $K_B = K_S$. Typical values are $\nu = 10^{-2} \frac{cm^2}{s}$, $k_s = 10^{-5} \frac{cm^2}{s}$ and $\beta F_S = 10^{-5} \frac{(cm/s)^2}{s}$ making $R_{af} \cong 10^7 \ell^4$ (c.g.s.). If the interface thickness is interpreted as the boundary layer thickness, then $\ell \cong 10^3$ and $R_{af} = 10^{19}$. Such a high Rayleigh number has never been approached in the laboratory and the flow in this regime may be entirely different than any measured or considered theoretically. In earlier sections the ambiguities in making a single measurement of a turbulent field made stronger conclusions impossible, but here there is an opportunity to make a separation

into mean and fluctuating fields. The 2 Yo-Yo stations from SCIMP provide 8 profiles close together in time and space.

From the composite temperature profile in Figure 3.33, the deepest interface that was measured all 8 times is chosen. This layer near 780 m remains relatively sharp throughout and the layer above and below are well mixed. The actual depth of the interface changes with time due to internal wave motions, and to remove this unwanted effect, a point of reference is chosen relative to the interface structure itself to establish mean properties of the interface. The bottom edge of the interface is picked as a relative reference because it is the probable site of salt fingers and because it is a well defined point on all the profiles. Figure 3.34 is a composite of the eight potential temperature measurements of the interface aligned so that the sharp gradients at the bottom are at the same level.

Before average profiles are presented, some of the features of the individuals are noted. The most striking thing about them is their similarity. Even though they are contained within a time span of approximately 12 hours and the launch positions are only separated by about a kilometer, the consistency in the general shape of the profile is surprising. Within the uniform layer below the interface there are several instances where there is a small blob that is approximately 0.005^{o}C warmer than the rest of the layer. There is one about 2 m thick 3 m below the interface in profile 6 and another slightly thicker and closer in profile 7. These blobs also appear to be saltier than the rest of the layer, though only by about 0.001%, making the blobs the

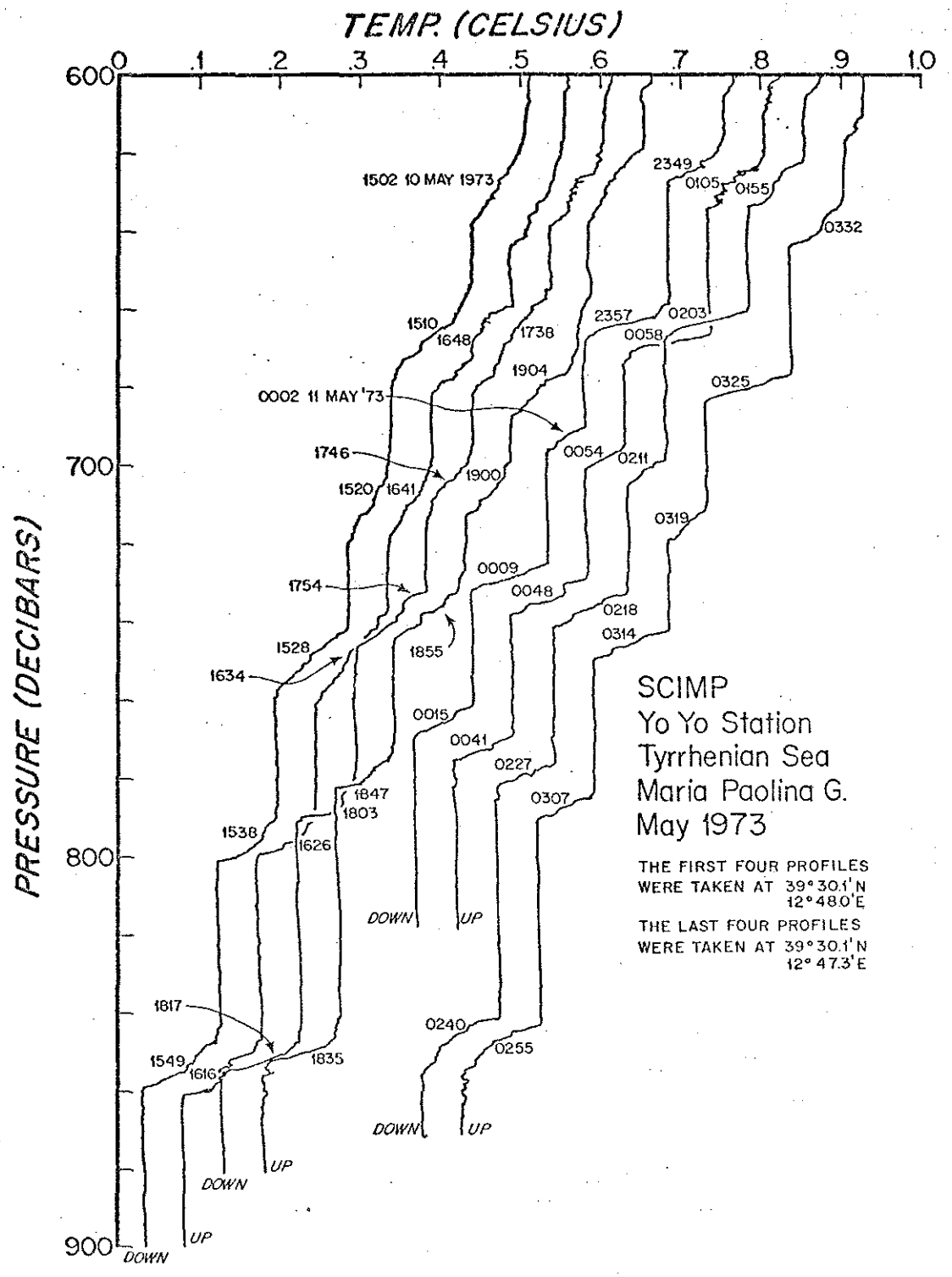

FIGURE 3.33 Compsite of temperature profiles through stepped structure. Each profile is offset 0.05 C with an additional 0.05 C between the two groups of four. The numbers beside the interfaces are the time. This figure is an excerpt from Molcard and Williams, 1975.

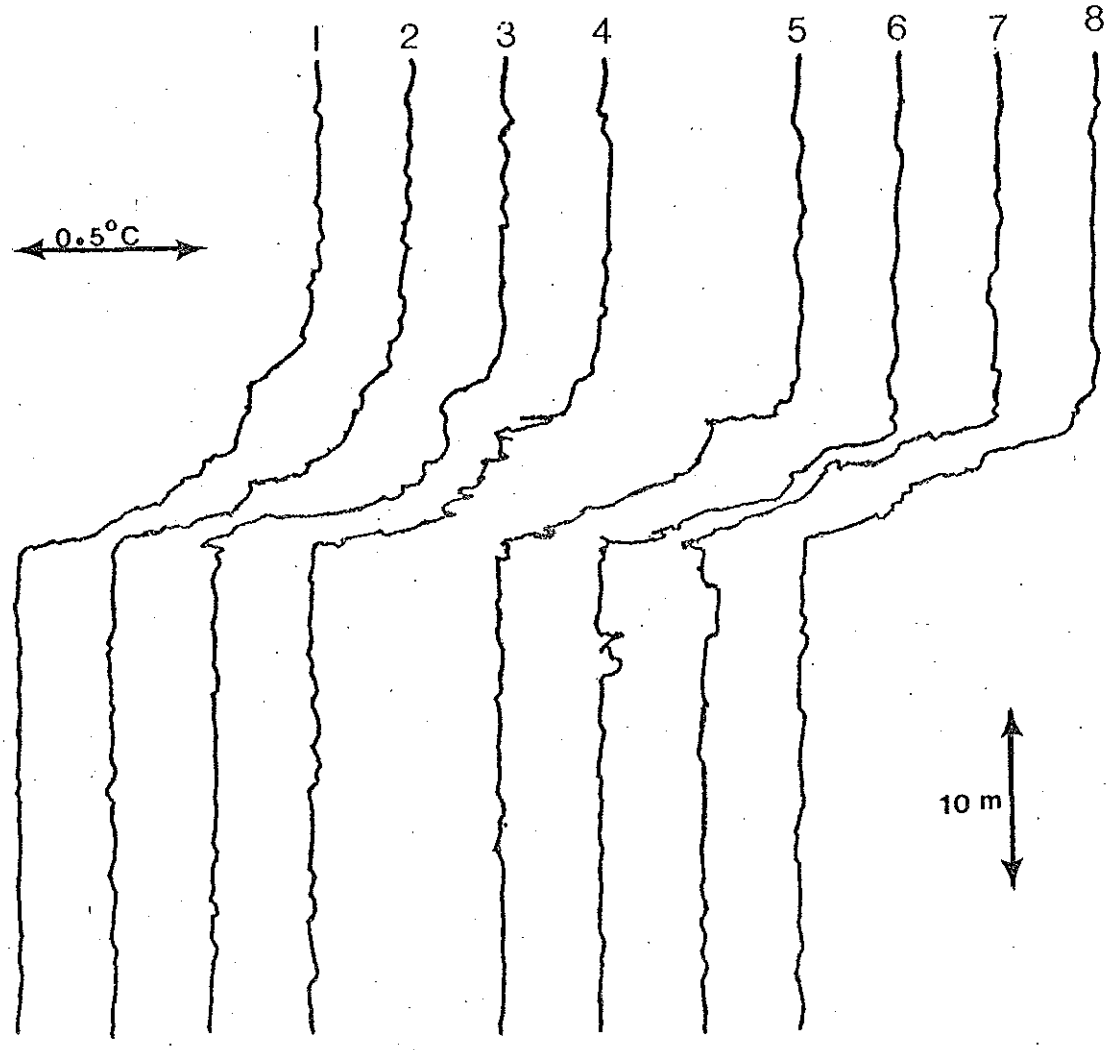

FIGURE 3.34 Potential temperature profiles for interface near 780 decibars in Figure 3.33. Each profile has been positioned so that the bottom edge is at the same level and offset 0.02 C. There is an additional offset of 0.02 C between the two groups of four.

same density as the layer. But this conclusion presses the limits of accuracy for the CTD. These may have been released or swept from the salt finger interface. The vertical length scale of these anomalies is the same order of magnitude as the distance from the interface, which is consistent with the similarity model of the buoyant plume developed in Section 2.1.2. There is also a weaker anomaly that is thicker ($\cong 7$ mm) and further from the interface ($\cong 10$ mm) in profile 4, but it is difficult to see in Figure 3.34. Its size and position are also consistent with the similarity model. Similar anomalies are not present above this particular interface, but the upper boundary of the interface is not sharp. These two observations suggest that the layer above is not actively convecting because there is no sharp interface with salt fingers there. Nor are there any blobs being swept away or released there. On the basis of these observations, the following calculation assumes a single plane source of buoyancy located at the bottom of the interface in Figure 3.34.

The data from the 8 profiles was first corrected to bring the salinities of the two layers to standard values. The reason why salinity of the layers varied from profile to profile is not certain, but it appears to be instrumental because there are not comparable variations in potential temperature. It may be that the calculated salinity has a sink rate dependence or it may be related to the erratic pressure sensor. The pressure sensor did have an "offset slip" on one of the dives (see Appendix A) so it must be suspect. After this correction the data was averaged over approximately 45 cm; the number of points in the average varied from 11 to 14 depending on the sink rate. A base-

line was then established for each profile corresponding to the alignment in Figure 3.34. For each point relative to the interface, an average and standard deviation of the eight profiles of temperature, salinity, and σ_t was then computed. These are shown in Figures 3.35-3.37.

The mean temperature profile is smooth and the variance is nearly constant between the reference and a point 7 m above. A reasonable fit to the mean profile can be made with a logarithmic distribution. Long (1972) has predicted this form for the temperature field by assuming that the temperature field is similar to the velocity and using an analogy with flow over a flat plate. This theory requires that temperature be proportional to density, but Figures 3.36 and 3.37 suggest that this is probably not the case within the boundary layer here.

The important variable for the convective boundary layer model is the density, here expressed in terms of σ_t. This function underestimates the actual density by a factor of approximately 3 under these conditions, so that the density difference of 0.002 between layers is 0.006-0.007 when expressed in terms of local potential density. Regardless, the form of the profile and general conclusions should not be greatly affected. The mean density appears to be a maximum near the interface reference. The two extreme points at and just above the reference are probably instrumental artifacts due to salinity spiking. This is given further support by the high level of salinity variance seen in Figure 3.36. Other points appear to be reasonable both in the salinity and density profiles. If these two points are disregarded, then the mean profile of Figure 3.37 is approximately linear, both above and below the reference level, stable above and unstable below. If there

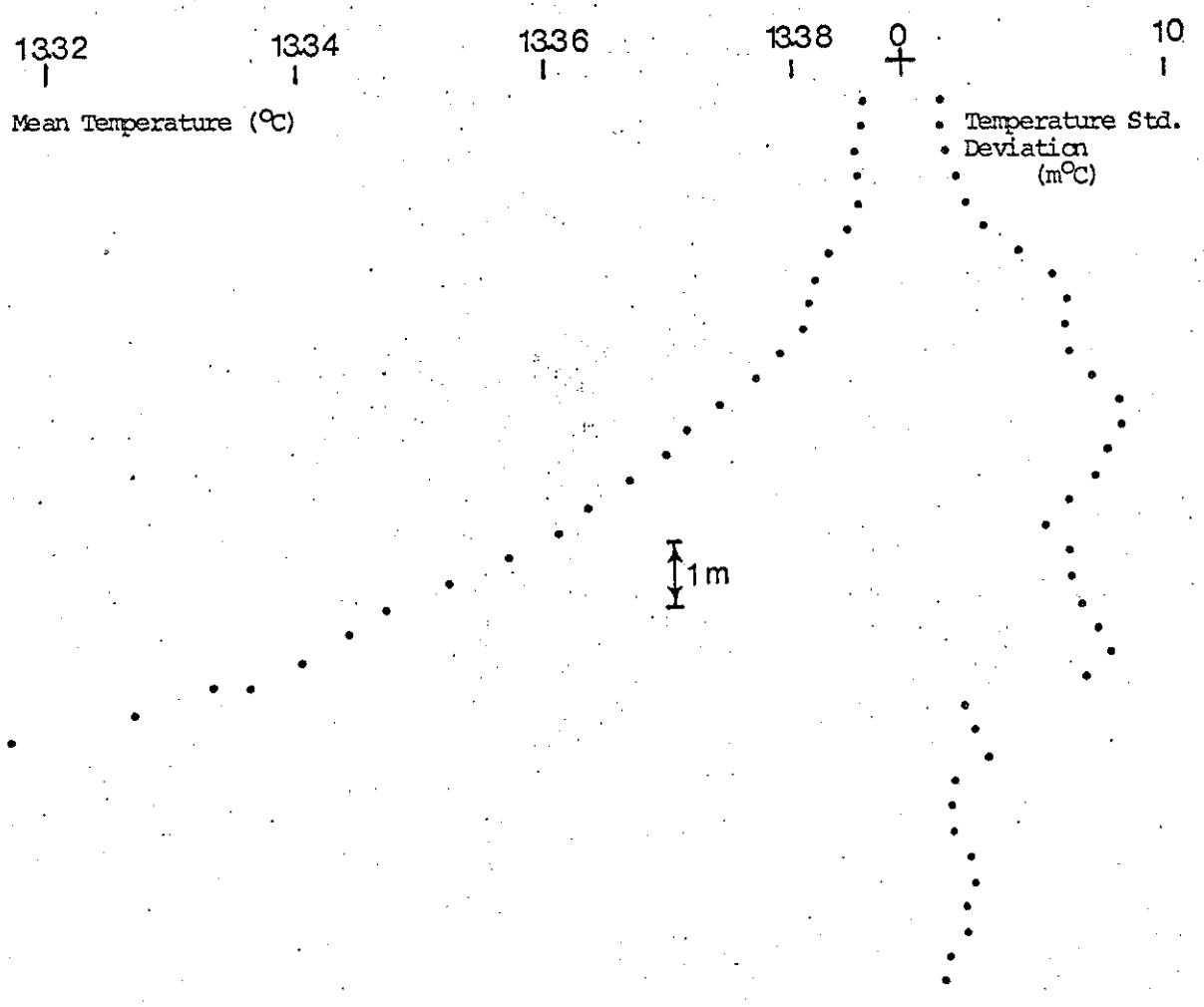

FIGURE 3.35 Mean temperature profile and standard deviation for 8 profiles of the interface in Figure 3.34. The mean is a smooth curve that can be fit with a logarithmic, while the standard deviation is nearly constant.

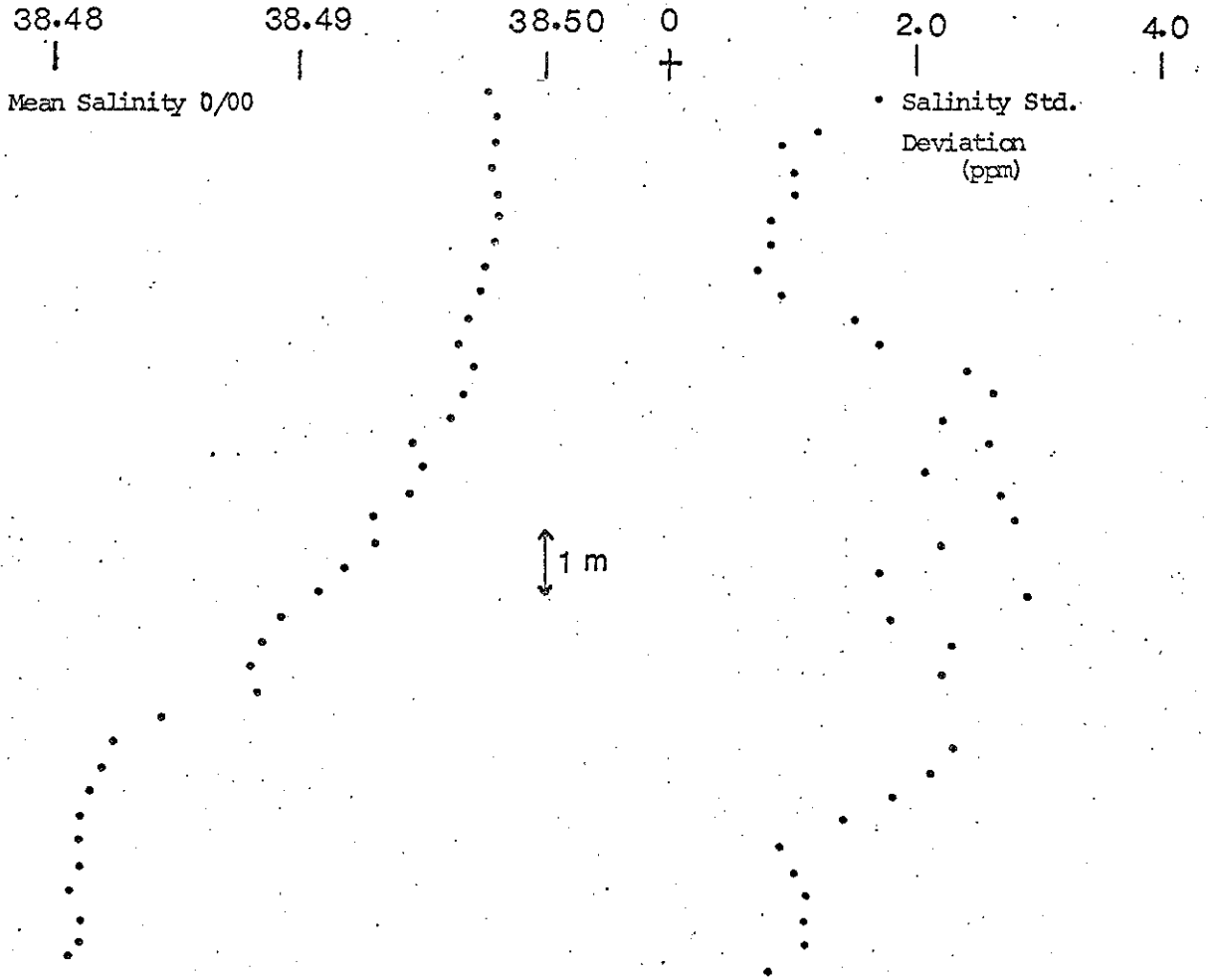

FIGURE 3.36 Mean salinity profile and standard deviation for the same interface as in Figures 3.34 and 3.35. Salinity has been scaled to a constant value in the layer below.

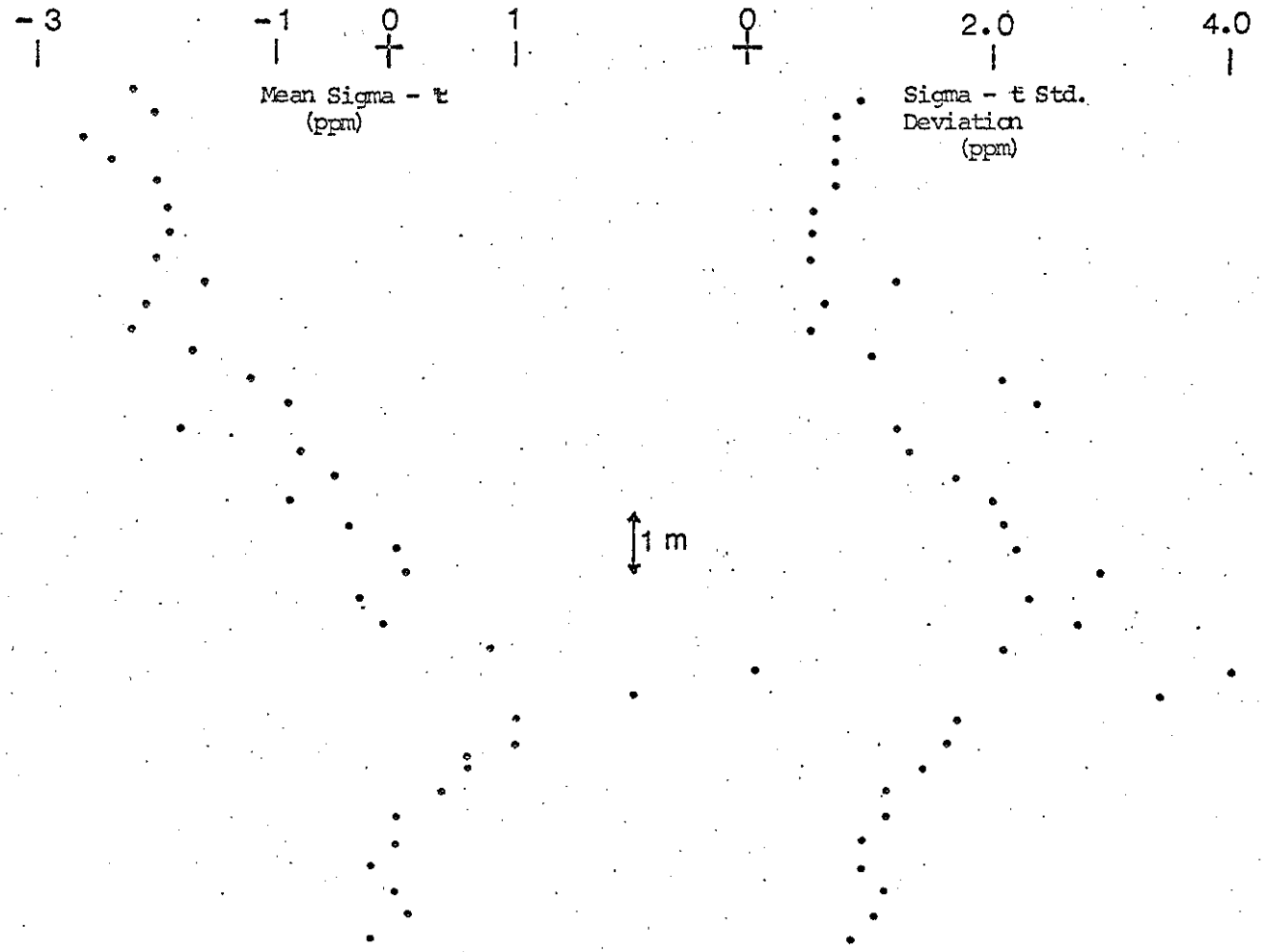

FIGURE 3.37 Mean sigma -t profile and standard deviation for interface in Figures 3.34 - 3.36. The mean of sigma -t is referred to the layer below the interface.

is a convective boundary layer above the interface, then it is undetectable because of the salinity spiking in the CTD. In view of this difficulty, the boundary layer model is inconclusive, but receives some support.

4. SUMMARY AND CONCLUSIONS

SCIMP is a unique instrument that can image very weak inhomogeneities in the deep ocean by the shadowgraph technique. These shadowgraphs measure variability with a length scale that is comparable to that of molecular diffusion. In this study, the shadowgraphs are compared to concurrent measurements of temperature, salinity, and density to discover the characteristics of some of the mixing events in the deep ocean.

The finestructure of temperature, salinity and density often has evidence of variability at smaller scales. But it is usually ambiguous so that it is necessary to perform an experiment where both the finestructure and fluctuations associated with diffusion are measured. Since the latter are indicative of turbulence and mixing which is an important and poorly understood aspect of ocean dynamics, this set of measurements can be used to establish when mixing occurs and suggest possible mechanisms.

Mixing in the deep ocean can occur when the shear in the current field is so great that the flow overturns and breaks down into turbulence. Or, when the temperature and salinity gradients have the same sign, there may be double diffusive convection which is characterized by sharp gradients on a thin interface with turbulent convection above and below. In either case there is irregular structure in the temperature, salinity, and density fields and small scale fluctuations in these properties may be found on the interfaces where the gradients are the most intense. The shadowgraph is sensitive to the second derivative of refractive index, and there are no images where the water

is homogeneous. Refractive index is closely related to density, but not perfectly, so that wherever there are large gradients of temperature, salinity, or density, there are probably also large gradients in refractive index.

The contrast in the shadowgraphs varies over a broad range, depending on the strength of the anomaly in refractive index or focal length of the structure in the seawater. Most of the images in the shadowgraphs are chaotic, but some of them have a periodic structure which is aligned vertically. These bands are characteristic of salt fingers in the laboratory and the results from this study suggest that salt fingers in the ocean have a similar appearance.

Whether the images are banded or have a random appearance, they nearly always occur on interfaces. In this discussion, an interface is a place where temperature and/or salinity gradient is several times larger than the prevailing mean over a distance of approximately 1-10 m. Often these interfaces have layers with very weak gradients above and below, and when there is a regular sequence of interfaces and homogeneous layers, it is called stepped structure.

In the eastern North Atlantic, where the influence of the high salinity water from the Mediterranean Sea is particularly strong, SCIMP was deployed 6 times. Each time the CTD profiled from the surface to a depth of approximately 1900m, while the OSFD photographed shadowgraphs from approximately 1000 m to the bottom of the dive. Using the interface definition above, 398 have been identified in the portions profiles that are covered by the shadowgraphs, and, of these, 135 or about 1/3 have detectable images. This is the first important result in this

study: a significant fraction of the interfaces in Mediterranean Outflow have variability extending down to the scale of millimeters in refractive index. This suggests that there is turbulent mixing on these interfaces resulting in accelerated vertical transport of heat and salt.

A large number of interfaces with images have some that are banded, and nearly all the banded images are from interfaces where conditions allow salt finger convection. There are 18 interfaces where there are bands that have particularly high contrast, and these have been used to evaluate some of the properties of salt fingers in the ocean.

There are two particular locations relative to the temperature and salinity structure where the high contrast bands occur. The first is at interfaces within the stepped structure where there is a regular sequence of uniform layers separated by interfaces where temperature and salinity both decrease with increasing depth. The second place high contrast bands are found is below a relative salinity maximum. This feature indicates that there is a warm saline layer intruding into a fresher environment by horizontal advection.

Although the parameter range for salt fingers in the ocean cannot be duplicated in the laboratory, and available theoretical models are highly idealized, some of the calculations from them can be compared to salt fingers in the ocean. The salt finger diameter is proportional to the -1/4 power of the mean temperature gradient, and the measurements from SCIMP are consistent with this relationship. Other parameters that are typical for interfaces with high contrast bands in

terms of the mean and standard deviation, are temperature difference = 0.016 ± 0.064°C, salinity difference = 18 ± 12 ppm, density difference = 6.5 ± 3.5 ppm, Turner Number = 1.6 ± 0.3 and thickness = 2.6 ± 2.2 m. For comparison a group of interfaces has been selected from the stepped structure, that have similar finestructure but no detectable images in the shadowgraphs. The average values of all the same parameters for this group is 10 - 30% smaller except interface thickness, which is 30% larger. This means that the interface gradients are stronger in the cases where there are bands by up to a factor of 2.

When there is banded structure, it is not found continually across an entire interface. Generally there is only one or two consecutive banded shadowgraphs corresponding to 10-20 cm, but there may be several instances within a single interface and there may also be more random structure interspersed. This suggests that length of salt fingers in the ocean may be much smaller than the interface thickness. Apparently salt fingers occupy only a small fraction of the interfaces between homogeneous layer and the remainder is a turbulent convective boundary layer that is driven by salt finger convection. Theoretical calculations support a length of 10-20 cm for salt fingers.

The interface thickness has been taken to be the distance between two points on either side of the interface where the temperature gradients are weak. In some ways, this is just a practical consideration because the CTD on SCIMP could not resolve salinity and density where the gradients were strong. However, SCIMP normally samples every 5 cm

so that the thermal structure can be sensed down to length scales that are not greatly separated from the scale of the fluctuations in the shadowgraphs. Careful examination of the thermal structure within the interface shows that is generally a higher level of variability with length scale of tens of centimeters on the interfaces with active shadowgraphs. This suggests that the variability may be continuous from a wavelength of meters down to millimeters. Such continuity is a necessary condition for turbulent flow, and in this case the turbulence generated by relatively thin fields of salt fingers that are found within an interface. There may also be turbulent flow within the homogeneous layers, but there it is invisible to the shadowgraph and a thermometer cannot measure it.

Most of the measurements were made in regions where the temperature and salinity gradients allow salt finger convection, and nearly all were where double diffusion is possible. This makes the data set incomplete because a critical test would be to compare the occurrance small scale structure in shadowgraphs in situations where double diffusion convection is impossible to those where it is theoretically possible. However, there are conditions that favor either turbulence generation by shear or double diffusive convection, and evaluating the census of interfaces and turbulent interfaces brings out some trends. The 398 interfaces are distributed throughout the depth interval covered but they are most frequent near the salinity maximum (1.0 - 1.1 km), where there is complex interleaving of waters. A relatively large number of interfaces are also found at the depth where stepped structure occurs (1.3 - 1.5 km), while the distribution of turbulent interfaces

peaks in this interval. There are very few turbulent interfaces below 1.6 km. Most of the interfaces have a density difference in the range 2-4 ppm, but there is an increasing fraction that are turbulent with increasing density difference. Similarly, there is an increasing turbulent fraction with increasing salinity difference in the sense that allows salt fingers, but there is no trend where the salinity gradient has the opposite sign. This appears to be the most distinctive characteristic of interfaces with small scale variability in the shadowgraphs, and it is consistent with turbulence production from salt finger convection.

Finestructure can be quantified by calculating the autospectrum of the temperature distribution. The shape and level of the resultant spectra can then be compared to theories of turbulence and internal wave motion. Internal waves may create finestructure in temperature by straining a more uniform distribution, but there need not be accelerated mixing or small scale turublence unless they overturn or break. The stepped structure that does not appear to be the direct result of internal waves, but the model spectrum (Garrett and Munk, 1975) for internal waves is a good basis for comparison. Using the normalization for internal waves, the displacement spectra from the stepped structure are uniformly higher than similar measurements from a number of depths in the Sargasso Sea (Hayes et al., 1975). The difference is up to an order of magnitude in the band 0.1 to 1 cycles/decibar.

A further comparison has been made between two temperature gradient spectra from SCIMP data. One is calculated from the stepped structure, while the other is from a relatively featureless profile from

nearby at approximately the same depth. The latter spectrum is nearly flat, but temperature gradient spectrum from the steps is higher at all wave numbers and falls off with a slope of approximately -1. This is consistent with a model of turbulence effected by buoyancy (Lumley, 1964). There is a significant peak in the spectrum in the vicinity of 2 cycles/meter, which is equal to length scale of salt fingers calculated theoretically and inferred from shadowgraph measurements. The turbulence in the stepped structure is generated by buoyant convection from the thin ($\sim$10 cm) salt finger interface, and the spectra verify this model.

The CTD on SCIMP is nearly identical to that lowered on a cable, so that measurements of a distinctive feature such as the stepped structure by both can be used to evaluate the effects of ship motion on the measurements. A comparison shows that temperature spectra from the two appear to be identical in the wave number band 0.5 to 2.0 cycles/decibar, but the level of the spectrum from SCIMP is higher above and below that band. At high wave number, the loss of variance for the standard CTD may be due to the averaging procedure used to sort the data to a uniformly spaced series. The discrepancy at low wave number does not appear to be an instrumental artifact.

Layers of high salinity water appear as intrusions in the Mediterranean Outflow, and high contrast shadowgraph images are usually found at interfaces just below such a relative salinity maximum. The intrusion represents horizontal advection of more saline water, but it enhances the mean vertical salinity gradient below by its presence. Since the salinity gradient is the energy source for salt

finger convection, this is a most likely site for salt fingers to be found. In some cases a series of interfaces separated by relatively uniform layers may be found just below a relative salinity maximum, and it continues downward until a point is reached where the salinity gradient changes sign. This suggests that the stepped structure develops downward from a saline intrusion and that the very strong interfaces with high contrast images that are so often found on the underside of intrusions are very closely related to stepped structure. The dimensionless salinity gradient, expressed in terms of the Turner Number, is relatively weaker for the stepped structure than for the intrusive interfaces, indicating that the latter may represent a slightly different parameter range for salt finger convection.

A series of measurements with SCIMP in the Tyrrhenian Sea show there is also stepped structure found below the deep salinity maximum there. These layers are generally thicker and more homogeneous than those in Mediterranean Outflow; there are layers greater than 100 m thick that have no detectable potential density gradient. The interfaces are also thicker and the layer thickness increases systematically with depth. There is banded structure on the interfaces, but the contrast is so low that it is barely detectable. Using the characteristics of these layers, along with measurements discussed above from the Mediterranean Outflow and other published measurements of stepped structure, an expression for layer thickness based on a model for salt fingers has been evaluated. The model does not predict the layer thickness correctly. This is probably because the model assumes that salt fingers span the entire distance between mixed layers, and

this is a very poor assumption here and for the data from the Mediterranean Outflow.

Finally, a series of Yo-Yo stations by SCIMP has measured the same group of interfaces eight times within twelve hours. To see if these interfaces can be modeled as a turbulent convective boundary layer, one interface has been selected and the eight profiles through the interface brought to a common reference at the lower edge of the interface. From these, a mean profile and standard deviation from the mean has been calculated for temperature, salinity and sigma-t. The mean temperature profile is fairly well modeled by a logarithm curve as predicted by some theories, but the variance is nearly constant rather than increasing with distance from the reference level. There are problems with salinity spiking in the salinity and density calculations, but there is strong evidence for an inversion in the mean just below the reference level. The variance of salinity and density are also nearly constant. A constant variance profile has also been found in laboratory measurements of thermal convection, but it is not predicted theoretically.

APPENDIX A

INSTRUMENTATION

Most of the instruments used in this study are unique or have recently been developed and come into common use. Since the performance of these instruments may not be well understood at this time, caution must be exercised in interpreting the data. But once the instrumentation is properly evaluated, this unique data set allows analysis at resolutions that had previously been inaccessible. This appendix is a description of the instrumentation including comparisons with more conventional probes.

The measurement package is known as SCIMP which is an acronym for Self-Contained Imaging Micro-Profiler. The probe has no mechanical connection to the surface, but it sinks freely according to a preprogrammed schedule which can be altered by acoustic command from the surface ship. The platform Autoprobe (Burt, 1974) performs these control and communication functions. One of the two measurement instruments is a precision CTD which measures electric conductivity, temperature and pressure, interpreted as depth. This unit is nearly identical to the unit developed at WHOI by N. Brown for hydrographic work except for the data recording system and sample rate, and it has a nominal precision exceeding standard water catching techniques. Precision in temperature is 4 times better, salinity 2 to 4 times better, and depth 100 times better. Accuracy is limited by in situ calibration against standard techniques. The CTD on SCIMP did not perform this well for reasons that will be discussed below. The other measurement

system is a shadowgraph unit known as the Optical Salt Finger Detector (OSFD). As its name implies, it was constructed to find salt fingers in the ocean, but it has more general applicability because it may be sensitive to other processes with microscale fluctuations in index of refraction. The shadowgraphs are coded so that they can be compared to simultaneous CTD records.

Autoprobe

The platform Autoprobe can control its buoyancy by varying its displacement. It has rubber bellows exposed to ambient pressure, which may be expanded or collapsed by pumping fluid from a rigid vessel in or out of the bellows. In this way Autoprobe changes its displacement but not its mass. Power for the pumping is supplied by compressed gas carried in two Scuba tanks.

Autoprobe is programmed electronically for a specific mission before launch. In this study, a constant sink rate is set and the instrument repeatedly adjusts its displacement to achieve the programmed rate. In addition, a maximum depth and a maximum time are also preset and if either of these are exceeded Autoprobe increases its displacement to a maximum to return to the surface. As a safety precaution, there is also a heavy weight which may be dropped in an emergency. Finally, acoustic commands from the surface can override the internal programming to change the sink rate or abort the mission.

In practice Autoprobe is normally programmed to sink at a constant rate of 5-10 cm/sec. This rate was chosen because of restraints imposed by the measurement systems. The maintenance of such a rate is important to the experiment, but the most critical characteristic of Autoprobe is

that it is not connected to the ship and measurements are not contaminated by ship motions.

Internally Recording Brown CTD

Measurements of in situ electrical conductivity, temperature and pressure are made by a Neil Brown CTD (Brown, 1974). Each quantity is digitized as a 16 bit word and recorded internally on a digital magnetic cassette tape. The resolution of the measurements, i.e., one least significant bit, is respectively 1 μmho/cm, 0.5 mC, and 0.05 decibar. The sampling rate is 2.5 Hz so that at a sink rate of 5-10 cm/sec data points are recorded every 2-4 cm. Aside from the high resolution implicit in a 16 bit digital data word, the small sensors on the Brown CTD make it well suited for measuring the fine structure of hydrographic properties in the ocean. A careful discussion of the sensors is required before any detailed analyses of the data.

Pressure Sensor

Hydrostatic pressure is measured with a strain gage bridge transducer. The overall accuracy of this transducer is claimed by the manufacturer to be $\pm$0.1% of full scale, which in this case is 3000 decibars. Although performance on cable lowered CTD's has been compatible with manufacturer specifications (Fofonoff, Hayes and Millard, 1974), the pressure transducer on SCIMP has displayed two modes of erratic behavior. These failures have made absolute pressure unreliable on many dives, while on some segments of dives, the pressure is essentially worthless.

The first mode of erratic behavior is an offset slip. In this mode the pressure increases abruptly by a large amount ($\approx$5% of the current pressure reading) while the instrument is descending and then appears

to behave normally afterward, including returning to surface pressure at the surface. This phenomenon is sometimes observed when the instrument fires a squib that drops a weight to change the instrument's sink rate. However, it also occurs at other times for no apparent reason.

The cause for this offset slip is unknown, but may be attributable to a faulty pressure transducer since it has not been observed on cable-lowered instruments at WHOI. Since the pressure must be known accurately to calculate salinity accurately, this makes many of the absolute determinations of salinity doubtful. However, in most calculations in this study, relative salinity changes within a particular dive are sufficient and the malfunction is not as serious as it may seem. The principal limitation is that extreme caution must be exercised before making conclusions based on changes in hydrographic properties between two dives or between SCIMP and other CTDs.

The second mode of failure in the pressure signal is believed to be an electronic problem. In this mode the pressure becomes extremely noisy, varying in a random-like manner between the actual pressure (extrapolated from regions where ther pressure is not noisy) and a level about 20% less than the actual pressure. This behavior is intermittant so that there may be several of these segments, each 100-200 meters in duration, in a dive to 1500 m depth. It is believed that this is due to water condensation on the pressure interface board which causes an intermittant electrical leak. The problem has been corrected by careful drying of the circuit board and using additional drying agent within the instrument case.

In an attempt to recover some of the information in these data, the sink rate of the instrument is assumed to be constant or piece-wise constant and pressure is interpolated between sections where the pressure signal is well behaved. This procedure is moderately successful in that the relative salinity field can be fairly well reproduced, but often calculated density distribution becomes unrealistic. However, the data are still useful for many applications, particularly for small vertical length scales.

Temperature Sensor

The temperature sensor is a platinum resistance thermometer with a nominal time constant of 310 msec at a sink rate of 92 cm/sec. Since the sink rate for SCIMP is a factor of 10 slower than this, the time constant in this application may be somewhat different.

The geometry of the platinum thermometer is complicated by a perforated stainless steel protective shield and mounting, but a crude estimate can be made of the dependence of time constant on sink rate. First assume that the time constant is inversely proportional to a heat transfer coefficient h, and that self-heating is not of primary importance. Empirical data show that a reasonable estimate for the dependence of heat transfer coefficient on Reynolds number, R_e, for a long cylinder immersed in water with flow normal to its generators is

$$h_t \propto (R_e)^{1/2}$$

where $R_e = \frac{ud}{\nu}$, defined in terms of the free stream velocity, u, the cylinder diameter, d, and the kinematic viscosity, ν. Then if the

velocity and hence the Reynolds number is decreased by a factor of 10, the heat transfer coefficient decreases by a factor of $10^{1/2}$ and the time constant increases by the same factor. This suggests that the time constant for the platinum thermometer sinking at 10 cm/sec is approximately 1 sec. This means that temperature changes that occur over distances less than 10 cm cannot be fully resolved.

The absolute accuracy of the temperature measurement is estimated at ± 1.5 m°C based on linearity of the electronics and calibrations made before and after use at sea.

Conductivity Sensor

The conductivity sensor is a miniature four-electrode cell. The sensing element is a cylinder 8 mm long and the hole in the center is 2 mm in diameter. The walls of the sensor are approximately 1 mm thick and they are constructed of alumina.

The nominal time constant of the cell is equal to its flushing rate, the ratio of its length to the instrument's speed through the water. This ratio is approximately 1/15 s for the measurements in the text, but in practice the response time was found to be several seconds. The reason for this slow response is unknown, but it may be a case of fouling.

Optical Salt Finger Detector

The OSFD is a shadowgraph imaging and recording system that can operate in the deep ocean. It is the most novel aspect of the instrumentation and as such it presents unique problems of data processing. A parallel beam of light will produce an image of uniform intensity when it passes through a medium that has an index of refraction distribution that has the second spatial derivative equal to zero everywhere. But if there are finite values of second derivative, there will be varia-

tions in intensity of the image because the medium will focus or defocus the light at a particular point. The variations in light intensity within the image are then an integral measure of the fluctuations in index of refraction within the beam path.

The light source for the OSFD is a 3.0 mW continuous pulse helium-neon laser. This beam is expanded to a diameter of 5 cm before it passes through a glass window in the pressure case into the water. The beam then passes through 0.8 m of undisturbed sea water, is reflected back toward the pressure case by two mirrors which are at right angles to each other, and returns through another 0.8 m of sea water to the pressure case, and it then is focused and expanded again to increase its effective focal length. The image is then projected on a ground glass screen where it is encoded with a number which is common to the simultaneous CTD record and photographed with a 16 mm movie camera. The camera photographs at a rate of approximately 1 Hz and can record approximately 16,000 images on 400 ft. of film.

There are several important characteristics of the OSFD system that may be subtle. The first is size preservation; because the beam is parallel as it passes through the sea water, all images maintain their position relative to the beam regardless of where in the seawater path they occur. The inhomogeneities in index of refraction are weak in the deep ocean, so the sensitivity of the system is increased by optical compression. These weak gradients are equivalent to long focal lengths, longer than can be accommodated in a 1.5 m long tube. In practice the strongest images found in the deep ocean have focal lengths in the range of 10-100 m. Also the variation of index of refraction with

density, temperature, salinity and pressure must be understood when evaluating an image. It is possible that a distribution may have sharp temperature gradients and still be invisible, and, in particular, linear gradients in index of refraction have no image on a shadowgraph.

Interpretation of Shadowgraphs

Because shadowgraphs of the deep ocean have never been made before, the interpretation of these measurements presents a novel problem. In order for an image to be visible on a shadowgraph there must be fluctuations in index of refraction. The shadowgraph technique is sensitive to the second spatial derivative of index of refraction in that the variations in intensity of the image depends on convergence and divergence of parallel light rays. The result is a maximum in brightness (convergence of rays) at a maximum of second derivative of refractive index and a corresponding minimum in brightness (divergence of rays) where the second derivative is also a minimum. An important corollary is that linear gradients in refractive index leave no image on a shadowgraph.

Refractive index is closely related to density in sea water, though not perfectly so. The relationship between refractive index and the normal oceanographic variables - temperature, salinity, and pressure - have not been extensively measured. The only complete set of measurements as a function of temperature and salinity over the ranges found in the ocean were made by Utterback, Thompson and Thomas in 1934. Since then Stanley (1971) has additionally measured the relationship between refractive index and pressure for different wavelengths of light.

Since refractive index is closely related to density in seawater and density differences in the deep ocean are very small, an extremely sensitive shadowgraph system is necessary to detect a signal in the deep ocean. In general the uncertainty in the relationship of temperature and salinity to refractive index is so great that it would be difficult to say that a structure is positively visible or invisible even with perfect information on the temperature and salinity. It is expected then that some structures will be invisible even though there are strong gradients of temperature or salinity because the proportions are such that there are no measurable fluctuations in index of refraction. The CTD does not measure salinity on a scale small enough to predict when structures become invisible. On the basis of temperature and salinity then there are two requirements for visibility:

(1) distributions of temperature and salinity with large spatial second derivitives

(2) proportions of temperature difference and salinity difference that lead to finite differences in refractive index.

The diameter of the parallel light beam as it passes through the sea water is 5 cm. This places bounds on the length scale of structures that can be seen on the shadowgraphs. The largest scale that can be recognized on the shadowgraph is approximately 2 cm since both light and dark must appear on the photograph for contrast. Similarly, the smallest scale that can be recognized depends on the quality of the image and the intensity of the contrast. A few millimeters seems to be the limit for recognizable contrasts in the OSFD system. Thus, there is information on the shadowgraph with length scales that span a decade with a maximum length of 2 cm.

The OSFD was originally designed to photograph salt fingers in the ocean (Williams, 1975). They are visible because rising and sinking fingers have different indices of refraction and because a group of salt fingers forms an orderly array. The shadow effect is amplified by an orderly array of salt fingers over contrast from a single pair of fingers because there are paths for the light through the array where it travels mainly through either rising or sinking fingers. For a square array that is seen in the laboratory, this effect is a maximum when the light passes diagonally through the square salt finger. And in this case the diameter that is measured on the shadowgraph is actually the diagonal rather than the length of a side, L, as derived in Section 2.1. Naturally, the ratio of these two dimensions is $\sqrt{2}$.

APPENDIX B

VERIFICATION OF BANDED STRUCTURE

In most cases the images in the shadowgraphs due to ocean microstructure are weak and difficult to quantify. Frames with structure either characteristic of salt fingers or of a more random nature are identified subjectively while viewing the films. Although human sight is a very effective means of translating optical data to more conventional forms, a more direct approach that is less dependent on human judgement may be desirable. But because human sight is such a sophisticated interpretor of optical information, high levels of technology are necessary to equal or exceed its performance. For purposes of illustration, some measurements with a simple densitometer have been made on the shadowgraph films.

The apparatus consists of a light source, lens to focus the light at a point on the film, a photoresistor to receive the light shown through the film, and a motor with coupling to move the film past the light at a regulated rate. The voltage drop across the photoresistor when placed in a simple electronic circuit varies with the density of the image on the film, and this voltage is entered into a Fourier analyzer for spectral analysis.

The measurement procedure was directed toward educing a peak in the horizontal wave number spectrum characteristic of salt fingers. The film is scanned with the light beam in a direction that corresponds to horizontal in the ocean and the intensity or voltage distribution is digitized and recorded. The autospectrum is then calculated

and ensemble averaged with other realizations at different levels in a particular frame. Typically, five spectra are averaged to form a single estimate with 10 degrees of freedom. The technique was used on several events where salt fingers were identified visually, but it was only successful on the one event with the highest contrast on the films.

Figure B1 shows the temperature profile through the best example of banded structure on the films. The individual frames that were photographed at the interface are reproduced in Figure B2. The location of the photographs relative to the profile are indicated by the two-digit number code. In general, the vertically banded structure corresponds well with the high gradient region.

The estimates of the spectra of photointensity are shown in Figures B3 and B4 and these are also coded to allow comparison with the profile and the photographs. Each estimate is the average of 5 scans through the photograph, and the intensity or energy density is in arbitrary units related to the voltage drop across the photoresistor. However, the scale used in 24-33 is a factor of 5 different than that of 35-44, illustrating the higher contrast in the earlier frames. The first five spectra have well developed peaks of nearly constant amplitude, but the dominant wave number varies between 0.9 and 1.6 cycles/cm. This scatter should be compared to the resolution of the system which was 0.25 cycles/cm. Since there were only a few cycles in any realization this amount of scatter should not be surprising. To relate this spectrum to a finger diameter, the geometric factor of $\sqrt{2}$ for the most visible salt fingers from Appendix A is introduced,

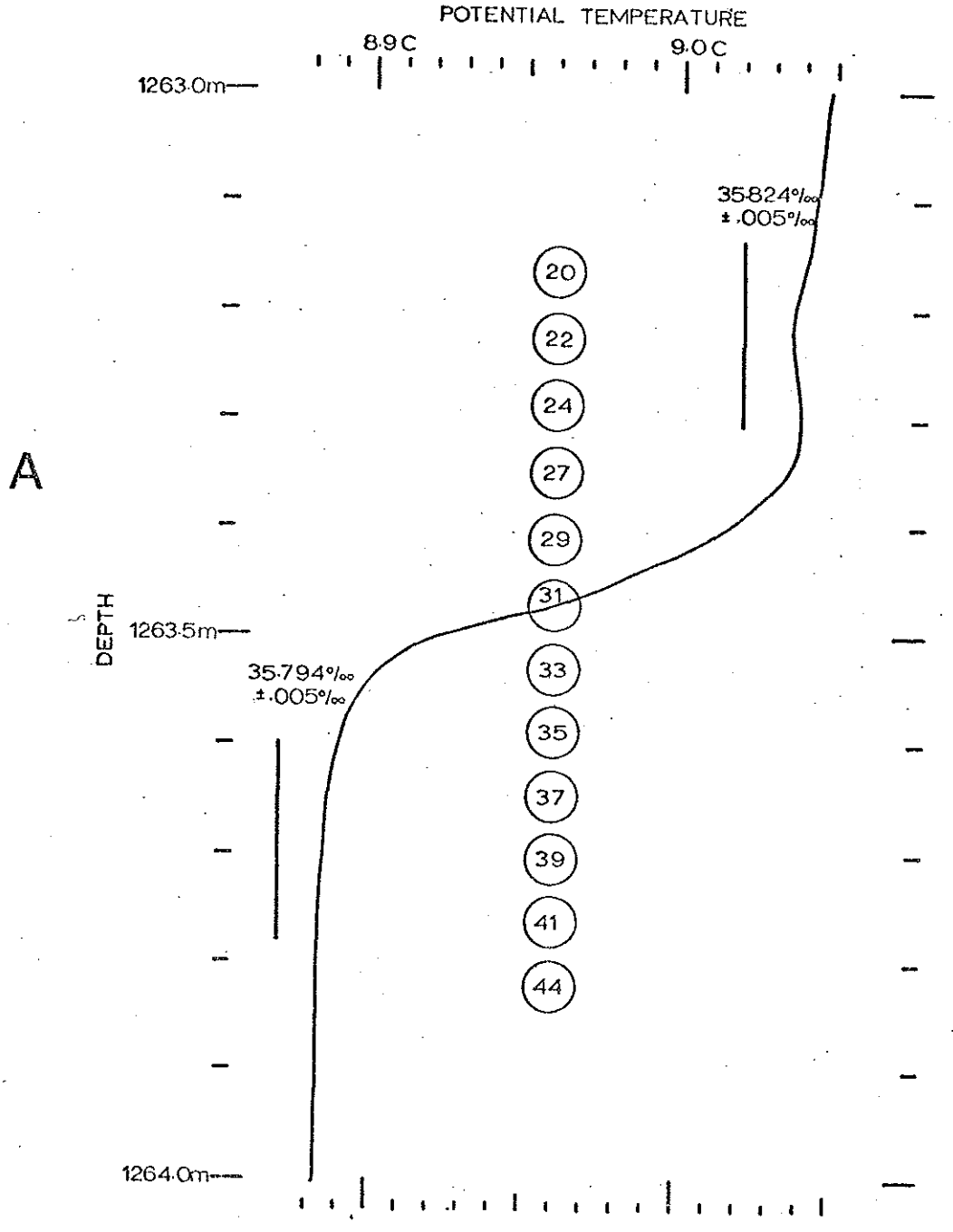

FIGURE B-1 Potential temperature profile of interface from SCIMP 1. This interface is also plotted in Figure 3.25. The circled numbers indicate the positions of shadowgraphs relative to the profile. This graph is an excerpt from Williams, 1974.

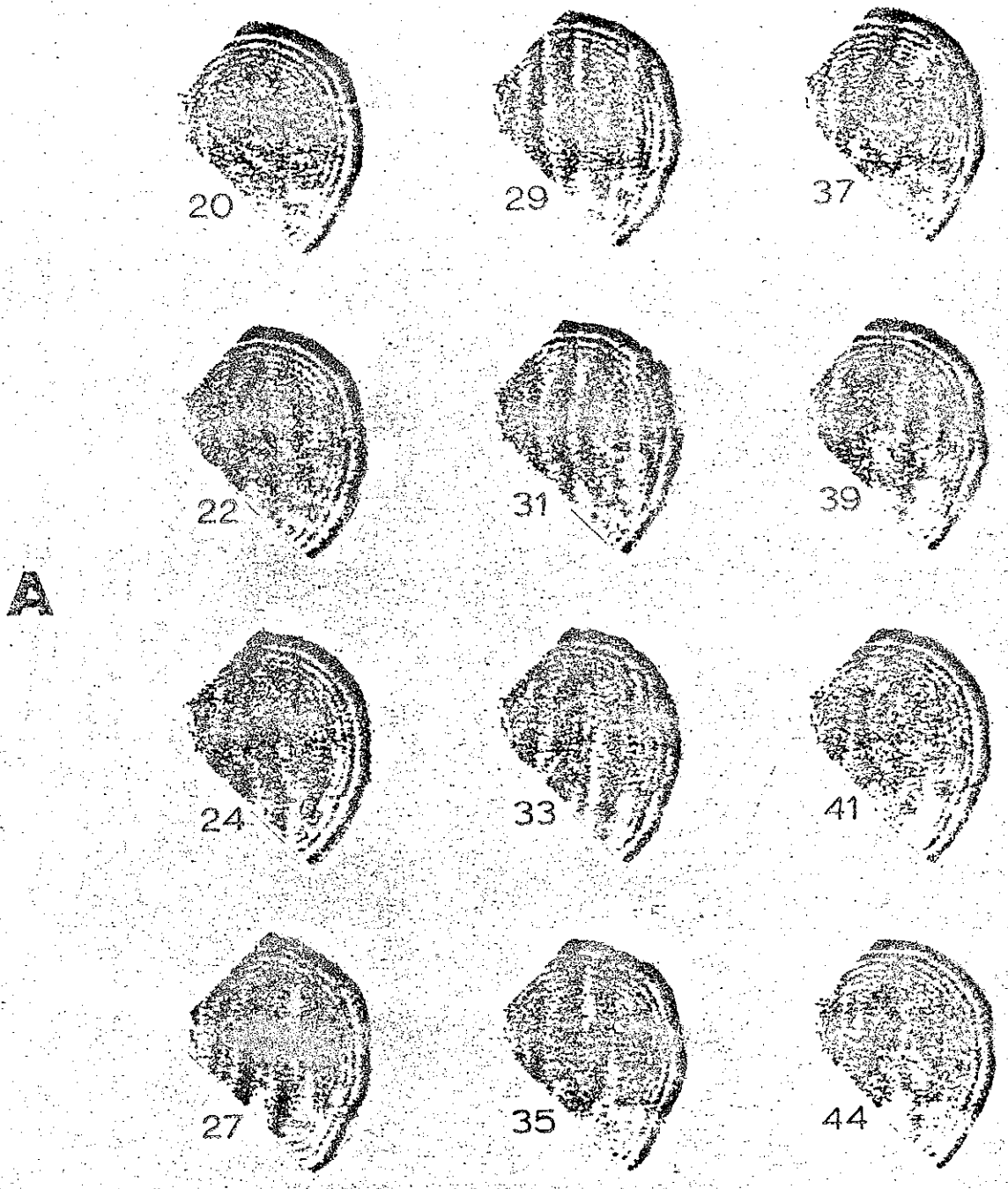

FIGURE B-2 Shadowgraphs for the profile in Figure B-1. Vertical bands are most pronounced near the center of the interface. The diameter of the shadowgraphs is 5 cm (Williams, 1974).

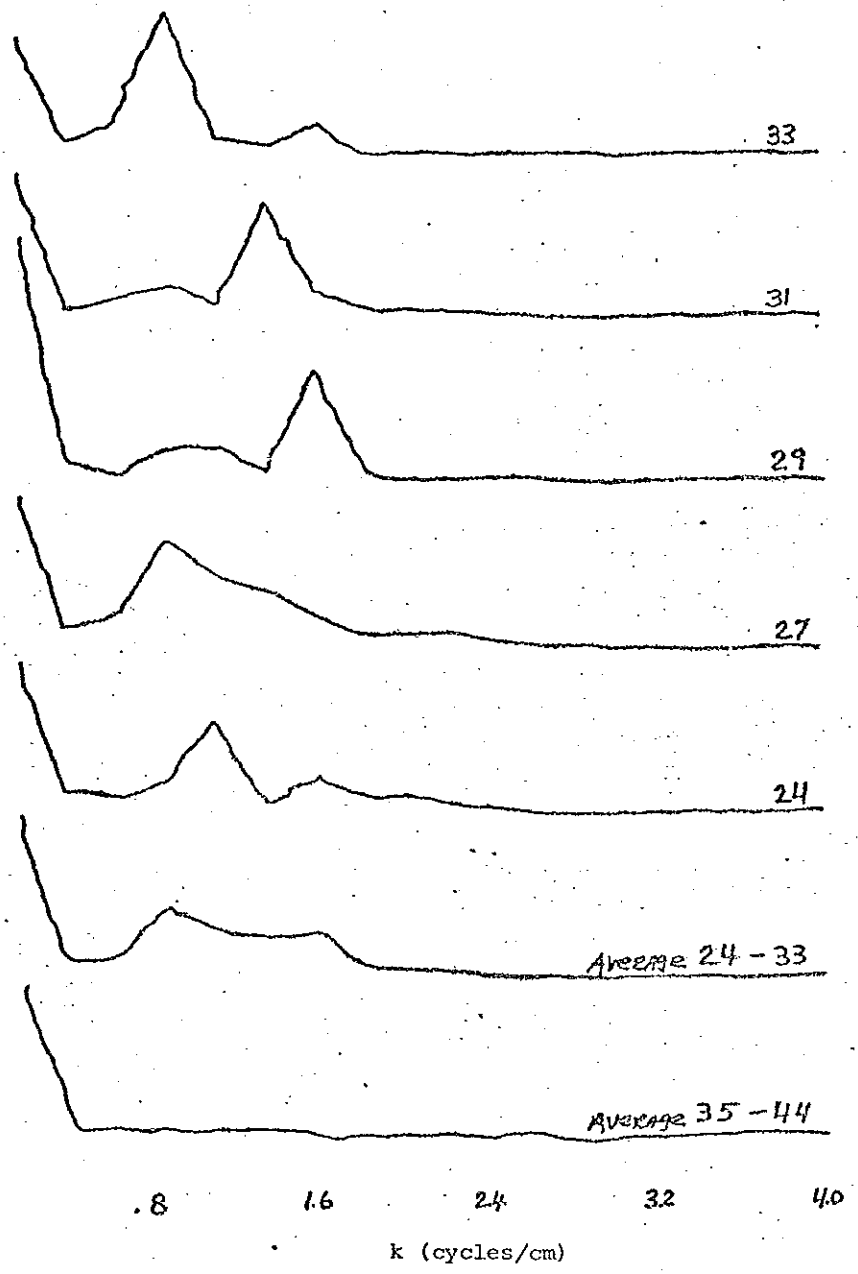

FIGURE B-3 Spectra of photointensity for a horizontal scan across the photographs in Figure B-2. A number identifies each spectrum with a photograph. There is a strong peak in the spectrum near 1 cycle/cm for each of the photographs. Each estimate has 10 degrees of freedom. The average of the 5 spectra is also shown as well as the average of the 5 spectra from the photographs of the lower part of the interface. The units of the ordinate are arbitrary but uniform.

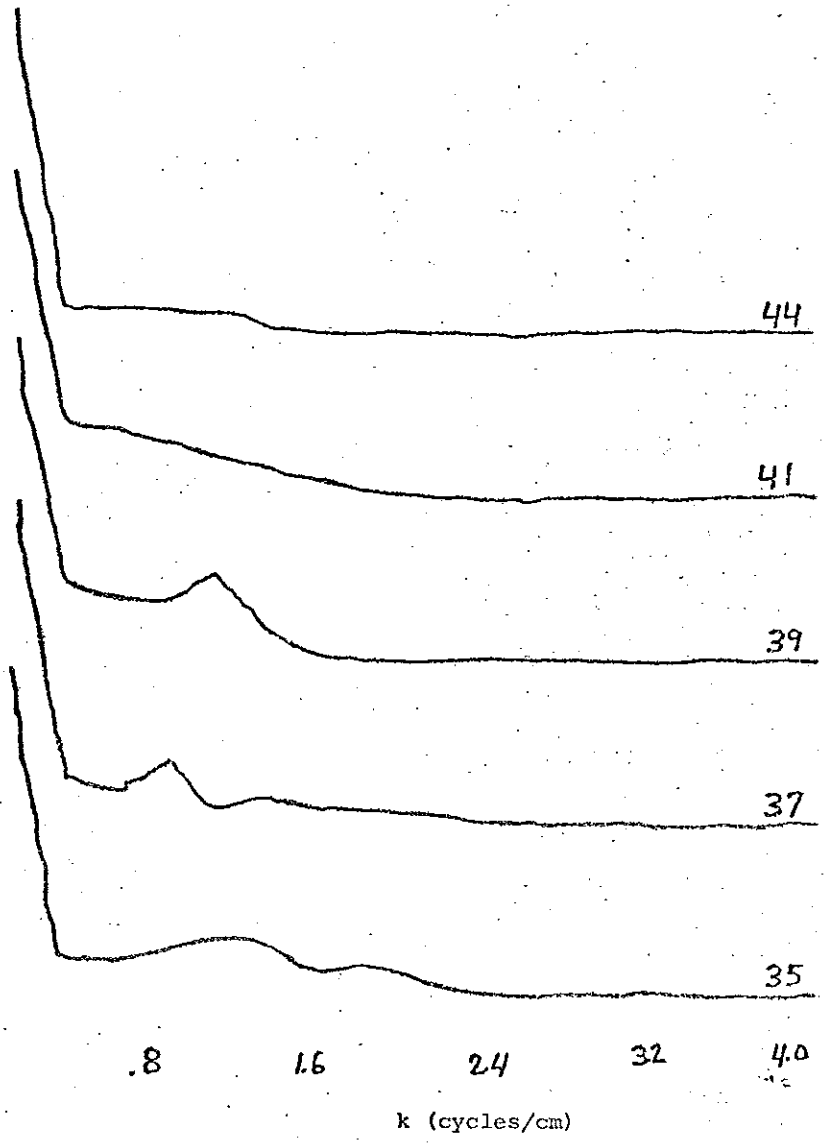

FIGURE B-4 Spectra of photointensity for 5 photographs from the lower part of the interface in Figure B-1. The ordinate is magnified by a factor of 5 over the spectra in Figure B-3. There are also 10 degrees of freedom here and the average of these 5 is shown in B-3.

then based on the extreme values for the spectral peaks,

$$L = \frac{1}{2k\sqrt{2}} = 0.22 - 0.39 \text{ cm}$$

Because of the L^4 relation for finger diameter as a function of other properties, this uncertainty in finger diameter is equivalent to a factor of 10 uncertainty in other properties, e.g. temperature gradient or flux ratio.

APPENDIX C

DENSITY FUNCTIONS

In the deep ocean density differences are generally small and a proper representation of the equation of state is essential. There are also several functions that are used to represent density and the correct one must be used to avoid erroneous results. This appendix describes the density functions commonly used and suggests some limits for their applicability.

Either the density, ρ, or its reciprocal the specific volume, α, may be used in the equation of state,

$$\rho = \rho(T, S, p) \quad \text{or} \quad \alpha = \alpha(T, S, p) \tag{C1}$$

where T is the temperature, S is the salinity and p is the pressure. The derived quantity, σ, is often used in oceanography to represent density, and it is defined

$$\sigma(T, S, p) = 1000\left[\rho(T, S, p) - 1\right] \tag{C2}$$

in cgs units. In order to compare water at different levels, the direct influence of pressure is removed in defining sigma-t

$$\sigma_T(T, S) = \sigma(T, S, 0) \tag{C3}$$

where the oceanographic pressure, p = 0, is one atmosphere absolute

pressure. A further refinement where the effect of pressure on the temperature is taken into account is potential density

$$\sigma_\theta = \sigma_t(\theta, S) \qquad \text{(C4)}$$

where θ is the potential temperature or the temperature a parcel of water would have when transported adiabatically to the surface. Potential density, σ_θ, is the preferred representation for the computation of currents because the effect of pressure appears to be completely removed. However, there are instances where the use of potential density can be misleading because the surface may not be the best place to compare two parcels of water, both of which come from depth. There is an example of the problems that may arise in the abyssal water of the North Atlantic where σ_θ decreases with depth while the water column is statically stable according to the Hesselberg-Sverdrup criterion. This inconsistency arises because the compressibility of sea water increases with decreasing temperature.

The Hesselberg-Sverdrup expression for stability is given by

$$N^2 = -g/\rho \left[\frac{d\rho}{dz} - \frac{\partial \rho}{\partial z} \right)_{\eta, S} \Bigg] > 0 \qquad \text{(C5)}$$

where Z is the vertical coordinate, positive upward, and η is the entropy. This is a purely local property and cannot correctly be written in terms of σ_θ, which involves adiabatic expansion to the surface. The first term in the braces is the prevailing density gradient and the second term is the adiabatic gradient for that

particular temperature, salinity and pressure, a property of the fluid. The potential density gradient, normalized by $-g/\rho$ can be written as

$$N_\theta^2 = -g/\rho \frac{d\sigma_\theta}{dz} \times 10^{-3} \qquad \text{(C6)}$$

Although this is similar in form to N^2, they are only equal when N^2 is evaluated at the surface, p = 0. Another representation of σ_θ which brings this point out explicitly is

$$\sigma_\theta = \sigma(T, S, p) + 1000\left[\int_p^0 K\,dP - 1\right] \qquad \text{(C7)}$$

where the compressibility K is defined

$$K \equiv \frac{\partial \rho}{\partial p}\Big)_{\eta, S} = 1/c^2 \qquad \text{(C8)}$$

where c is the speed of sound. The dependence of compressibility on temperature is the essential factor here; taking the partial derivative,

$$\frac{\partial K}{\partial T} = -2c^{-3}\frac{\partial c}{\partial T} \qquad \text{(C9)}$$

From speed of sound tables by Leroy (1968), this term may be evaluated for S = 35°/oo.

TABLE C1

P (decibars) \ T(celius)	0-1	1-2	2-3	3-4
1000	2.81	2.75	2.67	2.63
2000	2.74	2.65	2.58	2.50
3000	2.62	2.55	2.48	2.40
4000	2.49	2.44	2.37	2.30
6000	2.27	2.21	2.15	2.09

For an example of this effect, consider two parcels of water, each with a salinity of 35°/oo and each at a pressure of 6000 decibars. Parcel A has a temperature of zero degrees and Parcel B has a temperature of δT . This implies that Parcel A is denser than B by an amount

$$\delta \rho_{AB} = \rho_A - \rho_B = 1.8 \times 10^{-4} \delta T \qquad \text{(C10)}$$

Raising these two to the surface adiabatically and evaluating the density difference there gives

$$\delta \rho_{AB}\Big|_{p=0} = \delta \rho_{AB}\Big|_{p=6000} + \int_{6000}^{0} \frac{\partial K}{\partial T} \delta T \, dp \qquad \text{(C11)}$$

From the above table, choosing a representative value $\frac{\partial K}{\partial T} = -2.7 \times 10^{-4} \frac{(S/cm)^2}{°C}$, a constant, to simplify the integral, then

$$\delta \rho_{AB}\Big|_{p=0} = 1.8 \times 10^{-4} \delta T - 1.6 \times 10^{-4} \delta T \qquad \text{(C12)}$$

or the density difference has been reduced to approximately 0.1 of its in situ value. This illustrates that the density of water at different temperatures should not be compared at pressures greatly different than the in situ pressure.

Although the compressibility is not a strong function of salinity, salinity plays an important role in this discussion. Two parcels of water may have the same density at the same pressure with compensating differences in temperature and salinity. Increasing the salinity and

decreasing the temperature both increase the density of sea water, so that a parcel that is both warmer and more saline than another may have the same density.

Using the same numerical value for the compressibility derivative as before, if two parcels are initially the same density, for every 1000 decibar expansion the colder parcel becomes approximately 27 x 10^{-6} gr/cm^3 lighter for each 1.0C initial temperature difference.

This effect where the compressibility is strongly dependent on temperature can be neglected in many oceanographic applications, but in certain cases such as abyssal circulation and situations with large compensating salinity and temperature differences, it becomes critical. For abyssal circulation, Lynn and Reid (1968) have adopted a deep reference for density rather than the surface. They have specifically chosen 4000 decibars as a reference and found it to be more suitable for dynamic calculations. In the present context, the use of sigma-theta as a measure of density leads an incorrect representation of the stability of interfaces in the case of interleaving of different water types. When a layer of colder fresher water overlies a layer of warmer saltier water, the density contrast between the two layers is overstated by sigma-theta while in the opposite it is understated and can even lead to an apparent density inversion. Consider the case of a warm salty layer intruding in a region where the temperature is nearly constant, such as may be found near the core of the Mediterranean Water in the Western North Atlantic. If for example, the pressure is 1000 db and the temperature contrast is 0.2C, then the use of sigma-theta overstates the density difference on the upper interface by about 4.4 ppm,

and understates the difference at the bottom of the layer by the same amount. Similarly in the salt fingering staircase below, the salinity maximum at a pressure of approximately 1500 db, the temperature difference across an interface is typically 0.1C and sigma-theta understates the density difference by approximately 3.6 ppm. This is about the same as the density contrast in terms of local density so that these layers may appear unstable in terms of sigma-theta.

REFERENCES

Baines, P.G. and A.E. Gill (1969). On thermohaline convection with linear gradients. J. Fluid Mech., vol. 37, 289-306.

Batchelor, G.K. (1959). Small-scale variations of convected quantities like temperature in a turbulent fluid, part 1. J. Fluid Mech., vol. 5, 113.

Brown, N. (1974). A precision CTD microprofiler. Proceedings IEEE International Conference on Engineering in the Ocean Environment, vol. II, 270-278.

Burt, K.H. (1974). Autoprobe: an autonomous observational platform for microstructure studies. Proceedings IEEE International Conference on Engineering in the Ocean Environment, vol. I, 171-176.

Businger, J.A., J.C. Wyngaard, Y. Izumi, and E.F. Bradley (1971). Flux-profile relationships in the atmospheric surface layer. J. Atmos. Sci., vol. 28, 181-189.

Chandrasekhar, S. (1961). Hydrodynamic and hydromagnetic stability. Clarendon Press, Oxford, England.

Fofonoff, N.P., S.P. Hayes and R.C. Millard, Jr. (1974). W.H.O.I./Brown CTD microprofiler: methods of calibration and data handling. Woods Hole Oceanographic Institution Technical Report 74-89.

Foster, T.D. (1971). Intermittant convection. Geophys. Fluid Dyn., vol. 2, 201-217.

Garrett, C. and W. Munk (1972). Space-time scales of internal waves. Geophys. Fluid Dyn., vol. 2, 225-264.

Garrett, C. and W. Munk (1975). Space-time scales of internal waves: a progress report. J. Geophys. Res., vol. 80, no. 3, 291-297.

Gibson, C.H. and W.H. Schwartz (1963). The universal equilibrium spectra of turbulent velocity and scalar fields. J. Fluid Mech., vol. 16, 365-373.

Grant, H.L., R.W. Stewart, and A. Moilliet (1962). Turbulent spectra from a tidal channel. J. Fluid Mech., vol. 12, 241-268.

Gregg, M.C. (1975). Microstructure and intrusions in the California Current. J. Phys. Oceanogr., vol. 5, 253-278.

Gregg, M.C., C.S. Cox, and P.W. Hacker (1973). Vertical microstructure measurements in the central North Pacific. J. Phys. Oceanogr., vol. 3, 458-469.

Hayes, S.P., T.M. Joyce and R.C. Millard, Jr. (1975). Measurements of vertical fine structure in the Sargasso Sea. J. Geophys. Res., vol. 80, no. 3, 314-319.

Howard, L.N. (1964). Convection at high Rayleigh number. Proc. eleventh Int. Congress Applied Mechanics, Munich (ed. H. Gortler), pp. 1109-1115, Springer-Verlag, Berlin, W. Germany.

Howe, M.R. and R.I. Tait (1970). Further observations of thermo-haline stratification in the deep ocean. Deep-Sea Res., vol. 17, 963-972.

Huppert, H.E. and P.C. Manins (1973). Limiting conditions for salt-fingering at an interface. Deep-Sea Res., vol. 20, 315-324.

Johannessen, O.M. and O.S. Lee (1974). A deep stepped thermo-haline structure in the Mediterranean. Deep-Sea Res., vol. 21, 629-639.

Katz, E. (1973). Profile of an isopycnal surface in the main thermocline of the Sargasso Sea. J. Phys. Oceanogr., vol. 3, 448-457.

Lambert, R.B. and J.W. Demenkow (1972). On the vertical transport due to fingers in double diffusive convection. J. Fluid Mech., vol. 54, 627-640.

Landau, L.D. and E.M. Lifshitz (1959). Fluid Mechanics, Pergamon Press, Reading, Massachusetts.

Leroy, C.C. (1968). A simple and accurate formula for the calculation of the velocity of sound in sea water. Saclant ASW Research Centre Technical Report 111.

Linden, P.F. (1971). The effect of turbulence and shear on salt fingers. Ph.D. thesis. University of Cambridge.

Linden, P.F. (1973). On the structure of salt fingers. Deep-Sea Res., vol. 20, 325-340.

Long, R.R. (1970). A theory of turbulence in stratified fluids. J. Fluid Mech., vol. 42, 349-365.

Lumley, J.L. (1964). The spectrum of nearly inertial turbulence in a stably stratified fluid. J. Atmos. Sci., vol. 21, 99-102.

Lynn, R.J., and J.L. Reid (1968). Characteristics and circulation of deep and abyssal waters. Deep-Sea Res., vol. 15, 577-598.

Malkus, W.V.R. (1954). Discrete transitions in turbulent convection. Proc. Roy. Soc. A, vol. 225, 196-212.

Molcard, R. and A.J. Williams 3rd (1975). Deep stepped structure in the Tyrrhenian Sea. Memoires Societe Royale des Sciences de Liege, 6^{e} serie, tome VIII, 191-210.

Needler, G.T., and R.A. Heath (1975). Diffusion coefficients calculated from the Mediterranean salinity anomaly in the North Atlantic Ocean. J. Phys. Oceanogr., vol. 5, 173-182.

Phillips, O.M. (1966). The Dynamics of the Upper Ocean. Cambridge University Press, Cambridge, England.

Phillips, O.M. (1971). On spectra measured in an undulating layered medium. J. Phys. Oceanogr., vol. 1, 1-6.

Pingree, R.D. (1971). Regularly spaced instrumental temperature and salinity structures. Deep-Sea Res., vol. 18, 841-844.

Rossby, H.T. (1969). A study of Benard convection with and without rotation. J. Fluid Mech., vol. 36, 309-335.

Rusby, J.S.M. (1967). Measurements of the refractive index of sea water relative to Copenhagen Standard Sea Water. Deep-Sea Res., vol. 14, 427-439.

Shirtcliffe, T.G.L. (1967). Thermosolutal convection: observation of an overstable mode. Nature, vol. 213, 489-490.

Shirtcliffe, T.G.L., and J.S. Turner (1970). Observations of the cell structure of salt fingers. J. Fluid Mech., vol. 41, 707-719.

Siedler, G. and W. Zenk (1973). Variability of the thermohaline staircase. Nature Phys. Sci., vol. 244, 11-12.

Somerscules, E.F.C. and I.W. Gazda (1969). Thermal convection in high Prandtl number liquids at high Rayleigh numbers. Int. J. Heat, Mass Transfer, vol. 12, 1491-1511.

Sparrow, E.M., R.B. Husar and R.J. Goldstein (1970). Observations and other characteristics of thermals. J. Fluid Mech. vol. 41, 793-800.

Stanley, E.M. (1971). The refractive index of seawater as a function of temperature, pressure, and two wave lengths. Deep-Sea Res., vol. 18, 833-840.

Stern, M.E. (1960). The "salt fountain" and thermohaline convection. Tellus, vol. 12, 172-175.

Stern, M.E. (1969). Collective instability of salt fingers. J. Fluid Mech., vol. 35, 209-218.

Stern, M. (1976). Maximum buoyancy flux across a salt finger interface. J. Mar. Res., vol. 34, 95-110.

Stern, M.E. and J. S. Turner (1969). Salt fingers and convecting layers. Deep-Sea Res., vol. 16, 497-511.

Stommel, H. , A.B. Arons, and D. Blanchard (1956). An oceanographical curiosity: the perpetual salt fountain. Deep-Sea Res., vol. 3, 152-153.

Sverdrup, H.U., M.W. Johnson, and R. H. Fleming (1942). The Oceans, Their Physics, Chemistry and General Biology. Prentice-Hall, Englewood Cliffs, New Jersey.

Tait, R.I. and M.R. Howe (1968). Some ovservations of thermohaline stratification in the deep ocean. Deep-Sea. Res., vol. 15, 275-280.

Tait, R.I. and M.R. Howe (1971). Thermohaline staircase. Nature, vol. 231, 178-179.

Turner, J.S. (1967). Salt fingers across a density interface. Deep-Sea Res., vol. 14, 599-611.

Turner, J.S. (1972). On the energy deficiency of self-preserving convective flows. J. Fluid Mech., vol. 53, 217-226.

Turner, J.S. (1973). Buoyancy effects in fluids. Cambridge University Press, Cambridge, England.

Turner, J.S. and C.F. Chen (1974). Two-dimensional effects in double-diffusive convection. J. Fluid Mech., vol. 34, 577-592.

Utterback, C.L., T.G. Thompson and B.D. Thomas (1934). Refractivity-chlorinity-temperature relationships of ocean waters. J. du Conseil. Conseil permanent international pour l'exploration de la mer, vol. 9, 35-38.

Veronis, G. (1965). On finite amplitude instability in thermohaline convection. J. Mar. Res., vol. 23, 1-17.

Williams, A.J. 3rd (1975). Images of ocean microstructure. Deep-Sea Res., vol. 22, 811-829.

Woods, J.D. and R.L. Wiley (1972). Billow turbulence and ocean microstructure. Deep-Sea Res., vol. 19, 87-121.

Wüst, G. (1961). On the vertical circulation of the Mediterranean Sea.

BIOGRAPHICAL NOTE

Peter John Hendricks was born on November 15, 1944 in Jersey City, New Jersey. He grew up in Bayville, New York where he attended Locust Valley High School. At Brown University he was elected to Tau Beta Pi and Sigma Xi, graduating with an A.B. and Sc.B. cum laude with High Honors in Aerospace Engineering in 1967. He attended graduate school in the Department of Applied Mechanics and Engineering Science at the University of California, San Diego, where he earned an M.S. in Aerospace Engineering in 1969. During the period 1968-1971 he was employed as a Member of the Technical Staff at the TRW System Group, Redondo Beach, California. He entered the Woods Hole Oceanographic Institution and Massachusetts Institute of Technology Joint Program in Ocean Engineering in September, 1971. He has been married to the former Miss Kathleen Durick since August 1974.